

A SEARCH FOR LIGHTLY IONIZING PARTICLES
IN THE LUX DETECTOR AND R&D FOR FUTURE
EXPERIMENTS

by

KATAYUN J KAMDIN

A dissertation submitted in partial satisfaction of the
requirements for the degree of

Doctor of Philosophy

in

Physics

in the

Graduate Division

of the

University of California, Berkeley

Committee in charge:

Professor Daniel McKinsey, Chair

Professor Marjorie Shapiro

Doctor Peter Sorensen

Professor Kai Vetter

Summer 2018

ABSTRACT

A Search for Lightly Ionizing Particles in the LUX Detector and R&D
For Future Experiments

by

Katayun J Kamdin

Doctor of Philosophy
University of California, Berkeley
Professor Daniel McKinsey, Chair

Write the abstract here.

To my mom, for always making me feel like I could do this. To my friends, for being there when I was sure I couldn't.

ACKNOWLEDGMENTS

Some Text

More Text.

More text

CONTENTS

1	INTRODUCTION	1
I	THEORETICAL CONTEXT AND EXPERIMENTAL STRATEGIES	2
2	THEORETICAL BACKGROUND	3
2.1	A Little History	3
2.2	Evidence for Dark Matter	5
2.2.1	Galaxies and Clusters	6
2.2.2	Cosmic Microwave Background	8
2.3	Standard Models	12
2.3.1	The Standard Cosmology	12
2.3.2	The Standard Model of Particle Physics	14
2.4	Dark Matter Candidates Motivated by Particle Physics	17
2.4.1	WIMPs and the Hierarchy Problem	17
2.4.2	Axions and the Strong CP Problem	20
2.5	The Dark Sector and Lightly Ionizing Particles	20
2.5.1	Dark Sector	20
2.5.2	Lightly Ionizing Particles	22
2.5.3	WIMPless Miracle and the New Physics Flavor Problem	25
2.5.4	Charge Quantization	27
2.6	Experimental Strategies for Detecting Dark Matter	27
2.6.1	Production	27
2.6.2	Indirect Detection	28
2.6.3	Direct Detection	29
3	PARTICLE DETECTION WITH LIQUID XENON	31
3.1	Liquid Xenon as a Detector Medium	31
3.1.1	Properties of Liquid Xenon	31
3.1.2	Scintillation and Ionization Signal Generation	33
3.2	Dual-Phase Xenon Time Projection Chamber	34
3.2.1	Energy Reconstruction	36
3.3	Dual-Phase Xenon TPCs for Dark Matter Detection	39
3.3.1	WIMP Searches with LXe TPCs	39
3.3.2	Other Dark Matter Searches with LXe TPCs	44
II	BIG SCIENCE	48
4	THE LUX DETECTOR	49
4.1	LUX Overview	49
4.2	Internal Components	49
4.3	External Components	51

4.4	Trigger and Data Acquisition	54
4.5	Data Processing	56
4.6	Calibrations	57
4.6.1	Energy Reconstruction	58
4.6.2	Metastable Krypton-83 (^{83m}Kr): A Multifunction Calibration	59
4.6.3	Tritium Beta Decay: Calibration of the ER Band and Yields	64
4.6.4	Deuterium-Deuterium (DD) Neutrons: Calibration of the NR Band and Yields	66
4.6.5	Power of LUX Calibrations	67
5	LIGHTLY IONIZING PARTICLE SEARCH	70
5.1	Modeling LIP Interaction	70
5.1.1	Collision Cross Section	70
5.1.2	Photo Absorption Ionization Model for Charge Particle Energy Loss	71
5.1.3	Straggling	72
5.1.4	Energy Resolution in LUX	72
5.1.5	Position Resolution in LUX	72
5.2	LIP Search	72
5.2.1	LUX Run03 Conditions	72
5.3	LIP Search Analysis	72
5.3.1	Energy Consistency	72
5.3.2	Track Linearity Criteria	72
5.3.3	Background Rejection	72
5.3.4	Muons	72
5.3.5	Gammas	72
5.3.6	Electron Trains?	72
5.4	Result: Vertical Flux Limit	72
III	LITTLE SCIENCE	73
6	RESEARCH AND DEVELOPMENT FOR FUTURE LIQUID XENON TPCs	74
6.1	Test Bed Apparatus Overview	74
6.2	Circulation System	76
6.3	Slow Control	76
6.4	Photomultiplier Tube (PMT)	77
6.5	Charge Amplifiers	78
6.5.1	Charge Amplifier Noise Behavior	80
6.6	Data Acquisition and Processing	82
6.6.1	Estimating Picoscope Dead Time	83
6.6.2	PMT Signal Processing	84
6.6.3	Charge Amplifier Signal Processing	84

6.7	High Voltage Feedthrough Design	87
6.7.1	Off The Shelf Feedthroughs	87
6.7.2	Custom Feedthroughs	92
6.8	Electric Fields in Test Bed	96
7	SOLUBILITY OF RADON DAUGHTERS IN LIQUID XENON	100
7.1	Motivation	100
7.1.1	Plate Out	102
7.2	Experimental Configuration and Method	103
7.2.1	Plate Out of ^{220}Rn Daughters	105
7.2.2	Data Collection	106
7.2.3	Calibration	107
7.2.4	Position Reconstruction	107
7.2.5	Fiducial Volume	108
7.3	Analysis	108
7.3.1	Number of ^{220}Rn daughters in the TPC	108
7.3.2	Data Selection	108
7.4	Results and Discussion	111
8	STUDIES OF DELAYED SINGLE ELECTRON SIGNALS	119
8.1	Motivation for Studying Delayed Single Electron Signals	119
8.2	Origin of Delayed Single Electron Signals	121
8.2.1	Photoionization on Grids	121
8.2.2	Photoionization of Impurities	121
8.2.3	Delayed Extraction of Trapped Electrons	122
8.3	Test Bed Studies Of Electron Trains	125
8.3.1	Radon Source and “Full TPC Configuration” .	125
8.3.2	Polonium Source and “Extraction Region Only” Configuration	131
8.4	Electron Train Study Summary	133
8.5	Discussion	139
IV	APPENDIX	142
A	DUMMY APPENDIX	143
	BIBLIOGRAPHY	144

LIST OF FIGURES

Figure 1	Superposition of 21 Sc rotation curves from galaxies with a large range of radii and luminosities. All galaxies have a distinctive flat rotation curve at large radii. Figure from [5].	4
Figure 2	CfA Redshift Survey result showing the distribution of galaxies in a strip on the sky about 6 degrees wide and 130 degrees long. The radial coordinate is redshift, in km/sec, calculated with a Hubble constant of 20km/sec/million ly.	5
Figure 3	Galactic rotation curve from [9]	6
Figure 4	(left) The visible light image from the Magellan telescope of the merging Bullet Cluster overlaid with the weak lensing measurement contours in green, and white 68.3%, 95.5%, and 99.7% confidence levels for the weak lensing peaks. (right) The Chandra x-ray image overlaid with the same weak lensing measurement. Figure from [20] .	8
Figure 5	(left) The FIRAS instrument on the COBE satellite mission measured the Cosmic Microwave Background (CMB) temperature to be 2.7377 ± 0.0038 K. (right) The FIRAS instrument also confirmed the perfect Planck black body spectral shape of the CMB radiation. Figures from [21] .	9
Figure 6	(top) The relative spatial resolution of COBE, WMAP, and Planck. Figure courtesy of NASA. (bottom) The Mollweide projection of the Planck 2013 CMB temperature map. The color scale represents fluctuations of $\pm 30 \mu\text{K}$ around a central value of 2.7377 K. Figure courtesy of ESA and the Planck Collaboration.	9
Figure 7	The angular power spectrum from Plank 2018 results [23]	11
Figure 8	The effect of baryons (left) and total matter (right) on the magnitude and location of CMB angular power spectrum peaks. [22]	11

Figure 9	The effect of curvature (left), dark energy (center), and equation of state (right) on the magnitude and location of CMB angular power spectrum peaks. [22]	14
Figure 10	The particles that comprise the standard model of particle physics, including names, spins, masses, and charges. It is also indicated which fermions interact with which bosons, e.g. gluons interact with the quarks but not with the leptons.	16
Figure 11	(left) The co-moving number density Y (left y-axis) resulting in the thermal relic density Ω_χ (right y-axis) for a dark matter particle of mass $m_\chi=100$ GeV. The solid black line is the annihilation cross section which yields the correct relic density and bands indicate cross sections that differ by successive factors of 10 from the “correct” annihilation cross section. (right) A band of natural values for a thermal relic χ that composes different percentages of the observed dark matter content. The width of the band is set by the deviation of g from g_{weak} in Equation 12. Figures from [31]	19
Figure 12	A Feynman diagram of a dark sector particle h interacting with atomic electrons. g' is the gauge coupling to A' in the dark sector, θ the kinetic mixing angle between A' and A , and g is the usual electromagnetic gauge coupling, $g = e$	23
Figure 13	Regions of mass-charge space ruled out for Lightly Ionizing Particle (LIP)s from several different sources. The dashed line limits apply in the case of a dark sector photon (our case of interest), and the dotted line is the limit without dark photons. Abbreviations: AC, accelerator experiments; Op, search for the invisible decay of ortho-positronium; SLAC, the SLAC millicharged particle search (51); L, the Lamb shift; BBN, big bang nucleosynthesis; RG, plasmon decay in red giants; WD, plasmon decay in white dwarfs; DM, dark matter searches; SN, Supernova 1987A. Figure from [38].	24
Figure 14	Recent limits on the flux of LIPs with charge e/f where f is the x-axis.	25

Figure 15	Contours in the (m_χ, g_χ) for two different temperature conditions for the hidden sector. The upper line is for a hidden sector that achieves 80% of the visible sector temperature after reheating, the lower line is for 30%. The hidden sector is a 1-generation flavor-free version of the minimal supersymmetric standard model. Figure adapted from [31].	26
Figure 16	Summary of Dark Matter (DM) detection schemes with illustrative Feynman diagrams. In all cases, the arrow to time is from left to right. (left) Standard Model (SM) particles can be collided at high energy facilities, which may produce DM particles χ . (center) DM particles χ may scatter with SM particles, leaving behind a characteristic signal. (right) DM particles in the galaxy may annihilate and produce SM particles, which producing signal in excess of expectations from standard astrophysical processes.	28
Figure 17	(left) Diagram of a dual-phase xenon time projection chamber. The time difference between S1 and S2 gives the depth (z) of the interaction, and (x, y) is reconstructed from the S2 signal. (right) Diagram summarizing the generation of the scintillation and ionization signal generation in dual-phase xenon time projection chambers.	35
Figure 18	(left) Plot illustrating the effect of recombination and detector effects on a line source (^{127}Xe), courtesy of E. Pease. (right) Field dependence of scintillation and ionization yield in LXe for 122 keV electron recoils (ER), 56.5 keV nuclear recoils (NR) and 5.5 MeV alphas, relative to the yield with no drift field from [59]	37
Figure 19	Plots showing combined energy contours in two common sets of axis units, for an example set of g_1 and g_2	38
Figure 20	Plot showing ER and NR bands from LUX. Solid lines are the ER and NR Gaussian means μ , dotted lines are $\mu \pm 1\sigma$. Figure from [56]	40

Figure 21	Plot showing spin-independent WIMP rates in common detector target materials, dots indicate typical thresholds for the targets. Xenon gains in favored SUSY parameter space ($M_\chi \gtrsim 100$ GeV) due to a kinematic enhancement ($M_\chi \sim M_{Xe}$) and a cross-section enhancement ($\sigma_{SI} \propto A^2$). Figure from [65]	43
Figure 22	Projected limits of next-generation dark matter detectors and areas where SUSY models predict the presence of WIMPs. Although Xe (LZ, green dashed) performs better for WIMP parameter space, Ge and Si (SuperCDMS, blue dashed) can access other light dark matter parameter space below 10 GeV. The plot was generated by http://dmtools.brown.edu/ 43	
Figure 23	Xenon 10 low-mass WIMP limit extended the range of the standard WIMP result.	45
Figure 24	(left) Top: Expected 1,2,3-electron signal rates for Sub-GeV DM with $\sigma_e = 10^{-36} \text{ cm}^2$ and Bottom: exclusion limit set with Xenon10 few-electron signals. (right) Exclusion limits for dark matter scattering through an electric-dipole moment (red) and through a very light (\ll keV) mediator (blue)	46
Figure 25	(left) Recent limits on solar axion coupling and mass (right) recent limits on galactic axion coupling and mass. Figure taken from [74].	47
Figure 26	Major components and dimensions of the LUX detector.	50
Figure 27	Field-shaping rings detail	51
Figure 28	A simplified diagram of the LUX cryogenic system. [75]	52
Figure 29	A photo of the LUX detector installed inside the water tank.	53
Figure 30	Backgrounds distributions in squared radius and height for expected (right) and measured (left) backgrounds in the energy range 0.9-5.3 keV _{ee} (2-30 phe S1) for the 85.3 live-day Run03 Weakly Interacting Massive Particle (WIMP) exposure. Black lines show the 118 kg fiducial mass. Units are log ₁₀ DRU _{ee} , electron equivalent differential rate units, i.e. keV _{ee} ⁻¹ kg ⁻¹ day ⁻¹ . Figure from [78].	54

Figure 31	Overview of the LUX trigger system. Figure from [79].	54
Figure 32	An example recorded event. Channels that do not pass the POD threshold are not recorded. The waveforms are summed over all channels to produce the S1 and S2 [79].	55
Figure 33	An example of Large Underground Xenon (LUX) pulse classification showing individual pulses.	57
Figure 34	Plot showing calibration sources (Figure from [58]). The axis label subscript c denotes corrected variables with calibration for geometrical effects and electron lifetime (these corrections are discussed in Section 4.6.2).	58
Figure 35	Doke plot used to fit g_1 and g_2 for LUX Run03 (Figure from [58])	59
Figure 36	Spatial dependence of pulse area corrections for S1 (left) and S2 (right) from an example ^{83m}Kr calibration. The red circle indicates normalization point. (Figure from [82])	61
Figure 37	(Left) A simplified 2D COMSOL model showing electric field lines and equipotentials for the LUX detector in Run03. A radially inward component is seen. (Right) The resulting edge S2 coordinates of a uniform distribution of electrons drifted under the electric field model is shown in solid blue. The edge S2 coordinates of from ^{83m}Kr data is in dashed red; it is consistent with the field model prediction. Figure from [82]	62
Figure 38	The effect of radial position mapping between S2 coordinates (left) and real coordinates (right). The top panels show a thin horizontal slice of the detector and the bottom panels show a thin vertical slice. The red and blue colors are to make the effect of the mapping visible. Note that squared radius in the bottom panels exaggerates the scale of the effect. Figure from [82]	63
Figure 39	Field map of Run03 produced by ^{83m}Kr S1a:S1b ratio. Because only a fraction of ^{83m}Kr produce separate S1a and S1b, the bins are large to accommodate reduced statistics. Figure from [82]	64

Figure 40	(Left) Plot showing the theoretical tritium beta spectrum with the spectrum obtained from data, and residuals. (Right) The ratio of data to theory convoluted with the detector energy resolution. Figure from [83]	65
Figure 41	(Left) The measured quanta yields shown with lines of equal energy. (Right) A plot depicting the expected initial quanta yields, N_{ion} and N_{ex} , compared with the measured yield of photons and electrons. The difference is caused by the energy dependence of recombination. Figure from [83]	65
Figure 42	(Left) The Electron Recoil (ER) band for in WIMP search energy range obtained from the tritium calibration. (Right) Leakage fraction of ER events below the Nuclear Recoil (NR) mean in the WIMP search energy range. Knowledge of the NR band comes from the DD calibration detailed in Section 4.6.4. Figure from [83]	66
Figure 43	(Right) Photo of the water tank interior showing the neutron conduit, which is raised during Deuterium-Deuterium (DD) calibration. (Left) Diagram of the DD generator and water tank neutron conduit during DD operation. Figure courtesy of E. Pease.	67
Figure 44	Calibration showing the NR band mean and width from the DD calibration. Figure from [62]	68
Figure 45	Improved spin-independent WIMP limit of the Run03 exposure following the DD calibration of LUX . The first Run03 limit is the gray line labelled “LUX 2014”, the improved Run03 observed limit is the black line labelled “This Result”. Figure from [86]	69
Figure 46	Large scale view of the experimental apparatus showing key parts.	75
Figure 47	Diagrams of two often used internal arrangements. The configuration (left) has both a drift and extraction region. The configuration (right) is “extraction region only”.	75
Figure 48	Pumping and instrumentation diagram of the test bed. Special symbols are labelled in the diagram, see key for other symbols. For readability, all gauges are not shown.	76

Figure 49	A diagram showing components of the slow control.	77
Figure 50	(left) Segmented anode showing the xenon-facing anode segments. (right) The wires on the top of the anode which lead to the charge amplifiers.	78
Figure 51	A picture of the CR-110 charge amplifier from the manufacturer's data sheet, shown with an equivalent circuit diagram.	79
Figure 52	A raw and shaped charge amp signal taken in -100C gaseous xenon, with the radon source plumbed in	79
Figure 53	(Left) original mounting of CR-110 charge amplifiers inside the experimental vessel. (Right) Mounting in the outer vacuum reduced heat load on the TPC.	80
Figure 54	Different lengths of BNC cable attached to a CR-110 test board.	81
Figure 55	(Left) Event showing charge amp with detector -100 C, 1.5 bar, gas only. (Middle) Effect of circulation pump on charge amp is to cause 500 Hz oscillation noise (-100 C, 1.5 bar, gas only). (Right) Same event as (middle), but zoomed-in time scale.	81
Figure 56	An event with the detector at -100 C, 1.5 bar, with liquid condensed to a level between extraction grid and anode. (left) is a long time trace view the raw and shaped charge amplifier signals. (right) is the same event, but zoomed in. The baseline restorer on the shaped charge signal allowed it to be used as a trigger.	82
Figure 57	(Left) Periodic noise from the Glassman 20 kV negative polarity voltage supply. (Right) Partial breakdown in R60 cable as picked up by charge amplifiers.	82
Figure 58	(top) Laboratory method to find the maximum Data Acquisition (DAQ) record time time. (bottom) Calculating dead time from maximum record rate.	83
Figure 59	Fitting the charge traces with a piece-wise defined linear rise and exponential fall.	85
Figure 60	(left) A choice of	85
Figure 61	86

Figure 62	An alpha event showing the Shockley-Ramo effect on the inner and outer ring segments of the anode.	87
Figure 63	A 12kV SHV weldable connector from vacuum supplier Kurt Lesker.	88
Figure 64	(left) The copper tape in this picture is sitting on top of a 1/2 -in swage connector. The swage connector captures a 1/2 in pipe, which has the 12 kV SHV feedthrough welded to the end. (right) 12 kV SHV weldable connector, inverted, clipped, and attached with a machined copper connector. The connector uses a screw to capture the SHV feed though, and the same screw to capture a stranded wire, visible in this picture, which is then fed through a hole drilled in the Polytetrafluoroethylene (PTFE) to connect to the wire grid frames. The wire was wrapped around the grid frame.	89
Figure 65	The same 12kV SHV feed through, now with a modified spring connection connecting the feed through to the grid frame. A close up of the cathode grid showing the spring connection is on the right	89
Figure 66	Oscilloscope showing baseline rate of single photons (left) compared to a high rate of single photons (right) caused by the high voltage feed through.	90
Figure 67	(Left) Full xenon breakdown as visible on the PMT trace. The large, saturated pulse is caused by the high intensity of light. This type of breakdown was often accompanied by an audible buzz, and a rise in current that would initiate a trip of the high voltage supply. (Right) a close up of the xenon-facing side of the feedthrough. Visible gaps where xenon gas is exposed to high fields are particularly problematic for breakdowns.	90
Figure 68	Top: (left) cathode connection side (right) SHV-20 connection side Bottom: (left) an example showing how the cable was attached to the stock SHV-20 feed though end (right) a custom cap fit over the connection, smoothing out triple points.	91
Figure 69	Effect of holding the feed through in place with PEEK zip ties was explored, effects were minimal.	92

Figure 70	The black line shows the aging observed in the course of normal operations. The red line shows breakdown tests of the SHV-20 feed though in gas, illustrating that the aging observed during operation was due to aging of the feed though. .	93
Figure 71	First attempt at a custom feed through built out of Swagelock parts combined with basic materials like PTFE and stainless steel rods. The orientation shown (left) was later inverted due to concerns of temperature stress and pressure stress on the PTFE ferrules. The feedthrough as assembled (center) was functional, but higher voltage capability was desired. The effect of adding a grounding braid (right) was found to decrease the voltage capability instead of increasing it. .	94
Figure 72	(top) Input to a COMSOL model simulating gaps between the grounding braid and dielectric of a high voltage feedthrough. (bottom) COMSOL output of the model, showing that peak fields arise when gaps exist between dielectric and grounding braid. Both images provided by W. Waldron.	95
Figure 73	Top: (left) Close up showing the PTFE ferrules and notch. (right) Close up of the sealed top connection; epoxy was added to prevent leaks between the dielectric and conductor rod . Bottom: (left) Threaded U-bend cathode connector (right) Feed through assembled and installed.	96
Figure 74	Top: (left) Sealed top connection with liberal epoxy use. A male Bendix pin was soldered to the cable conductor. (middle) SHV connector with female Bendix to mate with feedthrough (right) Grounded safety housing with SHV connector. Bottom: (left) Ends of the feedthrough were held in the Teflon stack. (middle) Close up showing cable conductor, PTFE dielectric, and grounding sheath pulled back (right) Grounding scheme for feedthrough cables.	97

Figure 75	(left) COMSOL model with specific cathode voltage and liquid level. (right) Analytic calculation following the McDonald notes [93], which shows how the peak fields vary with change in liquid level and cathode voltage. The voltages in the legend refer to the cathode voltage; the anode is held at ground.	98
Figure 76	Ranges for the electric fields in gas and liquid for different cathode voltages and liquid levels.	99
Figure 77	The ^{222}Rn decay scheme. The fast and slow chains are indicated.	101
Figure 78	Pathways to radon and radon daughter contamination.	102
Figure 79	Diagram of the test bed. For this study, the cathode is held at -6.0 kV, and the grid is held at -4.0 kV. $E_1^{\text{liq}} \approx 5.0 \text{ kV/cm}$, $E_1^{\text{gas}} \approx 10.0 \text{ kV/cm}$ $E_2 = 1.0 \text{ kV/cm}$. $E_3 = 2.7 \text{ kV/cm}$. The large gray regions represent the structural rings of PTFE. The line between the grid and anode represents the liquid xenon level. The xenon inlet pipes incoming gas directly into the liquid region, and the liquid outlet pulls from the level of the active region. A gas outlet (not pictured) also draws xenon gas into the circulation system to be purified.	104
Figure 80	An example a circulation path used for plate out is shown on the pumping and instrumentation diagram. During data-taking the radon source was bypassed. The typical liquid level is indicated on the diagram to show that the outlet drew from the liquid via a capillary, ensuring purification of the liquid xenon. A gas purge also purified the gas column in the detector.	105
Figure 81	The ^{220}Rn decay scheme. The fast and slow chains are indicated. Events in the plate out data sets are from the slow chain.	106
Figure 82	a) and (b) and (c) show the plateout conditions of datasets A, B, and C, respectively. The gray bands indicate time when data was being acquired. Dataset D (calibration) was taken following dataset A and consisted of a few hours.	109

Figure 84	Monte Carlo study to find the maximum distance a ^{212}Bi beta (2.2 MeV) on the cathode could penetrate into the drift region. The projected range (red) is the relevant curve for this analysis; it shows a beta is not expected to travel more than 1.2mm from the cathode.	113
Figure 85	For datasets A and B: (left) Distribution of events in z . (right) The same events distributed in the S1-S2 plane, showing selection criteria for candidate ^{212}Bi alpha events in the bulk liquid xenon.	114
Figure 86	For datasets C and D: (left) Distribution of events in z . (right) The same events distributed in the S1-S2 plane, showing selection criteria for candidate ^{212}Bi alpha events in the bulk liquid xenon.	115
Figure 87	An electron train spanning several ms. Pre-trigger and electron train regions are indicated along with the LUX event that originated the electron train. The inset shows the shorter time structure of e-burps. The y-axis is a proxy for phd/sample. Such figures of electron trains are generated from .dat files, not from .evt files. Figure courtesy of J. Xu.	120
Figure 88	Figure adapted from [71].	120
Figure 89	The average of many high energy S2s from LUX , plotted with logarithmic y-scale, showing a prominent photoionization feature. After the photoionization, an instrumental effect is visible: for the highest-energy events, one to a few PMTs often do not return to baseline quickly, which gives the single electrons in the following train artificially higher areas. Figure from J. Xu. . . .	122
Figure 90	(left) The per-event rate of single electron signals 20 to 150 μs after the main S2 of a single-scatter type event as a function of the main S2 size. The fit line and residuals show a good proportionality in the relation. (right) The per-event rate of single electron signals, for events with the main S2 between 5000 and 10000 phe, as a function of the O ₂ -equivalent concentration of impurities in liquid xenon. Figures from [109]. .	123

Figure 91	(left) The absolute Electron Extraction Efficiency (EEE) measured by Gushchin from [111]. The Liquid Xenon (LXe) points were re-colored red. (right) Two relative EEE measurements from modern experiments, Xenon100 and PIXEY, compared to Gushchin. The plot is from the PIXEY result [112], where the authors fit their result with a quadratic function ($y = ax^2 + bx + c$). The fit to the PIXEY data (black dashed line) is scaled by a constant and applied to the Xenon100 data (blue dotted line).	124
Figure 92	(left) Effect of anode saturation measured as deviation from signal linearity as a function of the peak anode current. (right) Capacitor depletion in the R8778. The blue trace shows the largest S2-like pulse that can be generated with a LUX voltage divider base (generated with a $1\ \mu s$ square pulse on a blue LED); the 2% and 5% deviations from linearity is shown. The fall-off indicates the capacitor is depleted and the photomultiplication process is temporarily turned off. The black trace shows the effect of adding an extra capacitor between dynodes Dy9-Dy10. Figures are from [54], which also contains more information about the LUX PMTs and bases.	127
Figure 93	A series of PMT masks made from Conflat (CF) blanks which reduced the light collection area of the PMT to approximately 2%, 5%, 15%, and 10% (clock-wise from top left). The masks were installed in place of the PMT shield grid, and similarly to the PMT grid, they were kept at the same bias voltage of the PMT	129
Figure 94	The single phe spectrum from the PMT with a bias voltage of 1300 V. The spectrum was obtained by using a variable gain amplifier to 100x amplify the PMT signal (at room temperature, in vacuum). A NIM! (NIM!) quad discriminator was used to externally trigger the picoscope. The waveforms were summed in a fixed window, and the results were histogrammed.	129
Figure 95	Bunemann's condition for grid transparency. Cathode voltages from -7.24 kV to -4 kV should result no charge being collected on the grid.	130

Figure 96	Ionization charge vs. drift time presented in both S2 (left) and charge amplifier voltage from the central anode segment (right). A ~50% drop in signal is visible between events occurring above the grid and events occurring below the grid. The effect of purity of also visible in the fall off charge signal with drift time. The points under the obvious line in the charge amplifier plot are from events which share charge with other anode segments.	131
Figure 97	132
Figure 98	133
Figure 99	^{210}Po decay scheme.	134
Figure 100	Different field strength depending on particle trajectory. Adapted from [122]	134
Figure 101	(top) Recoiling ^{206}Pb nucleus. (bottom) ^{210}Po alpha decay. Capacitor depletion is visible in the S2 shape, and $\sim 20 \mu\text{s}$ dead time between the S2 and start of the electron train. Insets on both (top) and (bottom) show detail of the event S1 and S2, and electron train segments. From [117]	135
Figure 102	Stacked waveforms and fits from a dataset with cathode voltage at -4 kV. From [117]	136
Figure 103	Examples of the charge amplifier mirror effect on one anode segment. The example (left) is an event where charge is collected on the anode segment, and so the charge amplifier signal trace shows a step. The example (right) shows the charge trace mirroring the PMT, but with no charge collected on the anode segment.	137
Figure 104	Histogram of charge amplifier step height for a cathode voltage of -3 kV. The histogram is skewed by wire position-dependent recombination; the same effect is visible in Figure 98 (right). This mean of the fit was converted to electrons using the manufacturer's specification of charge amplifier gain, 1.4 V/pC. 5.5mV converts to 24500 electrons.	137
Figure 105	Single electron and photoelectron peaks obtained in liquid conditions for a PMT bias voltage of 1500 V.	138

Figure 106	κ is the extraction efficiency as in Equation 48, so unextracted electrons should scale as $(1 - \kappa)$. In this thesis, (a) is reference [111], an absolute measurement of EEE; (b) is reference [112], a relative measurement of EEE. The methods use different methods and assumptions; they are shown to illustrate that the fast component follows the behavior trend of what is expected from unextracted electrons.	139
Figure 107	140

LIST OF TABLES

Table 1	A summary of the fit parameters and derived quantities from Planck’s 2018 results [23].	15
Table 2	Possible dark sector portals, related dark matter candidates, and operator that connects the dark sector to the SM	21
Table 3	Dimensions of the of the anode segments. 1 refers to the inner-most segment or “bullseye”, 2 refers to the inner ring, 3 to the outer ring and full to the entire anode, which includes inactive area that is not instrumented with charge amplifiers.	78
Table 4	Summary of plate out and data-taking conditions. Data sets A and B are taken after circulating radon gas and data set C, background, had no radon circulation. Data set D was taken following dataset A, and radon was circulated in a liquid xenon environment, purposefully introducing radon into the detector bulk to calibrate the detector.	107
Table 5	Calculations of fiducial volume. Liquid level is taken to be 14 ± 1 mm. Density of LXe near boiling point is 2.9 g/mL.	108
Table 6	Number of detected alpha particle events whose energy determination was consistent with ^{212}Bi decay to ^{208}Tl . Live times are quoted in Table 4	113
Table 7	Using observations from 6, proceed through solubility calculation.	118

ACRONYMS

- SM Standard Model
BSM Beyond the Standard Model
SUSY Supersymmetry
MSSM Minimal Supersymmetric Model
LSP Lightest Supersymmetric Particle
WIMP Weakly Interacting Massive Particle
LIP Lightly Ionizing Particle
CDM Cold Dark Matter
DM Dark Matter
MOND Modified Newtonian Dynamics
NFW Navarro-Frenk-White
CMB Cosmic Microwave Background
GUT Grand Unified Theory
LSP Lightest Super Partner
BBN Big Bang Nucleosynthesis
GMSB Gauge-Mediated Supersymmetry Breaking
LUX Large Underground Xenon
LXe Liquid Xenon
TPC Time Projection Chamber
SURF Sanford Underground Research Facility
ER Electron Recoil
NR Nuclear Recoil
VUV Vacuum Ultra Violet

- DPF Data Processing Framework
LUG LUX Electronic Log
DAQ Data Acquisition
FPGA Field Programmable Gate Array
POD Pulse Only Digitization
ADC Analog-to-Digital Converter
SE Single Electron
SPHE Single Photoelectron
LRF Light Response Function
RQ Reduced Quantity
DD Deuterium-Deuterium
PVC Polyvinylchloride
MFC Mass Flow Controller
HV High Voltage
SHV Safe High Voltage
SS Stainless Steel
CF Conflat
PMT Photomultiplier Tube
QE Quantum Efficiency
EEE Electron Extraction Efficiency
LBNL Lawrence Berkeley National Laboratory
PTFE Polytetrafluoroethylene
PEEK Polyether ether ketone
RMS root mean square
CCS Collisional Cross Section
PAI Photo Absorption Ionization
FVP Fermi Virtual Photon

1

INTRODUCTION

I was dreamin' when I wrote this, forgive me if it goes astray.

— Prince, 1999, 1989

This Thesis is laid out in three main sections. The first section deals with the evidence for dark matter, theoretical background for different dark matter candidates, and an overview of experimental strategies to detect dark matter, going into detail for one particular detection strategy, the dual-phase [LXe](#) Time Projection Chamber ([TPC](#)).

The second section, Big Science, delves into details about the [LUX](#) detector, a dual-phase [LXe TPC](#), and presents a search for the [LIP](#) dark matter candidate carried out with [LUX](#) data.

The last section, Little Science, describes an R&D test bed that was built at L ([LBNL](#)) over the course of this PhD and describes two studies completed with the test bed.

PART I

THEORETICAL CONTEXT AND EXPERIMENTAL STRATEGIES

This section describes the theoretical foundation for the analysis presented in [Part II](#). It includes an overview of the Standard Cosmology...

2

THEORETICAL BACKGROUND

2.1 A LITTLE HISTORY

Our understanding of the universe develops in a leap-frog of theory and observation, one catching up to and surpassing the other as technology improves, to be passed in turn by a new idea or new observation. The picture of dark matter commonly accepted today is much different than what Zwicky anticipated in 1933 when he found that the velocity dispersion of the galaxies in the Coma Cluster was much larger than expected from the Virial Theorem [1]. This observation is typically cited as popularizing the term “dark matter”, and starting the hunt for the mysterious invisible substance. Zwicky postulated that the faster rotation was caused by dark matter consisting of cold gas or stars and both macro- and micro-scopic solid bodies, and estimated that there was about 400 times more dark matter than visible matter. Smith, a contemporary of Zwicky’s, did a similar analysis with the Virgo Cluster and his results yielded a much smaller dark matter to visible matter ratio [2]. Meanwhile, many in the astrophysics community disagreed with an underlying assumption of these analyses and argued that galaxy clusters are not at equilibrium so the Virial Theorem does not apply [2]. At the time, the only consensus reached was that more information was needed to understand the dynamics of galaxy clusters.

In the 1970’s, a new technology called the image tube spectrograph allowed Vera Rubin and Kent Ford, the developer of the spectrograph, to measure the rotational velocity of the Andromeda Galaxy at different points along its radius (called a galactic rotation curve) [3]. The new data was of higher quality than previous attempts at measuring galactic rotation curves, and the result, that the galaxy was rotating faster than expected at large radius, indicating “hidden mass”, was soon replicated by others [2]. Over the next decade, a significant number of galactic rotation curves were obtained, all showing essentially the same result: galaxies were rotating faster than expected at high radii, indicating that the mass of galaxies continued to grow past where their lights dimmed. A figure showing this characteristic behavior in 21 galaxies from a 1980 review paper by Rubin, Ford, and Thonnard is shown in Figure 1. Another

argument in favor of dark matter came from contemporary numerical simulations of galactic gravitational dynamics. At first, many simulations showed that disk galaxies were unstable, in contradiction with many observations [2]. However, Ostriker and Peebles demonstrated that if the galactic disk was embedded in a massive (i.e. gravitationally interactive) spherical halo, the disk was stable [4].

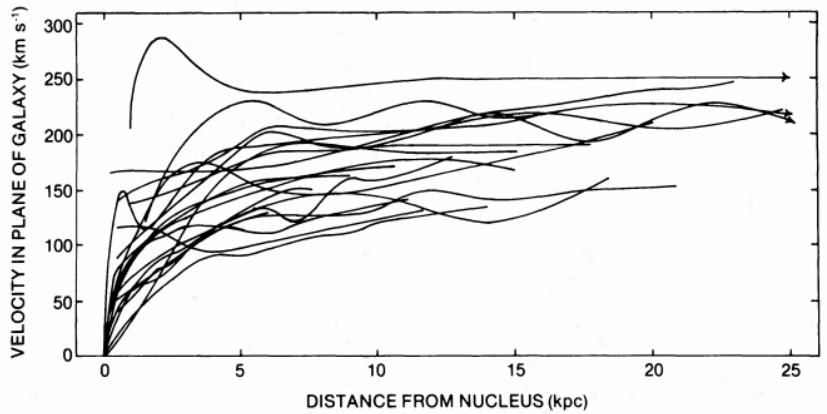


Figure 1: Superposition of 21 Sc rotation curves from galaxies with a large range of radii and luminosities. All galaxies have a distinctive flat rotation curve at large radii. Figure from [5].

In order to explain the behavior of galactic rotation curves without dark matter, Milgrom proposed Modified Newtonian Dynamics (**MOND**) in a trio of 1983 papers, [6], [7], [8]. Milgrom showed that if Newtonian dynamics was modified from $F = ma$ to $F = ma/a_0$, for a $\ll a_0 \approx 1.2 \times 10^{-10} m/s^2$ the observed galactic rotation curves could be accounted for without requiring any hidden or dark matter. Milgrom's goal in these first papers describing **MOND** was to present an approximate limit of some as-yet unknown full theory, which he and others went on to develop in the following decades [2]. However, theoretical and technological advancements in the fields of cosmology and astronomy have made **MOND** an unsatisfying theory, unable to explain several observed phenomena. Of these phenomena, gravitational lensing and **CMB** are discussed further below.

Big-Bang cosmology had a large success in 1965 with Penzias and Wilsons' observation of the **CMB**. It was in the 1980's however, that cosmology, particle physics, and astronomy became tied together as they are understood today, and dark matter came to refer to an as yet undiscovered particle species and not the cold gas and stars of Zwicky's day [2]. The root of this paradigm shift was in the new theory of cosmological inflation [2]. Inflation refers to a period of exponential expansion 10^{-36} to 10^{-33} seconds after Big Bang. Without an inflationary period, fluctuations would

be washed out as the universe expanded, leading to a universe devoid of structure. Inflation, however, provides mechanism for quantum fluctuations to be ‘blown up’ and seed the structure observed by the 1982 CfA redshift survey (Figure 2). Numerical simulations to reproduce the structure seen by the CfA redshift survey benefited from new improvements in processing speed and numerical techniques, and also from the new theory of inflation, which provided a physical reason for initial density perturbations [2]. The structure was reproduced only in the presence of gravitationally-interacting dark matter. It is interesting to note here that these cosmological simulations were largely insensitive to any additional, non-gravitational interactions the dark matter had, as long they were sufficiently weak. However, the simulations did require the dark matter to be non-relativistic or “cold”. Such dark matter is referred to as Cold Dark Matter (**CDM**), and plays a prominent part in the standard cosmology to describe the structure and evolution of our universe at all scales.

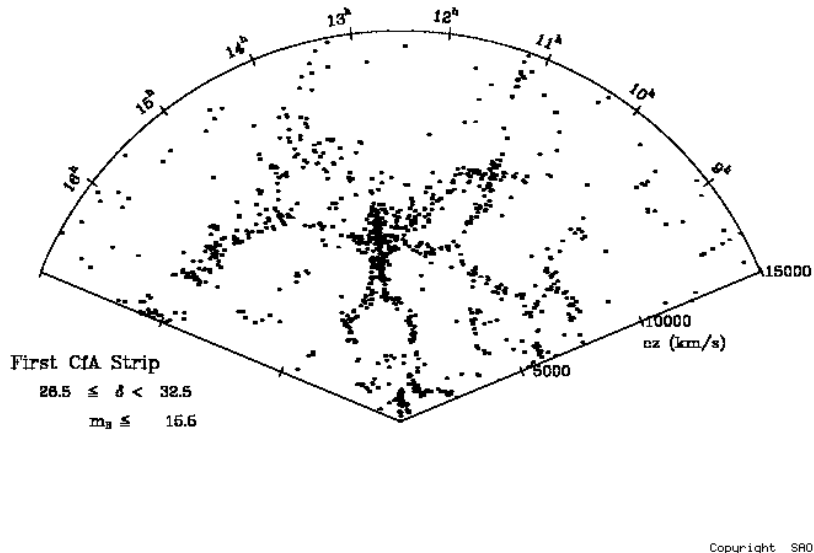


Figure 2: CfA Redshift Survey result showing the distribution of galaxies in a strip on the sky about 6 degrees wide and 130 degrees long. The radial coordinate is redshift, in km/sec, calculated with a Hubble constant of 20km/sec/million ly.

2.2 EVIDENCE FOR DARK MATTER

The previous section gave an overview of why **CDM** has become, over the last century, the leading paradigm to explain the small and large-scale

structure observed in our universe. The following subsections deal with particular pieces of evidence, discussed in detail.

2.2.1 GALAXIES AND CLUSTERS

Galactic rotation curves were discussed above, as evidence for dark matter halos. Here we further discuss the properties of dark matter halos. An example of a galactic rotation curve of a spiral galaxy showing the presence of an inferred dark matter halo is shown below in Figure 3. Each side of Figure 3 shows the same galaxy, NGC 3198, but fit with a different disk and halo model. In this particular example from 1985, the authors note their uncertainty about which halo model is the correct one: “Should one seriously consider the case where the amount of visible matter is negligible with respect to the amount of dark matter [Figure 3 (left)]? Or is the maximum disk case [Figure 3 (right)] closer to the truth?” [9]. A decade later, in 1996, Navarro, Frenk and White published a paper describing high-resolution simulations of CDM, which could all be fit with a universal dark matter halo profile [10]. This formula became known as the Navarro-Frenk-White (NFW) profile; it is still widely used today, and is the basis for many direct detections experiments, including LUX.

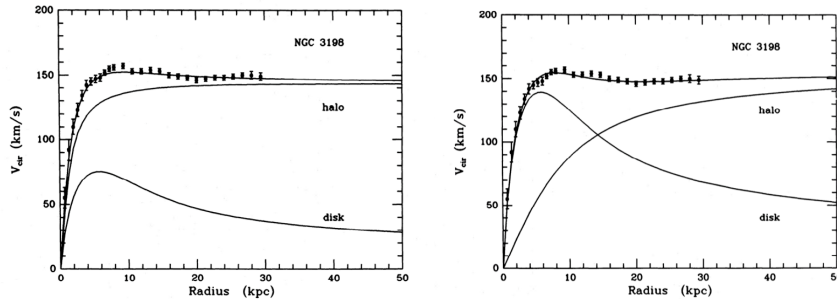


Figure 3: Galactic rotation curve from [9]

The astrophysics community is near unanimous that galaxies have a dark matter component. Today, research continues into the particular shape of the dark matter profile. While NFW is in common use and agrees with many observations, it is not consistent with observations of low surface brightness and dwarf galaxies [11], [12]. This known as the core-cusp problem: NFW galaxies have an over-density of dark matter at small radius (cuspy), while dwarf galaxies favor flatter density profiles (core). Some argue that such behavior may be a consequence of the nature of dark matter, or that current simulations are not sufficient to properly understand dwarf galaxies [13]. Others argue that a cusp can be changed to a core via baryonic feedback that arises in simulations of active galactic nuclei [14].

Other current research into dark matter halos centers on the globular clusters and stars that orbit the Milky Way. These researchers look for evidence of halo substructure and streams of dark matter from the movements of stars orbiting the Milky Way. Data from the Gaia satellite, launched in 2013, calls into question whether dark matter halos are truly in equilibrium, which has consequences for direct detection experiments, as it would change the expected dark matter recoil spectrum [15] [16]. In addition to the stars and globular clusters orbiting the Milky Way, there could be clusters of dark matter more dense than the surrounding halo. Telescope data shows evidence for dark matter halo substructure in the Milky Way [17], and simulations expect upcoming data from LSST to further contribute to understanding of Milky Way halo substructure and rule out certain dark matter halo models [18].

Galaxy clusters make up some of the strongest direct evidence for dark matter though the method of gravitational lensing. A gravitational lens is created when a massive object is located between a light source and an observer. General relativity requires photons to propagate on the null geodesics of spacetime, meaning the path the light takes from the source will be bent by the distorted space-time of the the massive object. Thus images of background galaxies are distorted by invisible mass along the line of sight from the observer. Being dependent on general relativity, and therefore Newtonian dynamics, the numerous observations of gravitational lensing in large structures strongly disfavor MOND.

There are a few types of gravitational lensing: strong, weak, and microlensing. Weak lensing has been used to observe dark matter in large scale structures (galaxy clusters); the other types of lensing are not treated here. In weak lensing, the light sources are far away from the foreground mass (or the mass is small). Several light sources are required, and the location of the mass is statistically reconstructed. The Bullet Cluster (1E0657-558) is one of the most dramatic weak lensing measurements to date: it is actually the collision of the galaxy cluster 1E0657-56 and smaller cluster (the “bullet”) [19]. The x-ray image of the collision, by the Chandra x-ray observatory, shows the location of the baryonic matter. The baryonic matter suddenly slowed down upon the collision, emitting shock x-rays [19]. The authors of [19] call it “a textbook example of a bow shock”, indicating the x-ray behavior is well understood. A few years later, Clowe et al. also call the Bullet Cluster “a direct empirical proof of the existence of dark matter.” Their weak lensing observations show the location of the large, invisible mass centers of the two clusters to be offset from the location of the baryonic matter at a significance of 8σ [20]. In the collision, the dark matter halos of the two clusters are expected to pass through each other without slowing down, while the baryonic matter in the two clusters interacts, slowing down dramatically and producing x-rays. The

weak lensing measurement is shown overlaid with the visible and x-ray images in Figure 4.

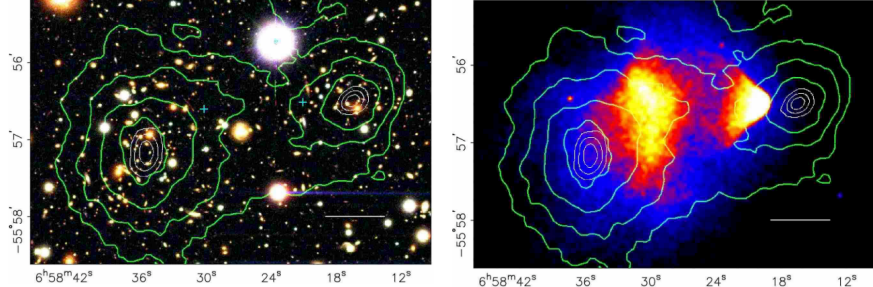


Figure 4: (left) The visible light image from the Magellan telescope of the merging Bullet Cluster overlaid with the weak lensing measurement contours in green, and white 68.3%, 95.5%, and 99.7% confidence levels for the weak lensing peaks. (right) The Chandra x-ray image overlaid with the same weak lensing measurement. Figure from [20]

2.2.2 COSMIC MICROWAVE BACKGROUND

In the thermal history of our universe, the term recombination refers to the epoch when temperatures had cooled enough to allow electrons and protons to combine into hydrogen, leaving photons to propagate freely through the universe. The photons should have decoupled from the matter as a black body peaked at the temperature of recombination, ≈ 3000 K. The relic radiation from this epoch is visible today as the [CMB](#), where the continuing expansion of the universe has redshifted the peak of the black body spectrum to ≈ 2.7 K. The [CMB](#) photons are also referred to as the light of last scattering, referring to the interaction the photons had with free electrons before the electrons became bound to protons in hydrogen. The temperature of the [CMB](#) was precisely measured to be 2.7377 ± 0.0038 K by the COBE mission, which also confirmed its perfect adherence to a black body spectrum [21] (Figure 5).

While the COBE satellite mission's measurements of the [CMB](#) provided strong support for the Big Bang model of cosmology, it was COBE's discovery of anisotropies in the [CMB](#) that eventually led to powerful evidence for [CDM](#). Since COBE, two more [CMB](#) satellite missions, WMAP and Planck, have launched and gathered data, each with successively higher spatial and energy resolution. The relative resolutions of COBE, WMAP, and Planck are shown in Figure 6 along with the full Planck [CMB](#) anisotropy map. The scale of the anisotropy fluctuations represent a scale of $\pm 30 \mu\text{K}$; the [CMB](#) power spectrum remains the most perfect black body spectrum observed in nature.

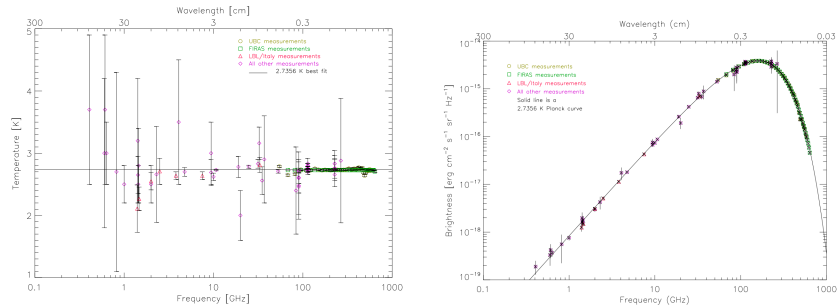


Figure 5: (left) The FIRAS instrument on the COBE satellite mission measured the CMB temperature to be 2.7377 ± 0.0038 K. (right) The FIRAS instrument also confirmed the perfect Planck black body spectral shape of the CMB radiation. Figures from [21]

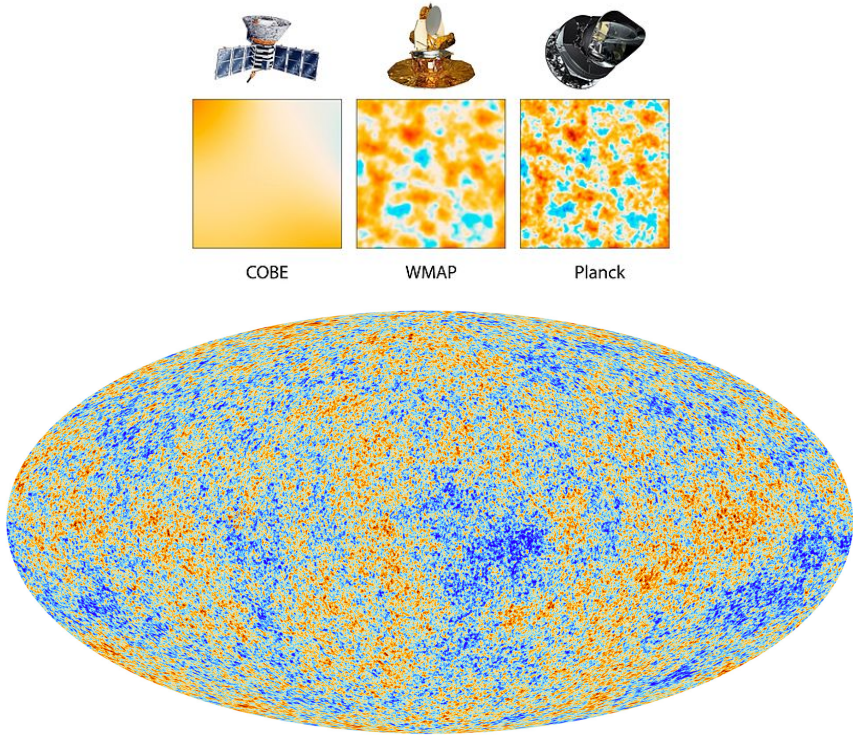


Figure 6: (top) The relative spatial resolution of COBE, WMAP, and Planck. Figure courtesy of NASA. (bottom) The Mollweide projection of the Planck 2013 CMB temperature map. The color scale represents fluctuations of $\pm 30 \mu\text{K}$ around a central value of 2.7377 K. Figure courtesy of ESA and the Planck Collaboration.

The fluctuations $\Delta T(\theta, \phi)$ of the CMB map shown in Figure 6 can be decomposed into its basis components via Fourier analysis, where each expansion component is represented by the spherical harmonics, Y_{lm} :

$$\Delta T(\theta, \phi) = \sum_{l=2}^{\infty} \sum_{m=-l}^l b_{lm} Y_{lm}(\theta, \phi) \quad (1)$$

The sum leaves out the $l = 0$ (mean) and $l = 1$ (dipole Doppler shift caused by movement of the earth) components, which were subtracted from the CMB temperature map, leaving only the fluctuations as in Figure 6. The power spectrum of the temperature fluctuations, which is calculated by squaring Equation 1, averaging it over all points that have the same angular separation θ , and performing an integral over all m (because the temperature anisotropies have no preferred direction), encodes all the statistical variation in the CMB sky (see, e.g. [22] for a derivation). The angular correlations of the different multipole moment l are typically extracted from this power spectrum and plotted as function of l and the coefficients C_l from the power spectrum. This quantity is referred to as the angular power spectrum and takes the form:

$$D_l^{TT} = \frac{l(l+1)}{2\pi} C_l \quad (2)$$

where the TT superscript denotes temperature anisotropies (polarization anisotropies, not discussed here, can be parameterized similarly). The latest angular power spectrum from Planck is shown in Figure 7.

The location and magnitude of peaks in the angular power spectrum (Figure 7), constrain the curvature, content, and evolution of our universe. The physical interpretation of the CMB is as follows: photons from the time of last scattering, newly free to propagate through the universe, carry information about the density fluctuations in the plasma from which they decoupled. The plasma, which was then composed of photons, baryons, and dark matter, behaved as an oscillator driven by gravitational attraction, with a restoring force from the fluid pressure of the plasma. The maxima of the angular power spectrum indicate extrema, overdensities or underdensities, in the plasma. The presence of baryons increases the magnitude of odd peaks relative to even peaks. The physical interpretation of this is that baryons add inertia to the oscillator system, causing an increase in compression (odd) compared to expansion (even) [22]. The angular power spectrum peaks are sometimes referred to acoustic peaks, as the oscillations that produced them were longitudinal and depended on density, much like sound waves. The presence of dark matter is apparent in the relative heights of the second and third peak in the spectrum.

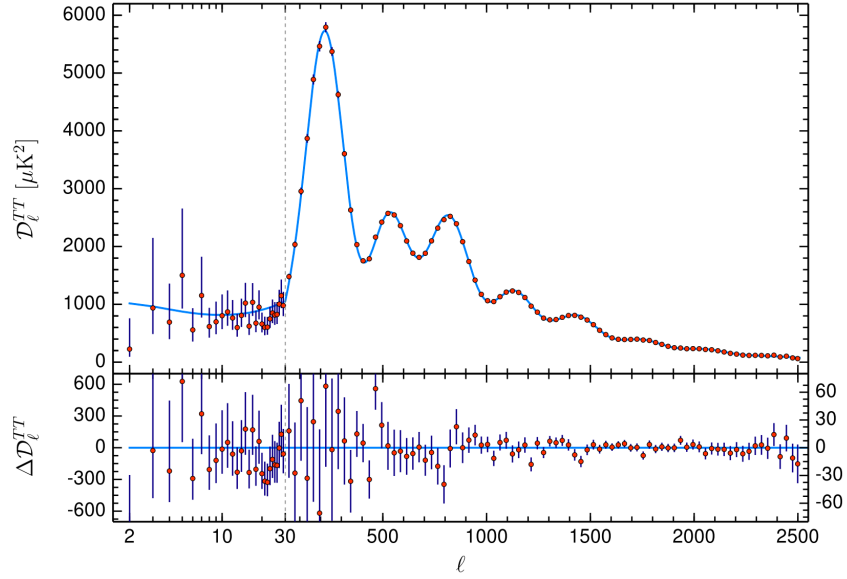


Figure 7: The angular power spectrum from Planck 2018 results [23]

The driving force of the oscillator is total matter content (baryons + dark matter,) which contributes to odd peaks, while baryons contribute characteristically to the even peaks. A third peak that is similar or larger than a second peak indicates that the matter content at the time of recombination was dominated by dark matter. A useful demonstration of the effect of baryons and total matter on the angular power spectrum is shown in Figure 8.

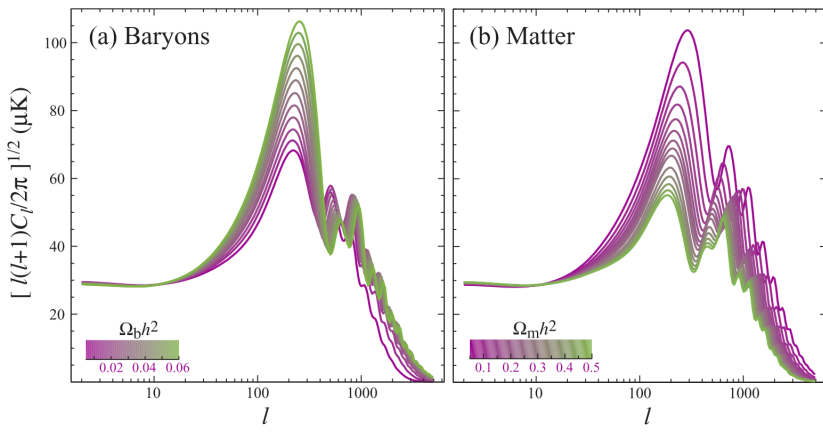


Figure 8: The effect of baryons (left) and total matter (right) on the magnitude and location of CMB angular power spectrum peaks. [22]

The measure of the dark matter content and baryon content of today's universe can be extrapolated from fitting the [CMB](#) angular power spectrum as in Figure 8. The results from the Planck 2018 angular power spectrum ([23]) are:

$$\Omega_{cdm} = 0.2696 \pm 0.0047 \quad (3)$$

$$\Omega_b = 0.0495 \pm 0.0005 \quad (4)$$

Each Ω_x represents the fraction of today's mass-energy density comprised by constituent x . These values do not add to one because a large fraction of the mass-energy density of the universe is comprised of dark energy, which we have left discussion of until the next section. However, note that these two values alone measure dark matter to comprise 84% of the matter in our universe.

2.3 STANDARD MODELS

Thus far we have focused only on the astrophysical and cosmological evidence for particle [CDM](#). [CDM](#) plays a central role in the standard model of cosmology, known as Λ [CDM](#) ("Lambda" - [CDM](#)). In this section, we briefly summarize the standard models of cosmology and particle physics.

2.3.1 THE STANDARD COSMOLOGY

The standard Λ [CDM](#) cosmology is based on the Einstein field equations:

$$R_{\mu\nu} - \frac{1}{2}g_{\mu\nu}R = \frac{8\pi G}{c^4}T_{\mu\nu} + \Lambda g_{\mu\nu} \quad (5)$$

where $R_{\mu\nu}$ is the Ricci tensor, R is the Ricci scalar, and $g_{\mu\nu}$ is the metric tensor. $T_{\mu\nu}$ is the stress-energy tensor, G is Newton's gravitational constant, c is the speed of light in vacuum, and Λ is the cosmological constant. The equation relates the geometry of space-time (on the left hand side) to the energy content of the universe (on the right hand side).

Einstein originally introduced the cosmological constant Λ to counteract gravity and produce a steady-state universe. Today, however, we know that the universe is expanding, and that the rate of expansion is accelerating. The second fact, first evidenced by supernova Type Ia measurements [24] [25], is what led to the modern interpretation of Λ as dark

energy. Today, we understand Λ to represent a “vacuum energy” associated with space-time itself, rather than its matter content. It is the source of the accelerating expansion of the universe, sometimes referred to as “negative pressure” or “gravitational repulsion”, and it is the dominant component of mass-energy density in our universe (see Table 1).

The Einstein field equations are solved with the Friedman-Lemaitre-Robertson-Walker metric (not shown here, see e.g. [26], [27]), which describes the symmetries we observe in our universe and therefore require of our model: isotropy and homogeneity. The solution yields the Friedman equation (Equation 6), which details how the addition of different energy sources (matter, radiation, dark energy) change the expansion rate of the universe. The rate of expansion is given by the Hubble constant $H(t)$ (a slight misnomer because it can change over time scales \sim history of our universe). It is defined as $H(t)^2 \equiv \frac{\dot{a}(t)}{a(t)}$, where a is the so-called scale factor, which is a dimensionless factor that parametrizes the size of the universe. The Friedman equation, given below, delineates how the Hubble constant changes with the energy content ρ_{tot} and curvature k of our universe.

$$H(t)^2 \equiv \left(\frac{\dot{a}(t)}{a} \right)^2 = \frac{8\pi G}{3} \rho_{tot}(t) - \frac{k}{a(t)^2} \quad (6)$$

The Friedman equation yields a quantity known as the critical density ρ_c , which is the density for a flat universe ($k = 0$).

$$\rho_c(t) = \frac{3H(t)^2}{8\pi G} \quad (7)$$

A species x is defined as having a fraction of the mass-energy density $\Omega_x(t) = \rho_i(t)/\rho_c(t)$. The individual Ω_x have different time evolutions according to their equation of state (see e.g. [26], [27], for a complete, pedagogical treatment). After treating equations of state, the Friedman equation can be re-written in a more convenient form:

$$\frac{H^2}{H_0^2} = \frac{\Omega_{r,0}}{a^4} + \frac{\Omega_{m,0}}{a^3} + \Omega_{\Lambda,0} + \frac{(1 - \Omega_{tot,0})}{a^2} \quad (8)$$

where the 0 subscript denotes today’s value, r denotes radtion, m denotes mater, and Λ denotes dark energy. Note that the last term disappears when $\rho_0 = \rho_c$, that is, if our universe is flat. Equation 8 makes a powerful statement: by measuring the energy content of the universe, we can tell the history and fate of the Universe. This is the core of Λ CDM – it is essentially a system of equations, which, when solved, can describe the

history and predict the future of the universe in terms of a few measurable parameters (e.g Ω_x).

The Planck collaboration fits for a standard, 6 parameter ΛCDM , from the CMB. This fit includes some parameters specific to the intricacies CMB measurements, as well as the familiar Ω_x density parameters from Equation 8. The 6 fit parameters¹ are: $\Omega_b h^2$, $\Omega_{cdm} h^2$, τ , $\ln(10^{10} A_s)$, n_s , and $100\theta_{MC}$. Other quantities are derived from these parameters. A summary of the parameters, derived quantities, and their values is given in Table 1. Note that the parameter A_s is the amplitude of curvature fluctuations in the CMB angular power spectrum (Figure 7). The effect of baryons and dark matter on the angular power spectrum were discussed in Section 2.2.2. Similarly, dark energy content, curvature, and equation of state of the universe also produce visible effects (see in Figure 9). Namely, dark energy and curvature determine the magnitude of the first peak, and curvature determines peak locations.

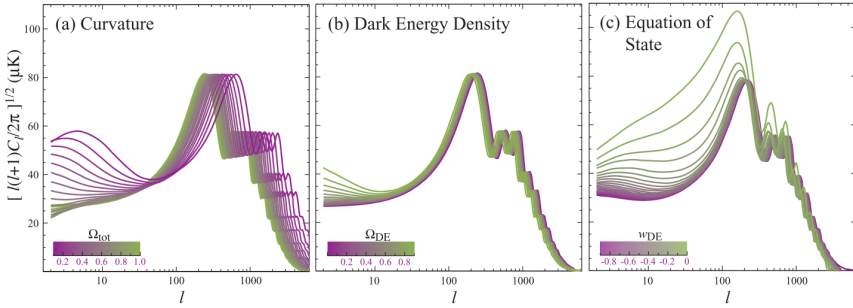


Figure 9: The effect of curvature (left), dark energy (center), and equation of state (right) on the magnitude and location of CMB angular power spectrum peaks. [22]

2.3.2 THE STANDARD MODEL OF PARTICLE PHYSICS

The SM of particle physics describes all the currently known matter particles and force carrier particles, which can also have mass, and which dictate interactions between the matter particles. As of 2012, it also includes a mass generation mechanism from the Higgs boson. The SM is formulated using the principles of Quantum Field Theory, where symmetries in the Lagrangian give rise to conserved physical quantities and thereby determine the rules for interactions.

¹ The density parameters are often reported as $\Omega_x h^2$ since the main source of error in their measurement comes from the Hubble constant H_0 . h is a dimensionless parameter defined as: $h = H_0/(100 \text{ km s}^{-1} \text{ Mpc}^{-1})$

Table 1: A summary of the fit parameters and derived quantities from Planck's 2018 results [23].

Fit Parameter	Definition	Planck TT spectrum
$\Omega_b h^2$	baryon density	0.02212 ± 0.00022
$\Omega_{cdm} h^2$	CDM density	0.1206 ± 0.0021
$100\theta_{MC}$	angular acoustic scale	1.04077 ± 0.00047
τ	optical depth	0.0522 ± 0.0080
$\ln(10^{10} A_s)$	curvature fluctuations	3.040 ± 0.016
n_s	spectral index	0.9626 ± 0.0057
Derived Quantity	Definition	Planck TT spectrum
Ω_b	baryon content	0.0495 ± 0.0005
Ω_{cdm}	CDM content	0.2696 ± 0.0047
Ω_m	matter content	0.321 ± 0.013
Ω_Λ	dark energy content	0.679 ± 0.013
H_0 [km s ⁻¹ Mpc ⁻¹]	Hubble constant	66.88 ± 0.92
Age [Gyr]	age of the universe	13.830 ± 0.037
k	curvature	consistent w/ $k = 0$

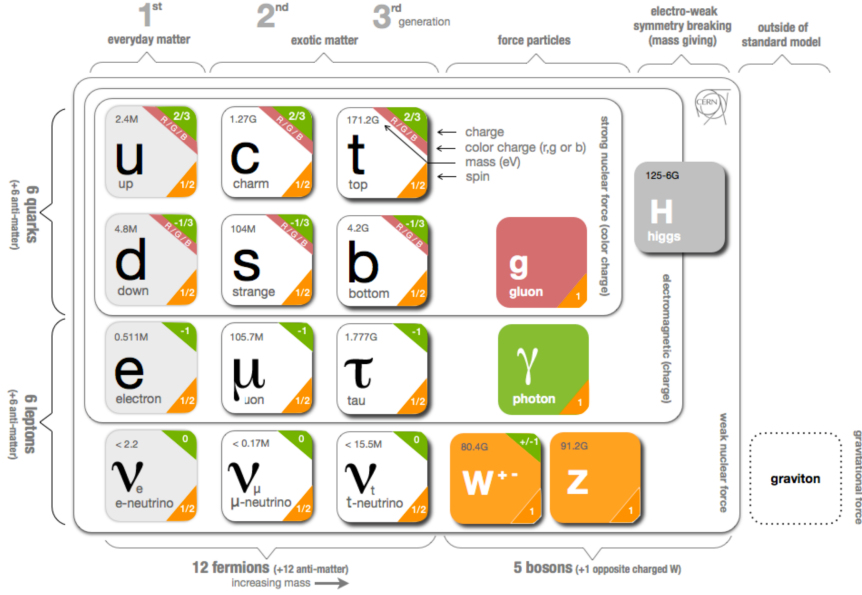


Figure 10: The particles that comprise the standard model of particle physics, including names, spins, masses, and charges. It is also indicated which fermions interact with which bosons, e.g. gluons interact with the quarks but not with the leptons.

The known particles of the SM are shown in Figure 10, along with a theoretical force carrier for gravity, the graviton. These particles are typically grouped into categories: fermions and bosons. Fermions comprise all the known matter particles and are spin- $\frac{1}{2}$ particles. Each of the fermions in Figure 10 has an anti-particle, although it is an open question whether the neutrino is its own anti-particle. The integer-spin bosons, excepting the Higgs boson, which provides a mechanism for giving mass to all the other particles, are the force carriers of the standard model. The spin-1 bosons: the gluon, photon, and W and Z boson, describe three of the four forces known to physics. The gluon mediates the strong force, which governs interactions between quarks, binding them in hadrons (three quark states which make up e.g. protons and neutrons) and mesons (two-quark states such as pions). The photon mediates electromagnetism, governing interactions between particles with electric charge. The W⁺, W⁻, and Z bosons mediate the weak force, which includes phenomena such as beta-decay and neutrino-electron scattering.

It was once proposed that the Z boson could mediate the interaction between DM and SM, because a DM particle that interacts via the weak force fits the WIMP paradigm discussed below. However, direct detection experiments have long excluded such scattering cross sections, of 10^{-39} cm^2 . Naively, it is possible for neutrinos, which interact weakly

and have mass, to be [CDM](#). However, neutrinos were relativistic during structure formation so could not perform the role of necessary of [CDM](#). Estimates of the density of today’s relic neutrinos show that they $\Omega_v \approx (1.2 - 2.2) \times 10^{-3} \ll \Omega_{cdm}$ [28], [29]. The standard model, as it is known today, contains no particles that could be [CDM](#).

2.4 DARK MATTER CANDIDATES MOTIVATED BY PARTICLE PHYSICS

Cosmology, while providing very precise measurements of the dark matter content of the universe, essentially requires only three things of dark matter candidates: (1) the candidate, *en masse*, must account for the observed Ω_{cdm} , (2) at least 95% of it is non-relativistic or “cold” [**something**], (3) it is not strongly self-interacting (“collisionless”) or strongly interacting with baryons. Requirement (1) is fairly loose, as it is possible for multiple different dark matter particles to comprise together Ω_{cdm} , but note that implies the dark matter candidate(s) must be stable on the timescale of the universe. This section briefly summarizes two very different dark matter candidates, which have additional motivation due to open questions from the standard model.

2.4.1 WIMPS AND THE HIERARCHY PROBLEM

Any system that describes particle interactions today at “low energy”, should also scale to describe particle interactions at different times (and therefore energies) in the history of our universe, namely immediately after the Big Bang in a time known as the Planck epoch. During the Planck epoch, energies were at the Planck scale of 10^{19} GeV, and gravitational interactions become as large as the other forces. Any sound quantum theory should be able to account for gravitational interactions at this energy scale. However, the highest energies described by the [SM](#) is the known as the electroweak scale, when electromagnetism and the weak force unify. The breaking of the electroweak symmetry is done by the Higgs mechanism, which provides mass. There is a compelling argument that the strong and electroweak forces unify at energies referred to as the Grand Unified Theory ([GUT](#)) scale, and that this theory then unifies with gravity at the Planck scale (sometimes called “Theory of Everything”) [30]. The 16 orders of magnitude between the Planck scale and the electroweak scale is known as the Hierarchy Problem; there must be new physics between the electroweak scale and the Planck scale, i.e new particles with $m > m_{Higgs}$ and new symmetries, to properly describe particle interactions during the history of our universe.

In order to solve the Hierarchy Problem, a framework known as Supersymmetry (**SUSY**) was developed. In **SUSY** each **SM** particle has a “superpartner.” In general, the superpartners have a spectrum of masses higher than **SM** particles and a symmetry called *R*-parity partitions and limits interactions between **SM** and **SUSY**. The lightest of the **SUSY** particles, called the Lightest Super Partner (**LSP**), can be stable. If the **LSP** neutrally charged it is a dark matter candidate known as a **WIMP**.

The **WIMP** paradigm has its roots in the mathematical coincidence called the **WIMP** Miracle. If one assumes a weak-scale coupling and mass for dark matter, it naturally produces the entire Ω_{cdm} observed today via thermal freezeout. When universe was small and dense with particles, a **WIMP**, χ , would meet its antiparticle $\bar{\chi}$ and annihilate into lighter particles: $\chi\bar{\chi} \rightarrow l\bar{l}$. The reverse reaction to produce the heavier **WIMP** ($l\bar{l} \rightarrow \chi\bar{\chi}$) proceeds as long as the energies of the particle is sufficiently high, i.e. $T > m_\chi$. When this condition is met, the number density n of **WIMPs** is at its thermal equilibrium value n_{eq} . As the universe expands, the reaction falls out of thermal equilibrium. Both directions of the reaction ($\chi\bar{\chi} \rightleftharpoons l\bar{l}$) are affected: the reverse reaction cannot produce more χ due to cooling, and the forward reaction stalls because annihilation rate Γ_A relies on a sufficiently high number density n , such that the probability of χ to meet $\bar{\chi}$ is large. The number density of **WIMPs** become frozen into a relic density that we can observe today when the Hubble expansion rate overcame the annihilation rate:

$$\begin{aligned} H(t) &> \Gamma_A \\ &> n_\chi \langle \sigma_A v \rangle \end{aligned} \tag{9}$$

where $\langle \sigma_A v \rangle$ is the thermally averaged annihilation cross section. The time when $H(t) = \Gamma_A$ is referred to as freezeout. Following [31], the time evolution of the number density is described by the Boltzmann equation (see Figure 11 (left) for number density evolution before and after freezeout):

$$\frac{dn}{dt} = -3Hn - \langle \sigma_A v \rangle (n^2 - n_{eq}^2) \tag{10}$$

This equation must be solved numerically (a more complete analysis can be found in e.g. [32]), but making a few assumptions, [31] finds:

$$\begin{aligned} \Omega_\chi &\sim \frac{m_\chi T_0^3}{\rho_c} \frac{n_f}{T_f} \\ &\propto [\text{constants}] \langle \sigma_A v \rangle^{-1} \end{aligned} \tag{11}$$

Where ρ_c is the critical density, f subscripts refer to freezeout and 0 subscripts refer to today's values. Ω_χ then depends only on the particular annihilation cross section, which is set by the mass scale m_χ :

$$\sigma_A v = k \frac{g_{weak}^4}{16\pi^2 m_\chi^2} (1 \text{ or } v^2) \quad (12)$$

Where v^2 is present or absent for S- or P-wave annihilation and $k \sim \frac{1}{2} - 2$ parameterizes the deviation of g from $g_{weak} \approx 0.065$. If the mass of the dark matter particle is in the range $m_\chi \sim 100 \text{ GeV}-1 \text{ TeV}$, then Ω_χ accounts for 100% of today's observed Ω_{cdm} . This is the **WIMP** miracle: weak-scale particles can account for *all* the dark matter content. Even the **WIMP** mass m_χ deviates from this perfect situation, the particle can still make up a substantial percentage of dark matter (see Figure 11 (right)),

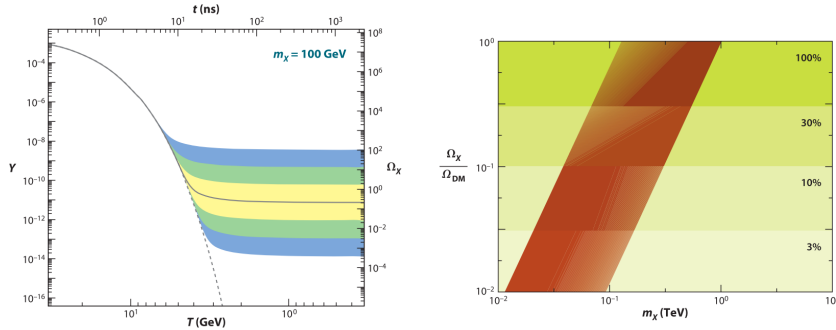


Figure 11: (left) The co-moving number density Y (left y-axis) resulting in the thermal relic density Ω_χ (right y-axis) for a dark matter particle of mass $m_\chi = 100 \text{ GeV}$. The solid black line is the annihilation cross section which yields the correct relic density and bands indicate cross sections that differ by successive factors of 10 from the “correct” annihilation cross section. (right) A band of natural values for a thermal relic χ that composes different percentages of the observed dark matter content. The width of the band is set by the deviation of g from g_{weak} in Equation 12. Figures from [31]

A particle with the exact mass and weak-scale coupling, i.e scattering mediation via the Z-boson, has been ruled out by direct detection experiments, but various **SUSY** parameter regions remain. The **LSP** can be a **WIMP**, and thereby it could solve two mysteries of physics: the hierarchy problem, and dark matter.

2.4.2 AXIONS AND THE STRONG CP PROBLEM

The [SM](#) includes a term in the quark sector that should contribute to CP-violating, flavor-conserving, observables that scale with a mixing angle θ_3 :

$$\mathcal{L} = \theta_3 \frac{g_3^2}{32\pi^2} G_a^{\mu\nu} \tilde{G}_{a\mu\nu} \quad (13)$$

where g_3 is the gluon coupling constant, $G_a^{\mu\nu}$ is the gluon field strength, and θ_3 is a dimensionless constant.

This term should produce, for example, an electric dipole moment of the neutron, d_e . For natural values of $\theta_3 \sim 1$, one would expect $d_e \sim 10^{-16}$ e cm. However, such a dipole moment has never been observed and current experimental limits constrain $d_e < 2.9 \times 10^{-26}$ e cm [31]. To account for this, θ_3 must be ‘fine tuned’ to $\theta_3 \rightarrow \theta_3 10^{-10}$. This is known as the Strong-CP Problem: we expect CP-violating observables from the [SM](#), but instead we find that CP is strongly conserved.

In 1977 Peccei and Quinn proposed a mechanism that solves in the strong CP problem: a new hidden and spontaneously broken global symmetry allows θ_3 to be a dynamical value which goes to zero when the symmetry is broken. A spontaneously broken global symmetry generates a Goldstone boson, so there is a new particle with non-zero mass called the axion (or QCD axion). Although they are predicted to be light ($\sim \mu\text{eV}$ to meV), axion production is possible in the early Universe in such a way that they can be [CDM](#). Depending on whether the Peccei-Quinn symmetry is broken before or after cosmological inflation, different constraints apply. In either case it is possible for an axion with the appropriate mass to make up all of the Ω_{cdm} observed today [33].

2.5 THE DARK SECTOR AND LIGHTLY IONIZING PARTICLES

Chapter 5 of this thesis details a search for [LIPs](#), in this section the theoretical underpinning of such a particle is discussed.

2.5.1 DARK SECTOR

Our universe is dominated by non-baryonic dark matter. A simple way of explaining dark matter without modifying the existing [SM](#) is to require the existence of a dark sector (also called hidden sector), which interacts with the visible sector primarily through gravity [34]. In general, there

may me multiple dark sectors, each with structure rich enough to rival that of the [SM](#). The dark sector and and visible sector may have different thermal histories, but the size of the dark sector (counted in degrees of freedom) is still constrained by the cosmological history we observe in the visible sector. If the hidden sector and visible sector have equal temperatures at the time of Big Bang Nucleosynthesis ([BBN](#))², an exact copy of the [SM](#) is excluded. If the hidden sector and visible sector do not have the same temperature at [BBN](#), either because they are not in thermal contact or they cool independently after inflation, hundreds of degrees of freedom, equivalent to several copies of the [SM](#) are allowed [31].

Dark sectors arise in many extensions to the [SM](#) to provide viable dark matter candidates, such as (pseudo-)scalars that appear naturally when symmetries are broken at high energy scales. If that sounds familiar, it is because an example of such a dark matter candidate, the QCD axion, was discussed above. Aside from gravity, symmetry requirements restrict the interactions the dark sector particles may have with the [SM](#) to a few interactions. These interactions provide what is known as a “portal” to the [SM](#). In general, a dark sector may be completely hidden with no interactions other than gravity with the [SM](#), but some portals are well-motivated by theoretical concerns [35] [31]. In some cases a portal is even required in order to explain galactic structure formation [34]. Four portals that are discussed often with respect to dark sectors are shown in Table 2 [35].

Table 2: Possible dark sector portals, related dark matter candidates, and operator that connects the dark sector to the [SM](#)

Portal Name	Dark Matter Candidates	Operator(s)
Vector	Massive Dark Photons or LIPs	$\frac{\theta}{2} F^{\mu\nu} F'^{\mu\nu}$
Axion	Pseudoscalars	$\frac{a}{f_a} F_{\mu\nu} \tilde{F}^{\mu\nu}, \frac{a}{f_a} G_{i\mu\nu} \tilde{G}_i^{\mu\nu}, \frac{\partial_{\mu} a}{f_a} \bar{\psi} \gamma^{\mu} \gamma^5 \psi$
Higgs	Dark Scalars	$(\mu S + \lambda S^2) H^\dagger H$
Neutrino	Sterile Neutrinos	$y_N LHN$

Higgs portal and neutrino portal searches are best suited to high-energy collider searches and neutrino facilities, respectively. Axion and vector portal searches can also be accomplished with these technologies, but direct detection offers low cost alternatives that are also model-independent.

² [BBN](#) is the time when the the universe has cooled enough to allow the nuclei of the light elements to form ($t_{BBN} \sim 1\text{-}1000\text{s}$). For more in-depth discussion of [BBN](#) and what constrains it places see e.g. [26], [27]

The axion described in Section 2.4.2 is referred to as the QCD axion, it has a specific combination of axion mass and axion-SM coupling. More general axion models, called **ALP!** (**ALP!**s), are less constrained and can make up some percentage of DM [35]. The vector portal is characterized by a dark photon (“paraphoton” in older texts) A' that kinetically mixes with the SM photon A . The mixing strength is parametrized by a factor θ . Dark photon dark sectors are broken up into two cases: $m_{A'} = 0$, and $m_{A'} > 0$. For the massive dark photon case ($m_{A'} > 0$), the dark photon itself can be dark matter. In the simplest case for the vector portal, the dark sector only consists of a massive dark photon and no other particles. Models exist for $m_{A'} \sim \text{MeV-GeV}$ range as well as the sub-eV range [35].

In case where the dark photon is massless ($m_{A'} = 0$), other dark sector particles χ can be stable and massive. This case is what yields LIPs, discussed in the next section.

2.5.2 LIGHTLY IONIZING PARTICLES

Lightly ionizing particles, also known as milli- or fractionally-charged particles, stem from massless dark photon models. The following [36], [37], the kinetic Lagrangian includes the terms:

$$\mathcal{L} \supset -\frac{1}{4g^2}F_{\mu\nu}F^{\mu\nu} - \frac{1}{4g'^2}F'_{\mu\nu}F'^{\mu\nu} + \frac{\theta}{2gg'}F_{\mu\nu}F'^{\mu\nu} \quad (14)$$

Where $F_{\mu\nu} = \partial_\mu A_\nu - \partial_\nu A_\mu$ is the usual electromagnetic field tensor, and $F'_{\mu\nu}$ is similarly the field tensor for the dark photon. The last term is called the kinetic mixing term, as it mixes the gauge kinetic terms for each sector.

Let h be a hidden sector fermion field that has a bare coupling to the hidden photon A' , such that

$$\mathcal{L} \supset \bar{h}A'h \quad (15)$$

The kinetic mixing term in Equation 14 can be diagonalized by the shift:

$$A'_{\mu u} \longrightarrow \tilde{A}'_{\mu u} + \theta A_\mu \quad (16)$$

With the shift, the hidden sector fermion h now couples to the photon:

$$\mathcal{L} \supset \bar{h}A'h \longrightarrow \bar{h}\tilde{A}' + \theta\bar{h}Ah \quad (17)$$

The last term in the equation above corresponds to an effective coupling q of the hidden sector particle h with the visible photon A :

$$q = \theta g' \equiv e \quad (18)$$

In general, g' can be large, but θ is constrained to be small (otherwise the sector would not be hidden). An example diagram of h interacting with electrons is shown in Figure 12. The electrons only “see” h through the A' coupling with A , and thus h appears with a small, non-integer charge with respect to the visible sector. The strength of the diagram goes as the three couplings:

$$|M| \sim \theta g' g = \theta g' e \equiv \epsilon e \quad (19)$$

where we substituted the known low-energy **QED!** (**QED!**) gauge coupling e for g . The particle h is known as a **LIP**, and can be treated as having ϵe charge in encounters with **SM** electrons.

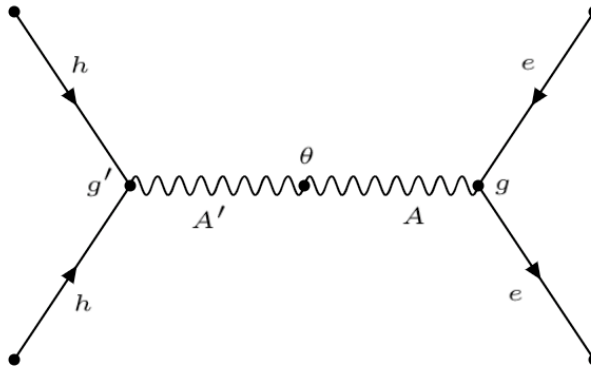


Figure 12: A Feynman diagram of a dark sector particle h interacting with atomic electrons. g' is the gauge coupling to A' in the dark sector, θ the kinetic mixing angle between A' and A , and g is the usual electromagnetic gauge coupling, $g = e$.

There are many constraints on **LIPs** from various sources summarized in Figure 13.

Unlike many of the constraints in Figure 13, a search for fractionally charged cosmic rays is model independent. That is, it does not depend on the particular production mechanism of the **LIP**, nor on its mass. A tacit assumption is made that the cosmic ray is high energy, and indeed such high energy **LIPs** may be produced in the present era in violent astrophysical processes or between interaction of ordinary cosmic rays in the

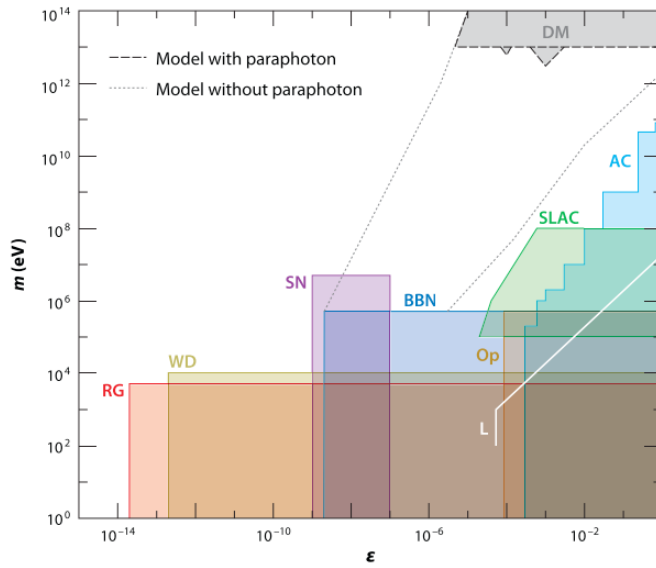


Figure 13: Regions of mass-charge space ruled out for LIPs from several different sources. The dashed line limits apply in the case of a dark sector photon (our case of interest), and the dotted line is the limit without dark photons. Abbreviations: AC, accelerator experiments; Op, search for the invisible decay of ortho-positronium; SLAC, the SLAC millicharged particle search (51); L, the Lamb shift; BBN, big bang nucleosynthesis; RG, plasmon decay in red giants; WD, plasmon decay in white dwarfs; SN, Supernova 1987A. Figure from [38].

atmosphere [38]. The analysis in Chapter 5 concerns the search for LIP cosmic rays. The search sensitivity for LIP cosmic ray searches is given in terms of flux, Φ , with units $\text{cm}^{-2} \text{sr}^{-1} \text{s}^{-1}$ as a function of the “charge fraction” f , where f is defined by $\epsilon = e/f$. See Figure 14 for recent LIP flux limits.

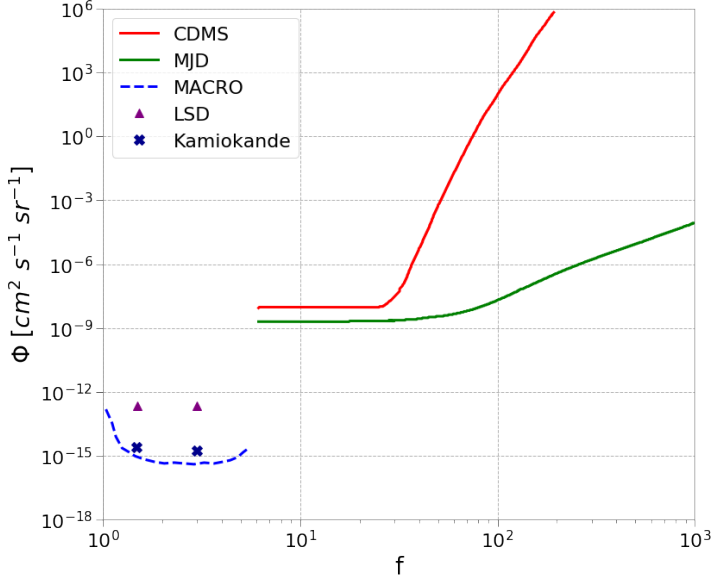


Figure 14: Recent limits on the flux of LIPs with charge e/f where f is the x-axis.

2.5.3 WIMPLESS MIRACLE AND THE NEW PHYSICS FLAVOR PROBLEM

As with any dark matter candidate, it is desirable for hidden dark matter to have the correct relic density. In Section 2.4.1, we discussed the WIMP miracle: how a particle with a weak scale mass and coupling undergoes thermal freezeout to naturally produce the correct relic abundance. There is a similar situation for the hidden sector dubbed the “WIMPless miracle”; which is much more general. Recall that for a stable thermal relic particle χ , the relic density Ω_χ goes as:

$$\Omega_\chi \sim \langle \sigma_A v \rangle^{-1} \sim \frac{m_\chi^2}{g_\chi^4} \quad (20)$$

The WIMP miracle says that for $m_\chi \sim m_{\text{weak}}$ and $g_\chi \sim g_{\text{weak}}$, $\Omega_\chi \approx \Omega_{cdm}$. For a particle that interacts via a known SM force, the weak force is the only reasonable choice, so $g_\chi \sim g_{\text{weak}}$. Hidden sector dark matter, however, has its own matter content and gauge forces, so many combinations of (m_χ, g_χ) are possible. This generalizes the WIMP miracle to

the **WIMPless** miracle: hidden sector dark matter can produce the correct relic density, but need not have weak scale mass nor interact via the weak force (Figure 15).

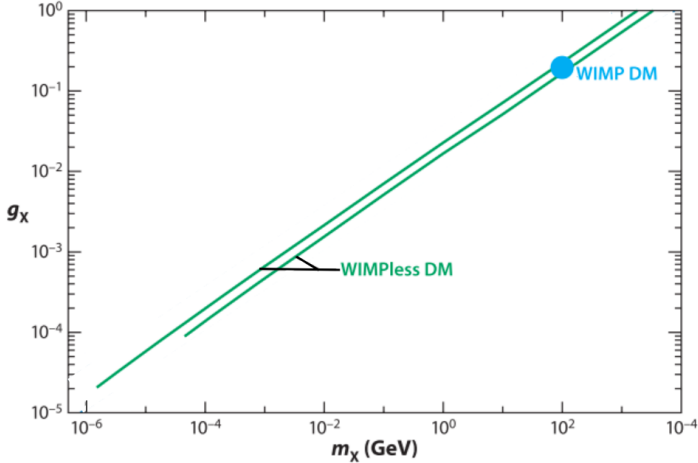


Figure 15: Contours in the (m_χ, g_χ) for two different temperature conditions for the hidden sector. The upper line is for a hidden sector that achieves 80% of the visible sector temperature after reheating, the lower line is for 30%. The hidden sector is a 1-generation flavor-free version of the minimal supersymmetric standard model. Figure adapted from [31].

Recall also from Section 2.4.1, that in addition to it producing the correct relic abundance, the **WIMP** is a favored dark matter candidate because it is related to **SUSY**, which is introduced to solve the hierarchy problem of the **SM**. In attempting to solve the gauge hierarchy problem, **SUSY** gives rise to another problem called the “new physics flavor problem” [31]. **SUSY** particles may violate baryon number, lepton number, flavor, or CP. At the same time, we observe these symmetries to be extremely well preserved in the **SM**. The new physics flavor problem, in a nutshell, is that not all **SUSY** models are capable of elegantly conserving these symmetries. Creating models that solve the new physics flavor problem is a “prime driver in the field of supersymmetric model building” [31]. A particularly elegant subset of **SUSY** models that do solve the new physics flavor problems are known as Gauge-Mediated Supersymmetry Breaking (**GMSB**). In these models, a hidden sector mediates **SUSY** breaking³. In **WIMPless** scenarios, one asks why the hidden sector dark matter should be stable. For **GMSB**

³ **SUSY** is a symmetry that must be broken, otherwise a host of problems would be present. For example, without a broken **SUSY**, the electron and selectron would have the same mass. Furthermore, selectrons are bosons. If we lived in a world where both electrons and selectrons were common, we would not have atomic structure because orbital fermionic electrons are a higher energy state than infinite ground state selectrons.

models, which solve the new physics flavor problem, an elegant way to stabilize the hidden sector dark matter is through the hidden U(1) charge conservation, which necessitates a massless gauge boson in the hidden sector. This is precisely the situation we have with LIPs. To quote [31]: “In summary, hidden sector dark matter models may in fact be motivated by leading problems in particle physics, and may even have naturally the correct relic density, through a generalization of the WIMP miracle to the WIMPless miracle.”

2.5.4 CHARGE QUANTIZATION

It is known experimentally that all charged particles in the SM have charge $\pm\frac{1}{3}e$, $\pm\frac{2}{3}e$, or $\pm e$. However, there is no theoretical motivation behind this quantization of electric charge. Holdom suggested a new, U(1) with a “paraphoton” gauge boson could produce quantized charge in the SM and transfer fractional shifts to fermions that interact with the paraphoton [36], which is the LIP paradigm. Others, [39], [40], [41], [42], and [43], have proposed various extensions to the SM that would produce charge quantization. Some of these theories yield fractionally charged particles, and all of them require new physics beyond the SM. It is useful to note that even outside of the hidden sector, there are theoretical motivations for fractionally charged particles.

2.6 EXPERIMENTAL STRATEGIES FOR DETECTING DARK MATTER

Experiments designed to detect dark matter, be it WIMP, axion, dark sector, or other candidates, fall into three main categories: production, indirect detection, direct detection (see Figure 16). Detection schemes and examples are discussed in the following subsections. All three methods are in use to provide a diverse, multipronged DM detection program.

2.6.1 PRODUCTION

Colliders like the LHC! (LHC!) are capable of accelerating SM particles to high energies. The SM particles, typically protons, antiprotons, electrons, and/or positrons, can be collided with each other or with a fixed target. In general, dark matter produced in these collisions appears as “missing energy” when the event is reconstructed. If a multitude of events is missing the same amount energy E , that is a classic indication that there is a

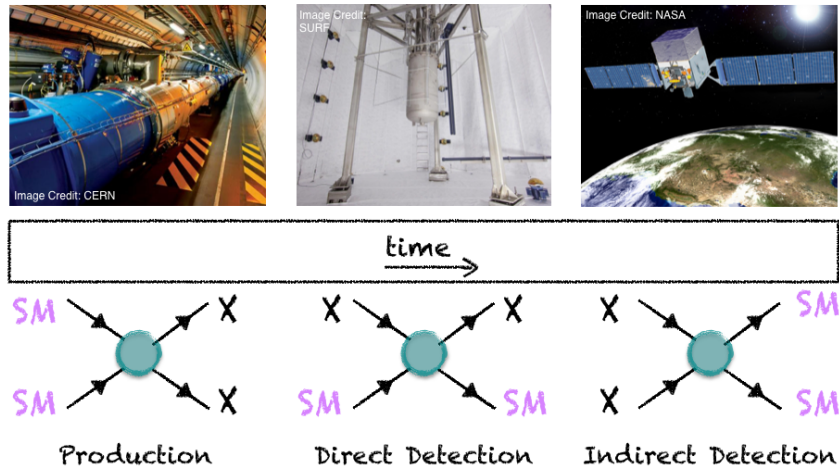


Figure 16: Summary of **DM** detection schemes with illustrative Feynman diagrams. In all cases, the arrow to time is from left to right. (left) **SM** particles can be collided at high energy facilities, which may produce **DM** particles χ . (center) **DM** particles χ may scatter with **SM** particles, leaving behind a characteristic signal. (right) **DM** particles in the galaxy may annihilate and produce **SM** particles, which produce signal in excess of expectations from standard astrophysical processes.

new particle with mass $m = E/c^2$. A recent overview of collider searches for several different dark matter candidates can be found in [44].

2.6.1 LIP PRODUCTION

It is noted in [38] that “high-energy electron-positron colliders provide the most definitive search method among accelerator and collider searches for fractionally charge particles [in the range $\pm \frac{1}{3}e - \pm \frac{4}{3}e$].” This is due to the production cross section being large and known to high accuracy. Another successful collider method to search for fractionally charged particles with charge $\ll 1$ is a “beam dump”. In beam dump experiments, the collider accelerates e.g. an electron into a fixed target, producing secondary particles. A large mass of shielding is between the target and the detector. Only secondary particles with a small charge can make it through the shielding to reach the detector. The limit in Figure 13 titled SLAC is from a beam dump type experiment; see [45] for details about the SLAC millicharged particle search.

2.6.2 INDIRECT DETECTION

The signal of dark matter annihilation can appear in both ground-based and satellite detectors. Dark matter may decay or annihilate into **SM** par-

ticles, which can be detected by conventional detectors. Positive identification of an indirect dark matter signal is difficult due to large potential backgrounds from astrophysical sources, which are not perfectly understood. However, indirect detection can probe questions collider and direct searches cannot, such as whether [DM](#) is perfectly stable and what the annihilation cross sections are.

2.6.2.1 LIP INDIRECT DETECTION

Indirect limits for fractionally charged particles come from stellar evolution and supernovae. See limits titled WD, RG, and SN from Figure 13. Essentially, new low-mass particles can be produced in the hot and dense medium of stars, and eventually escape, carrying away energy [46]. The additional energy-loss channel modifies stellar evolution, and observations of brightness, etc. can set a limit on the [LIP](#) mass and interaction strength. For Supernova 1987A, the number of neutrinos detected at Earth roughly agrees with theoretical expectations. If fractionally charged particles contribute to cooling, the neutrino flux would decrease, and the SN limit in Figure 13 is from such an analysis.

2.6.3 DIRECT DETECTION

In direct detection, experimentalists seek to observe [DM](#) interactions in a detector composed of [SM](#) materials. Detectors are designed with a [DM](#) candidate in mind, and aspects of the detector are optimized at the design stage to search for one type of [DM](#). Because direct detection searches are built with a particular [DM](#) candidate in mind, backgrounds can be controlled and minimized much more than in indirect or production searches. Of course, a given detector can search for [DM](#) candidate even if it was not initially designed to do so, and in this case, the search still benefits from the detailed understanding of backgrounds in the detector. Most current direct detection programs fall into one of two categories: [WIMP](#) detector or axion detector. In the case of [WIMP](#) detectors, the detector target material is some homogenous material like solid Ge or liquid Xe, and experimentalists seek to detect energy deposition consistent with that of a [WIMP](#) recoiling in the target. This type of detector must be composed of radiopure materials and located deep underground to be capable to detecting rare [WIMP](#) interactions. In the case of axions, the detector is resonator cavity with a strong magnetic field, which couples with the axion field. Axion detectors need not be underground because they take advantage of a resonance amplification of their signal that would occur at a specific axion mass and coupling.

2.6.3.1 LIP DIRECT DETECTION

Direct detection searches for fractionally charged particles include schemes like the Millikan drop experiment, which modern methods have improved upon (see [38] for more detail). Table-top style experiments searching for the decay of ortho-positronium, or changes in the Lamb shift, would indicate additional couplings to a hidden sector; these are marked Op and L in Figure 13, respectively. Large water or liquid scintillator detectors such as Kamiokande and Macro performed searches for fractionally charged cosmic rays from e down to $e/6$ (see Figure 14). More recent searches from **CDMS!** (**CDMS!**) and **MJD!** (**MJD!**) extend the charge fraction range of these searches down to $\sim e/1000$. These last two searches are both from cryogenic Ge detectors designed with other goals in mind – **CDMS!** is a canonical **WIMP** detector and **MJD!** is a neutrinoless double beta decay experiment. A similar search for cosmic ray **LIPs** is carried out in Chapter 5 with the **LUX** experiment, which is also a canonical **WIMP** detector, but uses **LXe** for its target material. More details about **LXe** as a detector medium are found in Chapter 3. Details about the **LUX** detector can be found in Chapter 4.

3

PARTICLE DETECTION WITH LIQUID XENON

3.1 LIQUID XENON AS A DETECTOR MEDIUM

Liquid xenon detectors are powerful tools for rare event searches. In particular, the dual phase [LXe TPC](#) has been very successful in accessing [WIMP](#) parameter space and currently holds the worlds most sensitive limits on [WIMPs](#). This section describes the properties of [LXe](#) and the basic principles of [TPCs](#) that have allowed this technology to play a large role in the hunt for dark matter.

3.1.1 PROPERTIES OF LIQUID XENON

Liquid xenon has many properties relevant to particle detection, particle identification, and also many properties related to the ease of detector operation:

- The density of [LXe](#) is 2.9 g/cm³ at 170 K, much denser than other possible [TPC](#) target materials, such as liquid argon which has density 1.4 g/cm³ at 87 K. The advantage in this two-fold: (1) the same volume contains more kg of Xe than Ar, so for two detectors of the same volume, one filled with Xe and the other with Ar, both running for one year, the Xe detector has more exposure; (2) xenon's high density effectively stops external radiation, producing an ultra-low-background volume in the center of the detector where rare-event searches can be performed (this region is called the "fiducial volume").
- Xenon gas is easily liquefied with liquid nitrogen (77 K) or commercially available pulse tube refrigerators.
- Xenon has no long-lived radioisotopes that cause troublesome backgrounds. The one exception is the $2\nu\beta\beta$ decay of ^{136}Xe (natural abundance 8.875%) with measured half-life of 2.1×10^{21} years. The long half-life and relatively low abundance together result in a very low count rate, and the isotope can be used to search for neutrino-less double beta decay ($0\nu\beta\beta$).

- Xenon, as a noble element, is easily purified with a heated getter to rid electronegative impurities. Some of these impurities absorb xenon scintillation light, e.g. N₂, and others can attract electrons, interfering with the ionization signal in TPCs, e.g. O₂.
- The comparatively large mass of xenon allows it to be purified of other noble gasses via gas chromatography [47] and cryogenic distillation [48]. As other noble gasses cannot be removed via getter, this feature is extremely useful in removing the troublesome background of ⁸⁵Kr decay. ⁸⁵Kr decays via beta emission to stable ⁸⁵Rb with a half-life of 10.8 years and Q _{β} = 687 keV. The decay proceeds directly to the ⁸⁵Rb ground state with a branching ratio of 99.6%. Since no de-excitation of ⁸⁵Rb follows, this beta decay cannot be rejected as background by coincidence with a gamma, and relies purely on the ability to discriminate between WIMP-like NR and beta- or gamma- produced ER. While ER/NR discrimination is one of the features of LXe TPCs (described in Section 3.3.1.1), leakage of ER events into the NR signal region can occur and the best mitigation is to remove as much of the ⁸⁵Kr as possible. Single-phase LXe detectors, with no ER/NR discrimination, benefit greatly from the ability to remove ⁸⁵Kr.
- Particles interacting in LXe excite atoms and create electron ion-pairs, producing detectable quanta: scintillation photons and ionization electrons, respectively (described in section 3.1.2).
- Xenon produces scintillation light of wavelength $\lambda = 178$ nm (described in Section 3.1.2). Xenon is transparent to this wavelength so it can propagate freely and be directly detected with current PMT technology, and doesn't require the use of e.g wavelength shifter.
- Ionization electrons produced in particle interactions can be drifted and extracted into a gaseous region via applied electric fields, where they undergo proportional scintillation. By this method, a single electron is amplified many-fold into detectable photons. This basic operating principle of dual-phase TPCs makes even a single ionization electron detectable.
- Xenon has high light and charge yields, and therefore a low threshold for producing detectable quanta. A useful quantity is the so-called ‘W-value’ of LXe: $W = 13.7 \pm 0.2$ eV [49]. The W-value, analogous to a work-function, is a measure of the average energy expenditure to produce one quanta (scintillation photon or an ionization electron) from liquid xenon.

- LXe TPCs are easily scalable: creating a large homogenous volume is straightforward. In contrast, solid state detectors, such as cryogenic Ge, are more difficult to scale up directly and require instead the production of multiple small modules ($O(10)$ cm) which each must be instrumented separately.

3.1.2 SCINTILLATION AND IONIZATION SIGNAL GENERATION

A particle can interact with a xenon atom through interaction with an orbiting electron, creating an ER, or though an interaction with the xenon nucleus, where the nucleus is imparted with momentum and recoils, NR. Some energy is lost to atomic motion (heat). The recoiling electron or nucleus loses energy via interaction with neighboring xenon atoms, creating more excited atoms and electron-ion pairs. The excited xenon atoms, Xe^* , combine with other atoms to form an excited dimer, or excitons, Xe_2^* . The excited dimer forms two states: a triplet and a singlet, which de-excite with the emission of a 178 nm photon. The lifetimes of the triplet and singlet are measured to be 24 ns and 3 ns, respectively [50]. Since the scintillation light is produced by the excimer, which has a different electronic structure than atomic xenon, the light is free to propagate through the detector and will not be absorbed by the atomic xenon. The Xe^+ ions of the electron-ion pairs combine with other Xe atoms to form dimers Xe_2^+ , and these dimers can combine with electrons (from the electron-ion pairs) to form excitons, Xe_2^* , which then decay and produce additional 178 nm scintillation photons. This process is called recombination. If no electric field is applied, all electron-ion pairs recombine to produce additional scintillation photons. If an external electric field is present, some electrons can be drifted away from the interaction site to be detected with other methods.

The sensitivity of liquid xenon detectors to low energy recoils depends on their ability to detect the 178 nm scintillation photons with high-efficiency. High Quantum Efficiency (QE) PMTs constructed with ultra-low radioactivity materials are the go-to instrument for this purpose. In addition to high-efficiency photon-detectors, liquid xenon detectors must also have high geometrical light collection efficiency to optimize sensitivity. Single-phase liquid xenon detectors, where no electric field is applied, maximize light-collection by with a spherical geometry, endeavoring to cover 4π steradians surrounding the LXe. The XMASS detector uses spherical geometry to accomplish photocathode coverage of 62%, and two types of Hamamatsu PMTs (R10789-11 and R10789-11MOD) with QE of 28%, and quote a signal collection efficiency of 20% [51], [52]. Dual-phase TPC detectors are lined with PTFE to take advantage of its extremely high (99%) reflectivity for 178 nm light in LXe [53]. The LUX detector uses a cylin-

drical geometry, with all non-light-collecting surfaces lined with PTFE, and Hamamatsu R8778 PMTs (QE of 33%) only on the top and bottom of the detector (low photocathode coverage), to accomplish a light collection efficiency of 90% [54].

If the detector is a TPC the ionization electrons are drifted away from the interaction site to be detected. Single phase TPC employ thin wires to collect the ionization electrons. For example, the EXO-200 experiment is a single-phase liquid xenon TPC that uses crossed-wire planes to collect the ionization electrons and avalanche photodiodes to collect the scintillation photons [55]. LUX is a dual-phase xenon TPC, where ionization electrons produced in the large liquid region are drifted and extracted into gaseous xenon via applied electric fields, where they undergo proportional scintillation. The proportional scintillation light is the same 178 nm wavelength as scintillation in the liquid produced in the liquid, and it is similarly collected via high QE PMTs.

In addition to light-collection efficiency, the sensitivity of TPC xenon detectors also depends on their ability to collect signal from the ionization electrons. There are challenges in delivering High Voltage (HV) to liquid xenon in order to set up the electric field which drifts the ionization electrons (some of these challenges are explained in Chapter 6). Additionally, electronegative impurities such as oxygen (O_2) present in the detector attract and capture ionization electrons as they drift, eating away the ionization signal. These non-noble impurities are removed by constantly circulating the xenon through a heated zirconium getter and returning it to the detection volume. Purification through a getter must be done in gaseous phase, so liquid xenon removed from the detection volume is evaporated, passed through the getter via a circulation system, and re-condensed into the detection volume.

3.2 DUAL-PHASE XENON TIME PROJECTION CHAMBER

A particle interacting in a noble liquid or gas target deposits energy into scintillation and ionization channels (Section 3.1.2). The basic operating principle of TPCs is to drift the ionization electrons away from the interaction site and detect them at a later time than the scintillation signal is detected. A dual phase liquid xenon TPC is a type of TPC with a large liquid target volume and a small region of xenon vapor above the liquid volume, instrumented with light sensors (typically PMTs). A particle interacting in the liquid target produces both scintillation photons and ionization electrons at the interaction site. The scintillation photons are promptly detected by the PMTs, this primary signal is called S1. The ionization elec-

trons are drifted upward to the gas region by an applied electric field, and extracted across the liquid-gas boundary by a higher electric field, where they undergo proportional scintillation and produce a second signal detected by the PMTs, called S2. The field is supplied by a series of electrodes, composed of wire planes, grids, or chemically etched meshes, held at constant voltages. The bottom-most field-producing electrode is called the cathode, at the top of the liquid region is the gate or extraction electrode, followed O(1) cm by the anode. The liquid region is often referred to as the ‘drift region’ and region between the gate and anode is referred to as the ‘extraction region’. The drift region takes up by far more volume than the extraction region. The electrons are extracted from liquid to gas with some efficiency, called the EEE. This efficiency plays an important role in the operation of dual-phase LXe TPCs, and is discussed further in **E-Train CHAPTER**.

The S2 in a dual-phase TPC plays two important roles: (i) internal amplification of the signal, whereby a few electrons are transformed into O(10) times as many photons (ii) (x, y) localization via PMT hit pattern. The time spacing of the S1 and S2 signals can be converted to depth (z) of the interaction, providing full (x, y, z)-reconstruction of the interaction position.

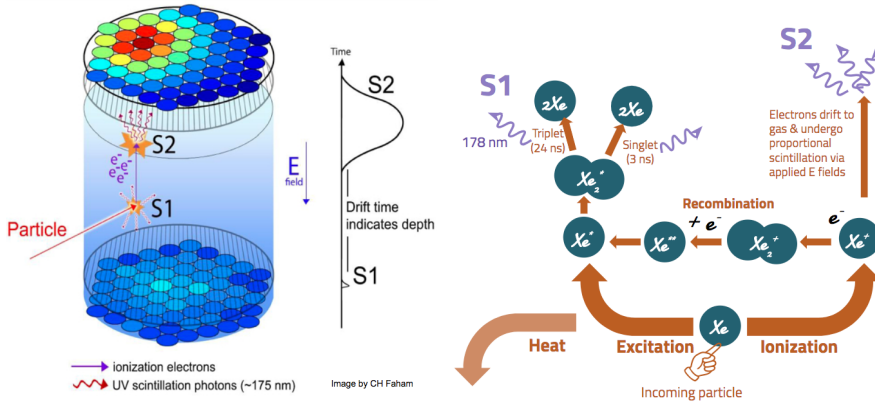


Figure 17: (left) Diagram of a dual-phase xenon time projection chamber. The time difference between S1 and S2 gives the depth (z) of the interaction, and (x, y) is reconstructed from the S2 signal. (right) Diagram summarizing the generation of the scintillation and ionization signal generation in dual-phase xenon time projection chambers.

3.2.1 ENERGY RECONSTRUCTION

Energy reconstruction in dual-phase xenon TPCs comes from the measurable quantities, S1 and S2, but begins with the number of excitons n_{ex} and electron-ions pairs n_i generated at the interaction site.

$$E = fW(n_{ex} + n_i) \quad (21)$$

where E is the deposited energy. W is the average energy needed to produce a single excited or ionized atom, $W = 13.7 \pm 0.2$ eV [50]. The quenching factor, f is 1 for electronic recoils but $f \neq 1$ for nuclear recoils. For now, take the case of electronic recoils and set $f = 1$. This equation can be rewritten:

$$E_{ER} = W\left(1 + \frac{n_{ex}}{n_i}\right)n_i \quad (22)$$

The ratio of excitons to ions is constant for electron recoils $n_{ex}/n_i = 0.2$ [56]. As discussed in Section 3.1.2, each exciton deexcites, emitting a 178 nm photon, some fraction r of the initial electron-ion pairs recombine and form additional excitons. The total number of prompt scintillation photons created by the interaction is then:

$$n_\gamma = \left(r + \frac{n_{ex}}{n_i}\right)n_i \quad (23)$$

And the total number of electrons created by interaction site (electrons escaping recombination) is:

$$n_e = (1 - r)n_i \quad (24)$$

Thus, the effect of recombination is to “trade-out” electrons for photons, but the total number of quanta is conserved (Figure 18 (left)). The amount of recombination depends on applied electric field, LXe density, and particle energy [56]. In the case of the 122 keV electron recoils in Figure 18 (right): at low fields, most of the electron-ion pairs recombine, which results in more scintillation photons. As the applied electric field increases, more electrons are pulled away from the interaction site resulting in fewer scintillation photons and more ionization electrons. These amounts of photons and electrons are referred to as the scintillation and ionization yields. The two quantities, n_γ and n_e relate directly to the observable S1 and S2 signals:

$$\begin{aligned} E_{ER} &= W(n_\gamma + n_e) \\ &= W\left(\frac{S1}{g_1} + \frac{S2}{g_2}\right) \end{aligned} \quad (25)$$

where E_{ER} reminds us that we are taking the case of electronic recoils and set $f = 1$ in Equation 25. $S1$ and $S2$ are in units of detected photons (phd) or photoelectrons (phe), and g_1 and g_2 are detector gains in units of phd / quanta or phe / quanta¹. g_1 is the detection efficiency for the prompt scintillation photons: it is a product of the the average geometrical light collection efficiency and the average PMT QE. Typical values for g_1 are in the range of 0.01-0.02. g_2 is the analogous quantity for $S2$ proportional scintillation light: it is a product of the EEE and the average number of detected photons produced by one extracted electron. Typical values for g_2 are in the range 10-60.

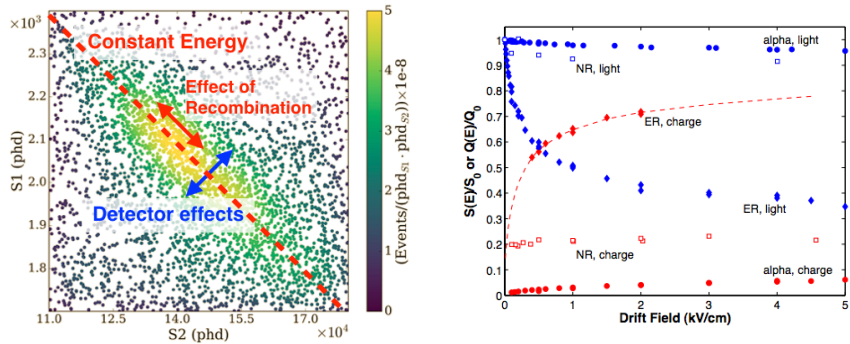


Figure 18: (left) Plot illustrating the effect of recombination and detector effects on a line source (^{127}Xe), courtesy of E. Pease. (right) Field dependence of scintillation and ionization yield in LXe for 122 keV electron recoils (ER), 56.5 keV nuclear recoils (NR) and 5.5 MeV alphas, relative to the yield with no drift field from [59]

To properly reconstruct the energy of nuclear recoils, we must revisit the quenching factor factor f . Equation 25 then becomes:

$$\begin{aligned} E_{NR} &= fW(n_\gamma + n_e) \\ &= fW\left(\frac{S1}{g_1} + \frac{S2}{g_2}\right) \end{aligned} \tag{26}$$

This equation can be rewritten:

$$E_{NR} = fE_{ER} = \frac{E_{ER}}{\mathcal{L}} \tag{27}$$

¹ An distinction should be made between the traditional units of phe and the units of phd which are used in many LUX publications. The Hamamatsu R8778 PMTs used in LUX emit two photoelectrons for a single VUV photon 20% of the time [57], but the PMT gain calibration photons (from blue LEDs) do not. LUX performed additional calibration with VUV photons to account for the difference, and report detected photons instead of photoelectrons [58]

where \mathcal{L} is Lindhard's factor. Lindhard's factor accounts for the fraction of energy lost to atomic motion (heat) in nuclear recoils [60]. An incoming particle interacts with a “patient zero” Xe atom, resulting in a nuclear recoil. The patient zero Xe atom interacts with surrounding atoms in a cascade to produce S1 and S2; it is the energy partitioning in this cascade that results in different energy scales for **ER** and **NR**. Lindhard shows that the energy partitioned in nuclear interactions and electron interactions from a recoiling xenon nucleus is:

$$\mathcal{L} = \frac{kg(\epsilon)}{1 + kg(\epsilon)} \quad (28)$$

where $k = 0.133Z^{2/3}A^{-1/2}$ is a proportionality constant that relates electronic stopping power and the velocity of the recoiling xenon atom, and $\epsilon = 11.5(E_{NR}/\text{keV})Z^{-7/3}$. Lindhard's calculation yields $k = 0.166$, which is the commonly accepted value. Measurements of nuclear recoils in **LXe** are used to fit for k . Several experiments were compared by Sorensen and Dahl to determine that nuclear recoil energy is well described by $0.110 < k < 0.166$ [61]. Results from **LUX** yielded $k = 0.1735 \pm 0.0060$ [62].

If it is not known *a priori* whether an interaction is a nuclear recoil or electron recoil, the ‘electron equivalent’ energy is given in units keV_{ee} . If it is known that the recoil is a nuclear recoil, Lindhard’s factor is applied and the units can be given in keV_{nr} . Lindhard’s factor allows us to combine nuclear recoils and electronic recoils on one energy scale by labelling contours of constant reconstructed energy with both keV_{ee} and keV_{nr} (example in Figure 19).

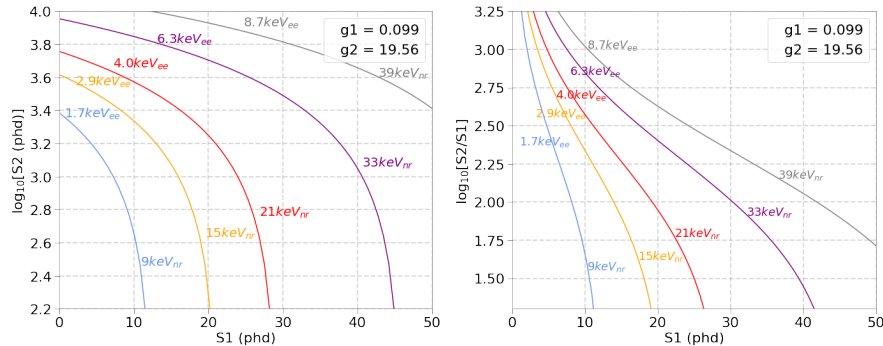


Figure 19: Plots showing combined energy contours in two common sets of axis units, for an example set of g_1 and g_2 .

3.3 DUAL-PHASE XENON TPCS FOR DARK MATTER DETECTION

Dual phase Xe TPCs have been at the forefront of the hunt for dark matter in the last several decades. As described above, the xenon medium and detector technology make excellent low-background, rare-event searches with high signal yields. Dual phase Xe TPCs also provide a few enhancements to WIMP dark matter searches, but other dark matter or rare event searches are also possible with the same detector.

3.3.1 WIMP SEARCHES WITH LXE TPCS

Dual-phase LXe TPCs are optimized for WIMP searches. They have been very successful in reaching large areas of WIMP parameter space.

3.3.1.1 ER, NR DISCRIMINATION

One of the most powerful features of LXe TPCs, which has made the technology especially useful in the hunt for WIMP dark matter, is the ability to discriminate between electron recoils and nuclear recoils. WIMP interactions are expected to be nuclear recoils, but most natural radioactivity (β, γ) are electron recoils. The amount of recombination for equal energy ER and NR is different, so for events with the same reconstructed energy $E(\text{keV}_{ee})$, the ratio of S2/S1 is characteristically different. A useful discrimination space is $\log_{10}(\text{S2}/\text{S1})$ vs S1, as the distributions of $\log_{10}(\text{S2}/\text{S1})$ for ER and NR events are Gaussian. Different calibration sources are used to develop a population of events known to be ER and a population of events known to be NR, these calibration sources reveal what is known as the ER and NR bands (Figure 20).

In the course of a WIMP search, the experimentalists are tasked with keeping a stable detector operating for months or years. In this time, the detector will see events of natural radioactivity and perhaps WIMPs. The natural radioactivity appears in the ER band (location of bands is known from calibration), and nuclear recoil events appear in the NR band. Due to band overlap, only events appearing below the NR mean are considered WIMP candidates. This restriction cuts signal acceptance to 50%, but allows dual-phase TPCs to reject background electronic recoils at $\gtrsim 99\%$. The background acceptance rate is known as ER leakage. It is the fraction of events appearing below the NR mean from the ER calibration source. For a background rejection rate of 99.99%, the ER leakage is 0.01%, this number determines the sensitivity of the detector.

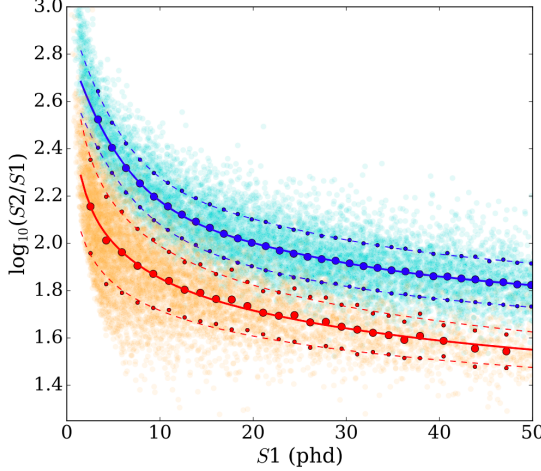


Figure 20: Plot showing ER and NR bands from LUX. Solid lines are the ER and NR Gaussian means μ , dotted lines are $\mu \pm 1\sigma$. Figure from [56]

3.3.1.2 WIMP RATES AND CROSS SECTION

The choice of direct detection for **WIMP** searches was touched on in Section ???. Here, we go through the specifics of **WIMP** rates and their cross section in **LXe**, showing that the **LXe TPC** technology gets an enhancement that makes it especially suited for **WIMP** searches.

WIMPs scattering in the **TPC** produce measurable nuclear recoils. The shape of this nuclear recoil spectrum determines eventually the number of **WIMP** events observed, and it depends on both **WIMP** properties and detector properties. The energy imparted to nucleus depends on **WIMP** mass M_χ and velocity distribution, as well as the mass of the target nucleus M_T and a nuclear form factor F that governs how effectively energy is transferred to the nucleus. Assuming a uniform, spherical dark matter halo, estimates for the local density of dark matter ρ_χ can be made from astrophysical observations. The velocity distribution $f(v)$ is assumed to be isotropic and Maxwellian, with a cut-off at the escape velocity v_{esc} of the Milky Way. If we account for the velocity of the Earth through the galactic plane v_E , the velocity distribution is shifted: $f(v) = f(v, v_E)$. Following Lewin and Smith [63], we can write the local number density:

$$\begin{aligned} dn &= \frac{n_0}{k} f(v, v_E) d^3v \\ &= \frac{n_0}{k} \exp\left(-\frac{(v + v_E)^2}{v_0^2}\right) d^3v \end{aligned} \tag{29}$$

Where $n_0 = p_\chi/M_\chi$ is the average local number density of dark matter particles, $v_0 \approx 220 \text{ km/s}$ [?] is the mean of the dark matter velocity dis-

tribution, and k is a normalization constant such that $\int_0^{v_{esc}} \equiv n_0$. If the escape velocity is infinite, the normalization integral is easily evaluated:

$$k = \int_0^{2\pi} \int_{-1}^{1i} d(\cos\theta) \int_0^{\infty} f(v, v_E) v^2 dv = (\pi v_0^2)^{3/2} \equiv k_0 \quad (30)$$

v_{esc} is not infinite ($v_{esc} \approx 544 \text{ km/s}$ [64]), and so the normalization integral evaluates to:

$$k = k_0 \left[\operatorname{erf}\left(\frac{v_{esc}}{v_0}\right) - \frac{2}{\pi^{1/2}} \frac{v_{esc}}{v_0} \exp(-v_{esc}^2/v_0^2) \right] \equiv k_1 \quad (31)$$

Although this is a more complicated expression, it should be noted the difference between k_0 and k_1 is less than 0.5%. We now have a full picture of the local number density of dark matter, and we focus on the scattering rate in the detector. If we let σ be the scattering cross-section per nucleus (the details of σ are discussed later), the event rate per unit mass detector with target mass M_T is:

$$dR = \frac{1}{M_T} \sigma v dn \quad (32)$$

The experimentalist is concerned with the observable recoil energy spectrum produced by such a dark matter rate. A **WIMP** of mass M_χ and initial energy $E_\chi = \frac{1}{2} M_\chi v^2$ scattering at angle θ (in the center-of-mass frame) will impart a recoil energy E_R to a target nucleus of M_T

$$E_R = r E_\chi \frac{1 - \cos\theta}{2} \quad (33)$$

Where r is the kinematic factor:

$$r = \frac{4M_\chi M_T}{(M_\chi + M_T)^2} \quad (34)$$

Note that the kinematic factor indicates that recoil energies are greatest for $M_\chi \approx M_T$. SUSY models favor **WIMP** masses in the range 100GeV-1000GeV (Figure 22), which makes xenon ($M_{Xe} \approx 123 \text{ GeV}$) an excellent target. **WIMP** scatters are assumed to be isotropic, so recoil energies are distributed uniformly in the range $0 < E_R < rE_\chi$ (i.e. Equation 33 for $0 < \cos\theta < 1$). We can put this together with Equation 32 to arrive at an differential rate per recoil energy in the detector – i.e. the observable recoil spectrum for **WIMP**-nucleus scattering. Note that equation Equation 32 is in terms of the **WIMP** velocity v and Equation 33 is in terms of

[WIMP](#) energy $E_\chi = \frac{1}{2}M_\chi v^2$, so a change of variables is required. After the variable change, we can write:

$$\frac{dR}{dE_R} = \frac{\rho_\chi}{M_\chi} \frac{\sigma}{k} \left(\frac{M_T + M_\chi}{M_T M_\chi} \right)^2 \int_{v_{min}}^{v_{max}} \frac{1}{v} f(v, v_E) d^3 v \quad (35)$$

Until now, we have left off discussion of the [WIMP](#)-nucleus cross section σ . Equation 35, as it stands is the [WIMP](#) spectrum in the limit of billiard-ball coherent scattering. In reality, nucleus has structure which must be accounted for, which is accomplished with a nuclear form factor $F = F(q)$. In addition, the cross-section is split into spin-independent (σ_{SI}) and spin-dependent (σ_{SD}) components:

$$\sigma = \sigma_{SI} F_{SI}^2(q) + \sigma_{SD} F_{SD}^2(q) \quad (36)$$

The nuclear form factor, $F(q)_{SI,SD}$, decreases the cross section at higher momentum transfer. The two coherent terms σ_{SI} and σ_{SD} are parametrized as follows:

$$\begin{aligned} \sigma_{SI} &= \frac{4\mu^2}{\pi} [(A - Z)f_n + Zf_p]^2 \\ &\approx \frac{4\mu^2 A^2}{\pi} f_n^2 \end{aligned} \quad (37)$$

Where μ is the usual reduced mass, and the second line takes into account that for [SUSY WIMP](#) models, the couplings to neutrons and protons are approximately equal ($f_n \approx f_p$).

$$\sigma_{SD} = \frac{32G_F\mu^2}{\pi} \frac{J+1}{J} [\langle s_n \rangle a_n + \langle s_p \rangle a_p]^2 \quad (38)$$

Where G_F is the Fermi constant, J is the total nuclear spin of the target, and $\langle s_{n,p} \rangle$ and $a_{n,p}$ represent values for neutron and proton spins and couplings, respectively. It should be noted that σ_{SI} scales as A^2 , which indicates a cross-section enhancement for larger targets. σ_{SD} lacks the A^2 scaling, and is smaller σ_{SI} . This indicates that recoil-rates are dominated by spin-dependent interactions. The two cases are treated separately, with collaborations releasing both spin-independent and spin-dependent [WIMP](#) limits. in liquid xenon detectors, the odd-numbered nuclei ^{129}Xe and ^{131}Xe contribute to the spin-dependent rate. The enhancements for the [WIMP](#) recoil rate in Xe are illustrated in Figure 21

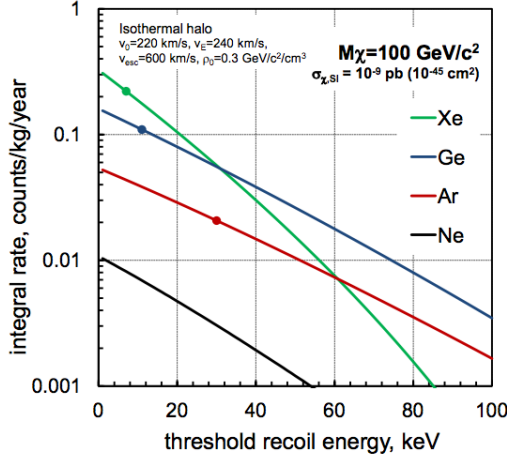


Figure 21: Plot showing spin-independent WIMP rates in common detector target materials, dots indicate typical thresholds for the targets. Xenon gains in favored SUSY parameter space ($M_\chi \gtrsim 100$ GeV) due to a kinematic enhancement ($M_\chi \sim M_{Xe}$) and a cross-section enhancement ($\sigma_{SI} \propto A^2$). Figure from [65]

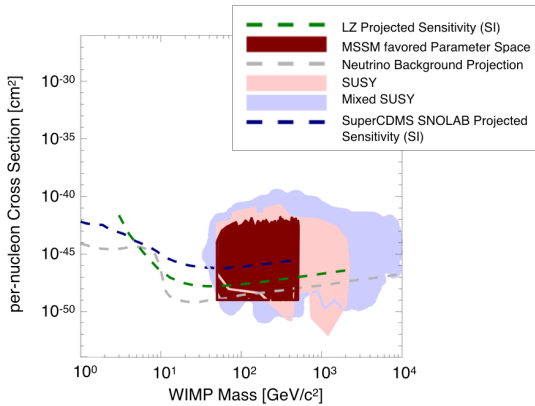


Figure 22: Projected limits of next-generation dark matter detectors and areas where SUSY models predict the presence of WIMPs. Although Xe (LZ, green dashed) performs better for WIMP parameter space, Ge and Si (SuperCDMS, blue dashed) can access other light dark matter parameter space below 10 GeV. The plot was generated by <http://dmtools.brown.edu/>

3.3.2 OTHER DARK MATTER SEARCHES WITH LXe TPCs

The available **SUSY** parameter space has dwindled greatly in the last few decades, due in large part to the success of this detector technology. Coupled with no observation of **SUSY** at the **LHC!**, experimentalists are beginning to look to other models and parameter spaces for dark matter. New technologies are being developed and refined for new dark matter candidates, but already existing, well-understood detector technologies such as dual-phase **TPCs** can also be employed in the search for non-**WIMP** dark matter.

In their first **WIMP** search results, the Xenon10 collaboration imposed an analysis threshold of 4.5 keV_{nr} [66]. The first **LUX** results set an analysis threshold of 4.3 keV_{nr} (with $2 < S1(\text{phd}) < 30$ and $S2(\text{phd}) > 200$; $S2(\text{electrons}) \gtrsim 8$) [67]. The first Xenon100 results set an analysis threshold of 8.7 keV_{nr} ($4 < S1(\text{phe}) < 20$ and $S2(\text{phe}) > 300$; $S2(\text{electrons}) \gtrsim 10$) [68]. Such thresholds are common practice, and are set by the light-collection efficiency of the detector; the detection threshold is much lower. Dual-phase **TPCs** are sensitive to events which produce a single electron, due to the internal amplification of the $S2$ signal; the reason for setting analysis thresholds is to ensure the presence of an $S1$ in the event. Without both $S1$ and $S2$ in the event, the full (x,y,z) position cannot be reconstructed, and so a fiducial cut cannot be applied. Sorensen showed that the Xenon10 $S2$ pulse width carries a mild z -dependence [69], and so larger detectors with a long drift time may gain reliable z -position reconstruction via $S2$ pulse width [70]. Improvements in analysis techniques such as this allow dual-phase xenon **TPCs** to reach lower **WIMP** masses, and even other dark matter models.

In 2011 the Xenon10 collaboration presented a search for low-mass (5 - 20 GeV) dark matter [71]. The detector conditions were distinct from the Xenon10 **WIMP** search in [66]: the secondary scintillation gain was about 12% higher, and the $S2$ -sensitive trigger threshold was set at the level of a single electron. With this, the collaboration carried out a standard **WIMP** analysis (i.e one based on the procedure presented in 3.3.1.2), with a lowered $S2$ analysis threshold of 4 electrons (1.4 keV_{nr}). Why they did not proceed down to the detection threshold of 1 electron is very interesting; and is discussed further in Chapter 8. Since Xenon10 is a small detector, they were not able to take advantage of $S2$ -width z -correlations, but they employed a radial fiducial cut and other analysis techniques to produce the result in Figure 23, which also shows the Xenon10 standard **WIMP** analysis for comparison.

A few years later, Essig et al. used the information reported in [71] and other Xenon10 publications to produce the first direct detection limits of sub-Gev dark matter [72]. The detection threshold for **WIMPs** in **LXe**

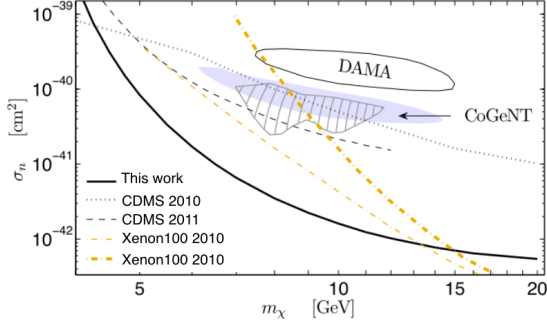


Figure 23: Xenon 10 low-mass WIMP limit extended the range of the standard WIMP result.

decreases sharply for $M_{WIMP} \lesssim 10 \text{ GeV}$; however, this detection threshold is based on the assumption that the dark matter is interacting only with the xenon nucleus. If sub-GeV dark matter scatters with atomic *electrons*, as opposed to nuclei, then it can produce observable signals of a few electrons. In L_{Xe} TPCs the S1 signal is lost due to light collection, and the few electron signals are observable as S2s. The approach in the paper is to follow approximately the same procedure as in Section 3.3.1.2, with a few but significant substitutions. The E_R in Equation 33 must now account for the binding energy of the electron, and take a different form to refer to the recoil of the electron and not the nucleus. The cross section of interest is now σ_e , the sum over all of the differential ionization cross sections for electrons in the (n, l) shell. For a dark photon with mass $O(\text{MeV-GeV})$ coupled to the visible sector via kinetic mixing (a very generic class of standard model extensions discussed in Chapter 2.5, Essig et al. set the exclusion limit in the $m_{DM} - \sigma_e$ plane in Figure 24 (left). If there is some momentum-transfer enhancement due to e.g. scattering through an electric-dipole moment, $\sigma_e \rightarrow \sigma_e F_{DM}(q) \equiv \bar{\sigma}_e$. Essig set exclusion limits for such dark matter candidates in Figure 24 (right).

In addition to the dark sector, dual-phase TPCs can search for other dark matter signals with scattering on electrons. Annual modulation searches (in ER or NR) can provide clues to dark matter. Such searches take advantage of the fact that v_E varies with the rotation of the earth around the sun, reaching a maximum in June and minimum in December. The modulation in v_E leads to a modulation in the recoil rate observed in the detector. Searches for dark matter-induced rate modulations can offer a generic approach to identify dark matter interactions, complementary to the model-driven dark matter searches. The LUX experiment did such a search, looking at ER modulations in an energy rage of interest (2-6 keV_{ee}). This energy range was chosen to overlap with the DAMA/LIBRA Collaboration's long-standing and controversial claim of dark matter modulation

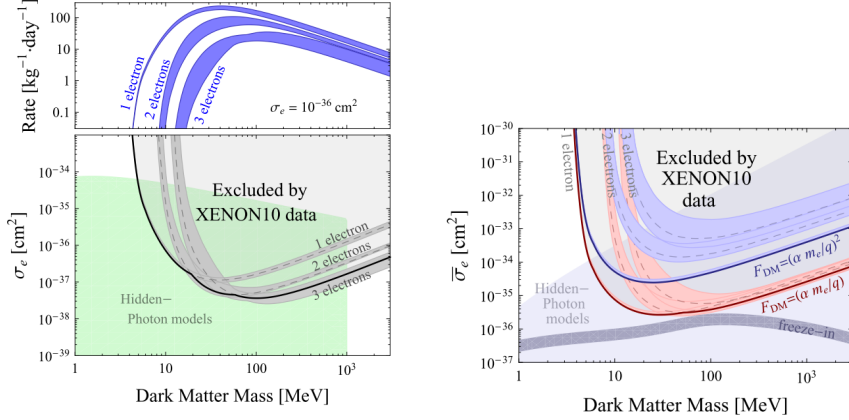


Figure 24: (left) Top: Expected 1,2,3-electron signal rates for Sub-GeV DM with $\sigma_e = 10^{-36} \text{ cm}^2$ and Bottom: exclusion limit set with Xenon10 few-electron signals. (right) Exclusion limits for dark matter scattering through an electric-dipole moment (red) and through a very light ($\ll \text{keV}$) mediator (blue)

on a target of NaI(Tl), which appears strongest around a recoil energy of 3 keV_{ee}. LUX found no significant indication of rate modulation [73]. If future large dual-phase TPCs like XenonNT and LZ observe a NR WIMP signal, the additional positive identification of a modulation signal of the NR signal would be a smoking-gun for WIMP discovery.

Another dark matter candidate that could produce an electron recoil signal in xenon is the axion (or more generally, axion-like-particles). For searches such as these, a signal model is produced from the spectrum of axions from different sources, such as galactic axions or solar axions. The resulting signal model is an ER spectrum accounts for finite detector energy resolution and threshold. The signal model spectrum is compared to the observed ER spectrum in the appropriate energy ranges, resulting in a confidence statement mass of the axion m_A and the axio-electric coupling g_{Ae} . The results of searches for solar axion and galactic axion signals are shown in Figure 25.

Finally, a model-independent search for LIPs is possible in dual-phase xenon TPC. As discussed in Chapter 2.5, LIPs appear in dark sector models with a masses dark photon, where another dark sector particle χ couples to the standard model electron via kinetic mixing of the dark photon and standard model photon. LIPs deposit energies that can be described with particles of effective fractional charge. Chapter 5 describes the signal model and analysis method to search for LIPs in LUX.

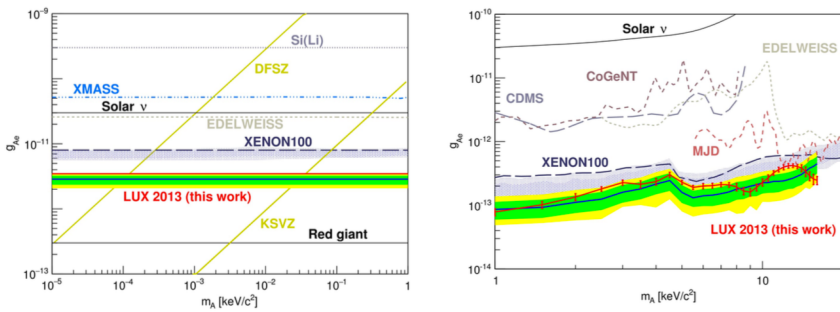


Figure 25: (left) Recent limits on solar axion coupling and mass (right) recent limits on galactic axion coupling and mass. Figure taken from [74].

PART II

BIG SCIENCE

This section describes research done with the LUX Detector.

4

THE LUX DETECTOR

4.1 LUX OVERVIEW

The [LUX](#) detector was an ultra-low background dual-phase liquid xenon TPC that set world-leading limits on [WIMP](#) interactions.

[LUX](#) began underground commissioning in July 2012, moving to the 4850 level (4300 m.w.e) of Sanford Underground Research Facility ([SURF](#)) in Lead, South Dakota. The [LUX](#) Collaboration’s first [WIMP](#) search exposure was for a period of 85.3 live-days, acquired between April 2013 and August 2013. This period of time is referred to as Run03, and the [WIMP](#) result is referred to as WS2013. The detector then underwent a grid conditioning campaign to improve voltage capabilities, followed by a series of extensive calibrations to characterize the new operating conditions. The detector then ran for a period of 332 live-days from September 2014 to May 2016 (Run04, WS2014-2016), ending with decommissioning in September 2016. Run03 and Run04 had distinct operating conditions and calibrations. The [LIP](#) search in Chapter 5 was carried out using Run03 data, and the calibrations in the latter half of this chapter describe the detector conditions as they were in Run03.

4.2 INTERNAL COMPONENTS

The active volume of [LUX](#) was composed of 300 kg of liquid xenon, instrumented with two arrays of Hamamatsu R8778 Vacuum Ultra Violet ([VUV](#))-sensitive [PMTs](#) viewing the liquid region from the top and bottom. Both arrays were composed of 61 [PMTs](#) that detected S1 and S2 photons from particle interactions in the active liquid volume, and were held in place by copper mounting blocks. The [PMTs](#) were tightly packed in a hexagonal formation to maximize light collection. The xenon-facing surfaces of copper [PMT](#) mounting blocks were covered with [PTFE](#) tri-foils to reflect the 178 nm light, since copper is a poor reflector of [VUV](#) light.

The active region was defined by a series of strung wire or mesh grids: the cathode grid was at the bottom of the detector, and the gate grid was 48.3 cm above the cathode when cold. These two grids formed the drift

field, which was 180 kV/cm during Run03. The region is known as the drift region, it is where particle interactions occur. The anode mesh plane was 1 cm above the gate grid, and the xenon liquid level was held constant between these two electrodes by a spillover weir. The anode and gate form the extraction region of the experiment, where electrons are extracted across the liquid-gas boundary and undergo proportional scintillation to form S2. There are two additional grids, the top and bottom grids, which are placed 2 cm from the top and bottom PMT arrays to insulate the PMTs from the high fields produced by the other grids. The top and bottom grids were held at approximately the same voltage applied to the PMTs. All electrodes were 88%-99% optically transparent at normal incidence, and made of stainless steel 316. The major components of LUX are shown in Figure 26

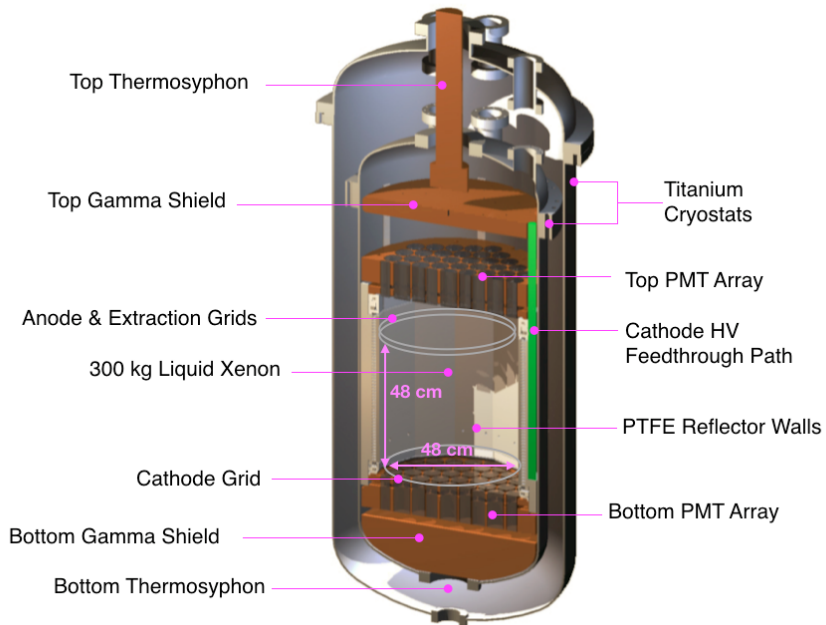


Figure 26: Major components and dimensions of the LUX detector.

The insides of the detector walls were lined with 12 PTFE panels, which made the exact detector geometry a dodecagonal prism with flat faces, instead of a cylinder one rounded face. Immediately behind the PTFE were 48 copper field-shaping “rings” (dodecagons). The rings were vertically separated by 1 cm, and the gate-to-cathode voltage was graded evenly over the rings by a resistor chain connecting the rings.

Below and above the PMT mounting blocks were two large solid copper domes which act as gamma shields and also function as thermal mass that aid in keeping the detector temperature stable. The bottom dome also acts as a heat exchanger to quickly re-thermalize incoming xenon

gas (from the circulation system) as it enters the liquid region, and minimizes the volume filled with non-active liquid xenon. See Figure 27 for details of the field-shaping rings and copper shields.

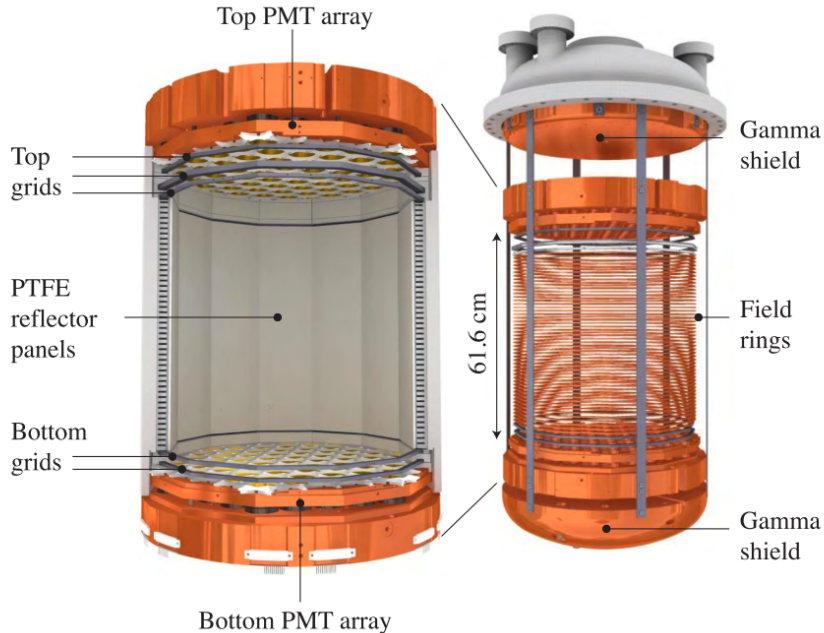


Figure 27: Field-shaping rings detail

More details about the internal components can be found in C. Faham’s PhD thesis [54].

4.3 EXTERNAL COMPONENTS

The [LUX](#) cryogenic system was based on thermosyphons, which deliver “cooling power” to solid copper cold heads, which are in thermal contact with the liquid xenon space. A simplified diagram is shown in Figure 28. A thermosyphon is a closed-loop cooling device containing a thermal messenger gas; N₂ is a common choice and was the choice for the [LUX](#) thermosyphons. The top of the thermosyphon is immersed in a bath of liquid nitrogen, and the bottom is in thermal contact with the liquid xenon space. The internal messenger gas condenses at the top and drips down to the cold head, where it absorbs heat from the xenon space, evaporates, and returns to the top of the thermosyphon to condense and repeat the cycle. In this manner, heat from the liquid xenon space is transferred to the external nitrogen bath, which boils off and must be periodically replenished. The pressure of the internal nitrogen messenger gas can be adjusted, providing more or less cooling power as desired. The [LUX](#) ther-

mosyphons were also instrumented with resistive heaters, for further fine control. Four thermosyphons were used to operate the LUX detector stably at 175 K with a xenon vapor pressure of 2 bar.

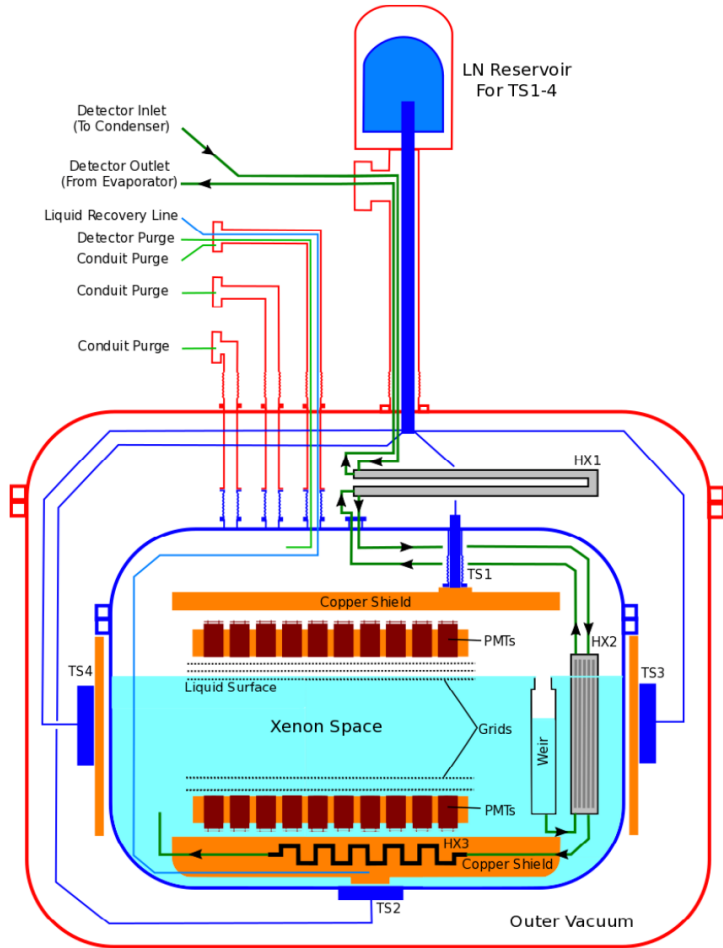


Figure 28: A simplified diagram of the LUX cryogenic system. [75]

The spillover liquid xenon from the liquid-level-setting weir mentioned above was directed into a circulation system through a series of heat exchangers that helped cool clean, incoming xenon gas. The xenon circulation was driven by one twin-head KNF double-diaphragm pump, which pushed liquid xenon from the spillover weir through a SAES MonoTorr heated zirconium getter to remove non-noble impurities before returning the clean xenon gas into the detector. A sampling system was able to pull xenon gas samples from different parts of the circulation system and measure impurity content, as well as test for the presence of ^{85}Kr [76], a troublesome beta emitter which must be removed from the xenon prior to carrying out a successful WIMP search.

The circulation pump was installed in parallel with a backup pump, which could be switched on immediately in case of a pump outage. Flow was regulated to the system by two high-flow Mass Flow Controller (MFC)s. Additional low-flow MFCs controlled purge flow through the cabling conduits in Figure 28 to ensure gas flow was away from the detector and prevent any contaminants from diffusing into the active xenon space.

Internal calibration sources were plumbed in to alternate flow paths of the circulation system. Xenon gas could be directed through a substrate source, such as the ^{83m}Kr source described below, to pull ^{83m}Kr into the detector volume. A bottle containing a source such as the CH_3T source described below could be used to deposit the gaseous source in an evacuated section of pipe. Xenon could then be directed through the section of pipe containing the source, sweeping it into the detector volume.

Lastly, LUX was placed in a 7.6 m diameter, 6.1 m high water tank (Figure 29). The shielding provided by the water tank attenuated the γ background from the cavern walls and thermalized neutrons from cavern background radioactivity and muon spallation. The water tank provided superior shielding from cavern radioactivity such that the detector backgrounds were dominated by the radioactivity of internal detector components, which in turn were controlled through a strict campaign of cleanliness and choice of detector materials [77], [78]. Vertical tubes visible in Figure 29 were used to deploy external calibration sources at different heights, such as ^{137}Cs , which were directed into the detector via a collimating source assembly.



Figure 29: A photo of the LUX detector installed inside the water tank.

The LUX detector water tank and material screening achieved a very low background in the WIMP search energy range shown in Figure 30

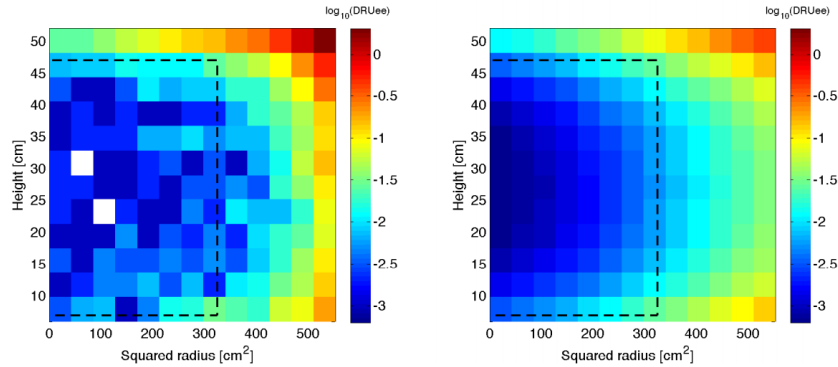


Figure 30: Backgrounds distributions in squared radius and height for expected (right) and measured (left) backgrounds in the energy range 0.9–5.3 keV_{ee} (2–30 phe S1) for the 85.3 live-day Run03 WIMP exposure. Black lines show the 118 kg fiducial mass. Units are $\log_{10}\text{DRU}_{ee}$, electron equivalent differential rate units, i.e. $\text{keV}^{-1}\text{kg}^{-1}\text{day}^{-1}$. Figure from [78].

4.4 TRIGGER AND DATA ACQUISITION

Cabling for PMTs and other monitoring instrumentation were routed from the inner detector volume to the outside via conduits illustrated in in Figure 28. A flow char illustrating the signal path is shown in Figure 31.

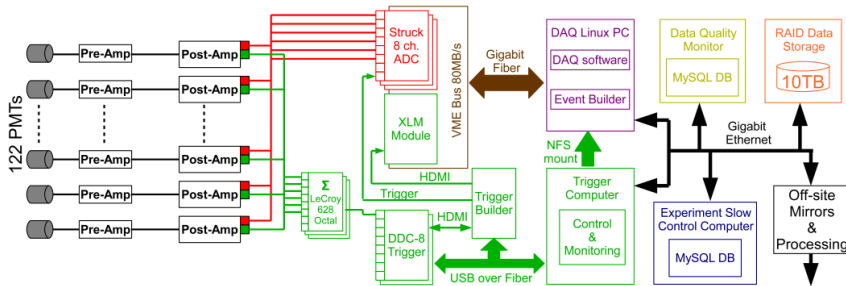


Figure 31: Overview of the LUX trigger system. Figure from [79].

The PMT signals were shaped and amplified by two sets of amplifiers. These analog voltage waveforms were then digitized by Struck Analog-to-Digital Converter (ADC)s, with 14 bit, 100 MHz sampling (1 sample every 10 ns). A copy of the analog PMT voltage waveforms passed through

the LUX Field Programmable Gate Array (FPGA) trigger system, which signaled the data acquisition computer to save the waveforms when they passed above a certain threshold, and stop when they fell below the threshold. Each of the 122 PMTs was dedicated its own channel in the recorded data, so recording only the channels that passed threshold allowed for a great amount of data reduction. This technique is called Pulse Only Digitization (POD). A POD threshold of 1.5 mV was used for LUX, which resulted in a single photoelectron efficiency of $> 95\%$ [58]. A figure showing the POD threshold and example waveform are shown in Figure 32.

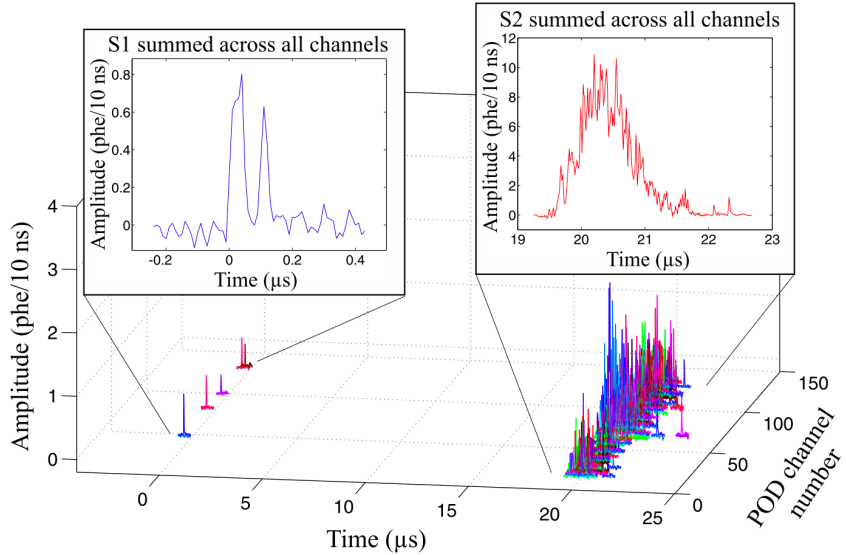


Figure 32: An example recorded event. Channels that do not pass the POD threshold are not recorded. The waveforms are summed over all channels to produce the S1 and S2 [79].

The channel-wise POD data is written continuously to disk as the ADC memory buffer fills; this is the rawest and least filtered form the LUX data that is saved in binary format with the `.dat` extension. The Event Builder takes the raw data and extracts portions located in a pre-trigger and post-trigger window. A additional hold-off time is applied after the post-trigger window to assure PODs are not duplicated by the subsequent event. The pre- and post-trigger windows for Run03 were set to be $500 \mu s$, chosen to ensure both S1 and S2 pulses were contained in the same event. The maximum electron drift time in Run03 was $322 \mu s$, so a pre- and post-trigger time of $500 \mu s$ ensured no S2 would appear without its partner S1. Both types can pass the POD threshold and signal the DAQ computer to save the waveforms, but some small S1s are may not cross the threshold and must be “found” only at the event-building stage.

The Event Builder then saved the waveform data in binary format with the `.evt` extension.

4.5 DATA PROCESSING

After event-building, the waveform `.evt`-files were sent off site for additional processing. The `LUX` Data Processing Framework (`DPF`) extracts essential information from the waveforms and produces Reduced Quantity (`RQ`) files with the `.rq` extension. The `DPF` is modular, and can be applied repeatedly to the same `.evt` data with different settings if desired. `RQ` files include event-level information (e.g. trigger timestamp), pulse-level quantities (e.g. pulse type, pulse area), and some channel-level quantities (e.g. pulse area recorded by each `PMT`). The `DPF` classifies pulses as one of five types: S1, S2, Single Photoelectron (`SPHE`), Single Electron (`SE`), and Else (for pulses that do not fit one of the previous four types). The pulse-finding and classification algorithm was designed and optimized for the `WIMP` search, and is crucial in identifying `WIMP` “golden events”, which are single-scatter interactions with only one S1 and one S2 in the event. Detector backgrounds such as gammas often scatter more than once in the active volume, producing an event with one S1 and multiple S2s. The pulse-finder and classifier also play a large role in `LIP` search, which is discussed more in Chapter ch:lips. An example of pulse identification for a multiscatter event is shown in Figure 33

Following identification of S1 and S2 pulses, the `DPF` position reconstruction module is run. This module uses the Mercury algorithm, originally developed for the ZEPLIN-III `LXe TPC` [80], which is based on maximum-likelihood to find the best (x,y) position of the event. Mercury uses Light Response Function (`LRF`s), obtained for each `PMT`, to predict the response of the `PMT` to interactions at some arbitrary position of the `PMT`. The `LRF`s were obtained using calibration data, of which ^{83m}Kr was the most important for position reconstruction. The position reconstruction method and `LRF`s are discussed in more detail in [81].

The `DPF` also applies calibration constants to the data. Calibration constants, many of which change over time, are tracked and recorded in the `LUX` Electronic Log (`LUG`), which produces date-specific record files in XML format, which in turn determine the settings for some of the `DPF` modules. For example, the ^{83m}Kr calibration (see Section 4.6.2) was used to normalize S1 pulse areas. The photon detection efficiency for S1s varies with z-position, with events occurring near the bottom `PMT`s 50% more likely to be detected than those near the liquid-gas boundary. The `DPF` applies corrections like this to several RQs, and both the corrected and uncorrected versions are kept.

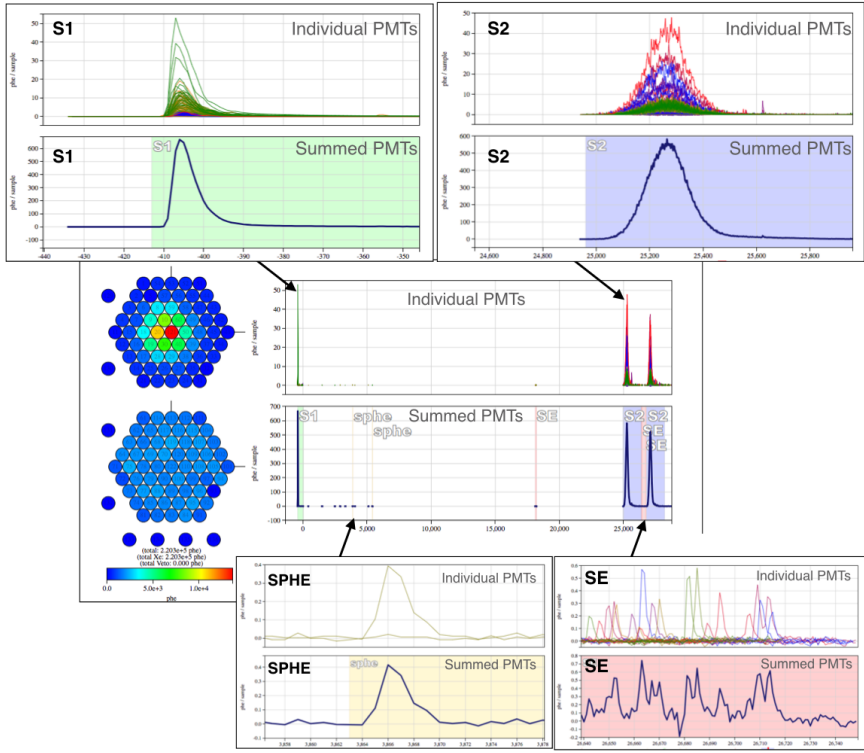


Figure 33: An example of [LUX](#) pulse classification showing individual pulses.

4.6 CALIBRATIONS

Several novel calibration methods were developed by the [LUX](#) Collaboration to fully characterize the detector. The superior self-shielding ability of [LXe](#) detectors also makes them difficult to calibrate. Sources placed external to the detector cannot penetrate the fiducial volume very effectively; since high-statistics are desired for calibration data, relying on external sources becomes untenable. The solution, then, is counterintuitive: purposely introduce radioactive material into painstakingly developed, ultra low-background, fiducial volume of the detector. For such a source to not destroy the ability to carry out a [WIMP](#) search, it must either (i) be short lived or (ii) be effectively removed by getter on a short timescale. [LUX](#) demonstrated that ^{83m}Kr fit the former [82] requirement and tritiated methane (CH_3T) fit the latter [83].

4.6.1 ENERGY RECONSTRUCTION

This section covers the energy calibration of **LUX**. Recall from Section 3.2.1 that the electron-equivalent energy of an event in a dual phase xenon TPC is reconstructed as follows:

$$E = W \left(\frac{S1}{g1} + \frac{S2}{g2} \right) \quad (39)$$

Two or more calibration line sources of different energies are required to fit for the detector gains g_1 and g_2 . The **LUX** experiment used a suite of sources to calibrate the energy response of the detector, shown in 34. The ^{83m}Kr is an injected source distributed in the entire internal volume. The ^{137}Cs is an external source lowered at different heights into the source tubes. The xenon lines, ^{131}Xe , ^{129}Xe , ^{127}Xe , are internal sources of cosmogenic origin and were only present early in Run03.

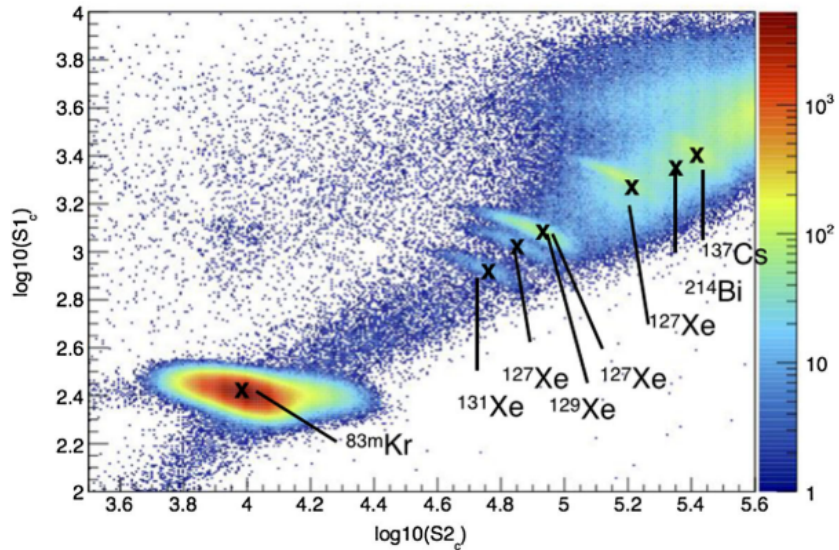


Figure 34: Plot showing calibration sources (Figure from [58]. The axis label subscript c denotes corrected variables with calibration for geometrical effects and electron lifetime (these corrections are discussed in Section 4.6.2).

The average $S1$ and $S2$ of each calibration source is normalized to the true energy:

$$(S1, S2) \rightarrow \left(\frac{\langle S1 \rangle}{E}, \frac{\langle S2 \rangle}{E} \right) \quad (40)$$

and a line $y = mx + b$ is fit to the transformed variables, where the slope is $m = -g_1/g_2$ and the y-intercept is $b = g_1/W$. Such a plot is called a Doke plot. The sources from figure Figure 34 are shown normalized in a Doke plot in Figure 35.

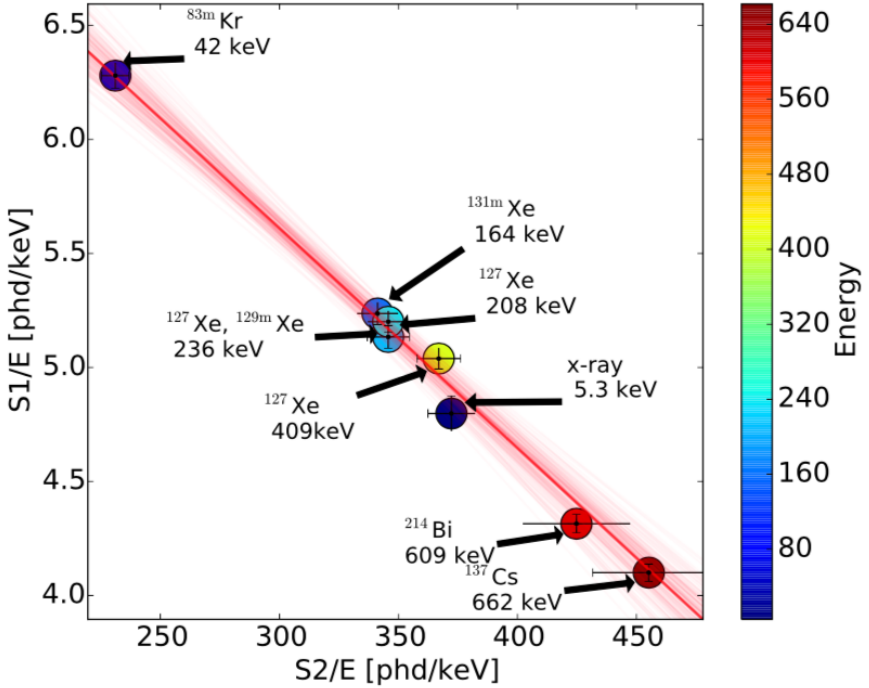


Figure 35: Doke plot used to fit g_1 and g_2 for LUX Run03 (Figure from [58])

From the fit in Figure 35, the LUX gains for Run03 were measured to be $g_1 = 0.117 \pm 0.003$ phd/photon and $g_2 = 12.1 \pm 0.8$ phd/electron. g_2 depends on a combination of the EEE and the number of photons produced by a single extracted electron – it is useful to know both values. Single electrons are periodically emitted into the gas and undergo proportional scintillation. This phenomenon is well known in liquid xenon detectors and is discussed further in Chapter 8. A sample of pure single electrons was collected to find the average number of S2 photons produced by one electron, referred to the single electron size. The single electron size in Run03 was a skew-gaussian with mean 24.66 phd and a $1-\sigma$ width of 5.95 phd. Combing this with g_2 gives an EEE of $49\% \pm 3\%$ [58].

4.6.2 METASTABLE KRYPTON-83 (^{83m}Kr): A MULTIFUNCTION CALIBRATION

The ^{83m}Kr source used by LUX was ^{83}Rb deposited on a charcoal substrate. Gaseous xenon within the circulation system was diverted over the char-

coal substrate, where it could sweep ^{83m}Kr on a flow path through the getter, and then into the detector.

^{83m}Kr decays by two steps releasing a total energy of 41.5 keV. The two branching ratios that dominate are first the internal conversion and subsequent Auger emission of a 32.1 keV β followed by another internal conversion and Auger emission of a 9.4 keV β , with an intervening half-life of 154 ns. The time structure of the decay sometimes yields two S1s, called S1a and S1b. If the second 9.4 keV β is prompt (i.e. within the timing resolution of the detector), then only one S1 is observed. The S2s are always merged because (1) the low energy of the decays made the energy depositions $O(10 \mu\text{m})$ from each other, smaller than the position resolution of the detector $O(1 \text{ mm})$ (2) the close timing of the two decays was smaller than the typical electron diffusion distances during drift $O(1 \text{ mm})$, merging the two electron bunches together into one S2 [82].

^{83m}Kr was a workhorse calibration source for [LUX](#), with ^{83m}Kr injections performed weekly at activities ranging from 10 Bq to hundreds of Bq, depending on the specific calibration goal. ^{83m}Kr was found to mix uniformly in the detector within 10 min of the injection, and would decay (half life 1.83 hours) back to an acceptable [WIMP](#) search background rate within a day, or few days, depending on the injected activity [82]. The combined energy of the ^{83m}Kr was well out of the [WIMP](#) search energy range, so no long-term pollution, though unlikely, was risked. ^{83m}Kr was used for two main calibrations, described below.

Pulse Area Corrections Detector efficiencies and gains can vary over time and position within the detector. ^{83m}Kr served as a “standard candle”, which produced monoenergetic signals with uniform initial light and charge yields distributed uniformly throughout the active volume. The efficiency for detecting the initial light yield as an S1 was dominated by spatially varying geometrical light detection efficiency. The areas of the S1s were binned in 3D, and the averages were found for each bin. A correction map was then constructed as the inverse of the S1 areas, normalized to the S1 amplitude at the center of the detector. The map of relative S1 amplitudes in Figure 36 (left) shows the strong z -dependence for S1 light collection. The corrections for S2 areas were more complex, as detection efficiency for the initial charge yield as an S2 depends on the presence of electronegative impurities, electron extraction efficiency, production of proportional scintillation photons, and then detection of those photons in PMTs. The xy - and z - dependence for S2s are corrected in two separate maps. The electronegative impurities caused a strong z -dependence in S2 size – events originating at the bottom of the detector must drift longer and so were more likely to encounter and lose electrons to impurities. The z -dependent S2 area correction map was an exponential function of drift time, normalized to unity at the liquid surface. The xy -dependence

was from detector conditions such as pressure, liquid level, and electric field deflection from the grid. The xy -correction map for S2s was normalized to (0,0) in the x-y plane. Examples of both the z and xy S2 area correction maps can be seen in Figure 36 (right).

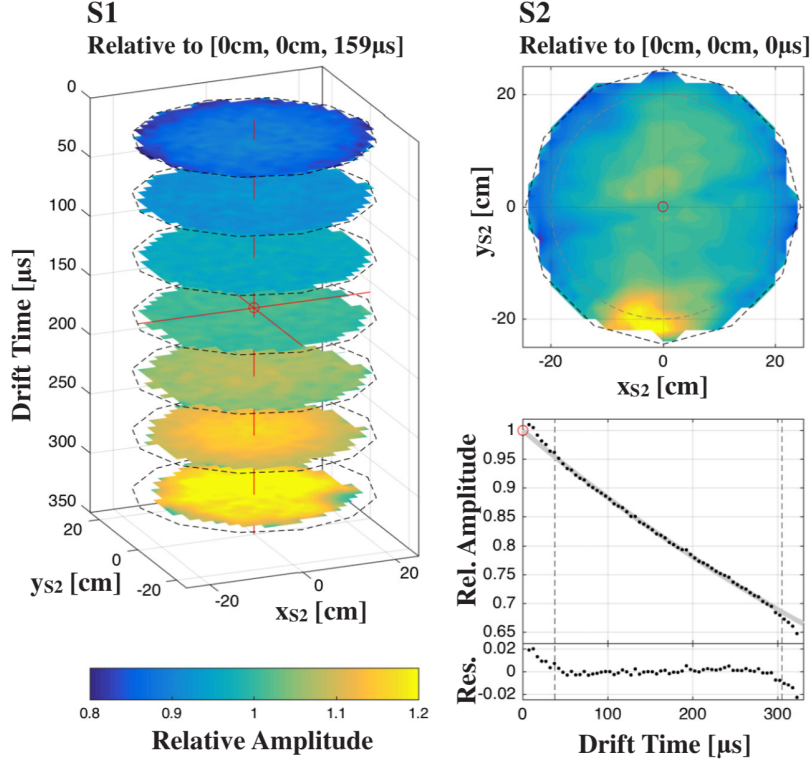


Figure 36: Spatial dependence of pulse area corrections for S1 (left) and S2 (right) from an example ^{83m}Kr calibration. The red circle indicates normalization point. (Figure from [82])

Position Corrections 3D position reconstruction depends on a full understanding of the path electrons take from an interaction site to the position observed after extraction at the surface. The reconstructed position of the proportional scintillation signal in the xy-plane, based on the Mercury algorithm, is referred to “S2 coordinates”, often with subscripts (x_{S2} , y_{S2}). The real coordinates may be displaced from (x_{S2} , y_{S2}) due to, for example, a radial field pushing electrons inwards deep in the detector. In fact, there was a small radially inward component to the electric fields in LUX Run03 due to the geometry of the field cage and grids (Figure 37). The spatial distribution of reconstructed ^{83m}Kr events was used to verify a COMSOL multiphysics electric field model of the detector by drifting electrons in simulation under the electric field model conditions. This field model could then be used to transform events from S2 coordinates to real (x,y) coordinates, however this was not done for Run03. Instead,

the ^{83m}Kr data itself was found to be more precise in for position corrections, since it didn't rely on the accuracy of the field model or electron drift simulation (Figure 38). The electric field conditions were very different in Run04, and so extensive calibrations and field maps were used to map S2 coordinates to real coordinates [84].

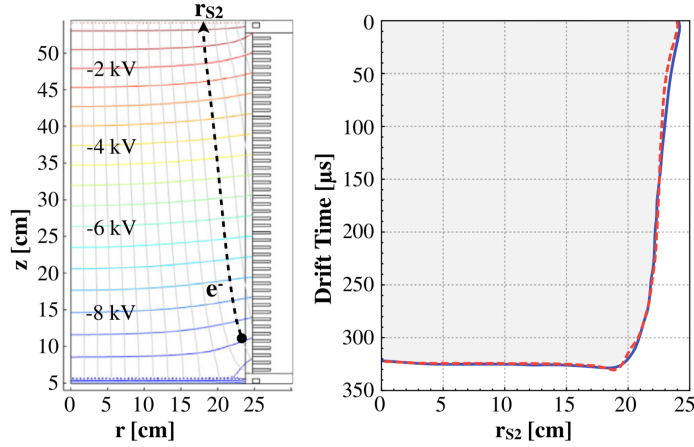


Figure 37: (Left) A simplified 2D COMSOL model showing electric field lines and equipotentials for the LUX detector in Run03. A radially inward component is seen. (Right) The resulting edge S2 coordinates of a uniform distribution of electrons drifted under the electric field model is shown in solid blue. The edge S2 coordinates of from ^{83m}Kr data is in dashed red; it is consistent with the field model prediction. Figure from [82]

In addition to the small radial dependence, the electric fields illustrated in Figure 37 also vary in magnitude. The two decays of ^{83m}Kr can be leveraged to directly probe the magnitude of the field, as they exhibit different field dependence. The ratio of S1a to S1b increases with field, and provides a measure the spatial dependence of the magnitude of the electric field. A highly variant electric field would affect recombination, and cause different light and charge yields at different positions in the detector, in turn affecting sensitivity. The fields measured via this method in Run03 were found to only cause corrections on the order of a percent and so no field-dependent corrections were applied [82]. However, in Run04 the ratio technique was of central importance (see [85] [84] [82] for more detail). The result of the ratio method for measuring electric field magnitude is shown in Figure 39 for Run03 fields.

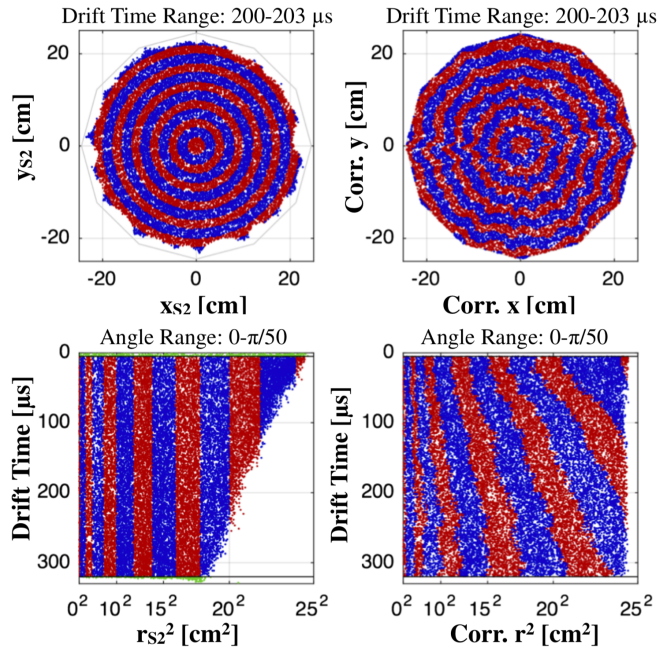


Figure 38: The effect of radial position mapping between S2 coordinates (left) and real coordinates (right). The top panels show a thin horizontal slice of the detector and the bottom panels show a thin vertical slice. The red and blue colors are used to make the effect of the mapping visible. Note that squared radius in the bottom panels exaggerates the scale of the effect. Figure from [82]

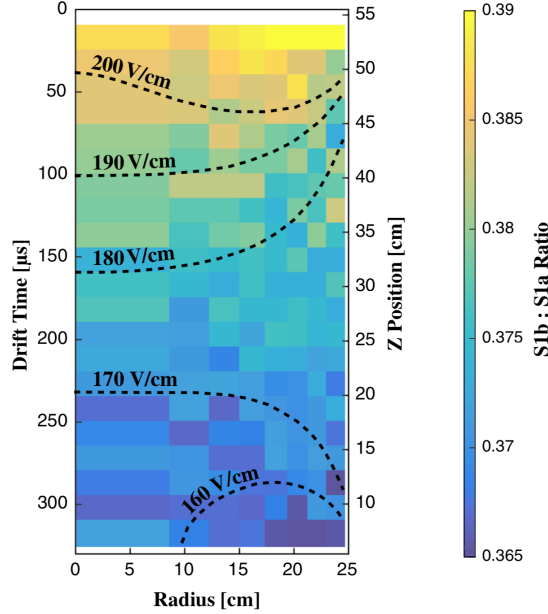


Figure 39: Field map of Run03 produced by ^{83m}Kr S1a:S1b ratio. Because only a fraction of ^{83m}Kr produce separate S1a and S1b, the bins are large to accomidate reduced statistics. Figure from [82]

4.6.3 TRITIUM BETA DECAY: CALIBRATION OF THE ER BAND AND YIELDS

In order to calibrate the **ER** band of **LUX** a β source in the **WIMP** energy range was needed. **LUX** used a gaseous tritiated methane (CH_3T) source to deliver tritium uniformly into the active volume. Tritiated methane was chosen over the molecular tritium (T_2) because it does not adsorb onto surfaces like the smaller T_2 molecule and it does not interfere with charge transport in **LXe** [83]. Tritium has a Q-value of 18.6 keV, but the spectrum peaks at 2.5 keV, with 64.2% of the decays occurring in the **WIMP** search energy range of 1 to 8 keV [83]. The half-life of tritium is 12.3 years, so efficient removal was essential. **LUX** demonstrated that once deployed, CH_3T was removed with a 6 hour time constant, returning the detector back to acceptable **WIMP** search rates. CH_3T was shipped to site in a bottle, mixed with purified xenon and released into the circulation system after the getter, to be swept into the inner volume.

The tritium energy spectrum from data is shown with the theoretical energy spectrum convoluted with the detector energy resolution in Figure 40 (left). The ratio of the two is shown in Figure 40 (right), demonstrating a 50% effective energy threshold for **ER** events at 1.24 ± 0.026 keV. The agreement between data and theory shows powerful support for the energy model $E = W(S1/g_1 + S1/g_2)$.

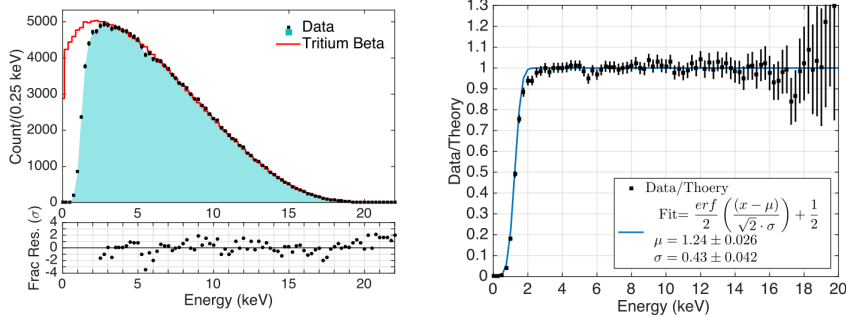


Figure 40: (Left) Plot showing the theoretical tritium beta spectrum with the spectrum obtained from data, and residuals. (Right) The ratio of data to theory convoluted with the detector energy resolution. Figure from [83]

Tritium was also used to measure the light and charge yields over a wide energy range. Figure 41 (left) shows the detected number of quanta, n_γ and n_e . Recall that this is not necessarily the number of initial quanta n_{ex} and n_{ion} that are produced, as some number of n_{ion} undergo recombination to produce additional scintillation photons. Figure 41 (right) shows the effect that event energy has on recombination. For ER events $n_{ex}/n_{ion} = 0.2$ is assumed to be constant [LUXYieldsAndRecombination], but the observed ratio n_γ/n_e is clearly energy dependent.

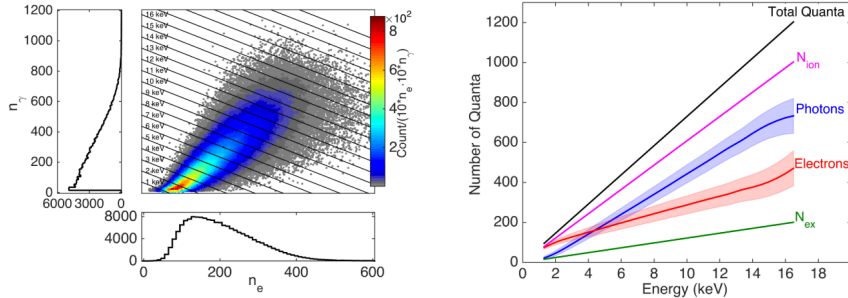


Figure 41: (Left) The measured quanta yields shown with lines of equal energy. (Right) A plot depicting the expected initial quanta yields, N_{ion} and N_{ex} , compared with the measured yield of photons and electrons. The difference is caused by the energy dependence of recombination. Figure from [83]

Lastly, as is tritium was used to construct the ER band (Figure 42 (left)), which is necessary for WIMP search. The width of the ER band is of significant interest, as it determines the nuclear recoil discrimination of the detector. The number of ER events from the tritium calibration that occur below the nuclear recoil band mean is known as leakage fraction (f),

and is shown as a function of energy in (Figure 42 (right)). The average **ER** discrimination efficiency ($1 - f$) for Run03 was $99.81\% \pm 0.02\%(\text{stat}) \pm 0.1\%(\text{sys})$, where the systematic error comes from the error on g_1 and g_2 . This measurement of discrimination efficiency relies on knowing the mean and width of the **NR** band, which is discussed in the next section.

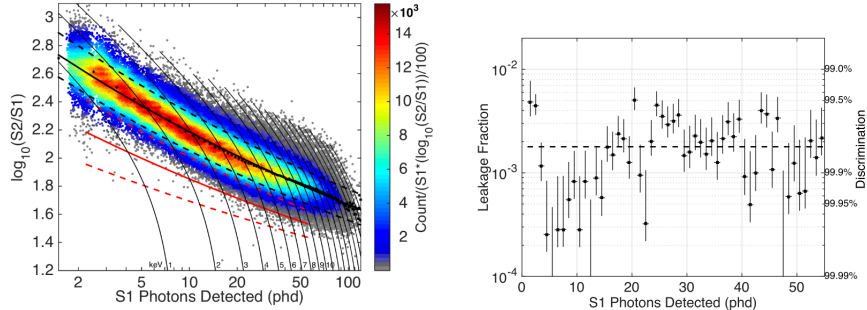


Figure 42: (Left) The **ER** band for in **WIMP** search energy range obtained from the tritium calibration. (Right) Leakage fraction of **ER** events below the **NR** mean in the **WIMP** search energy range. Knowledge of the **NR** band comes from the **DD** calibration detailed in Section 4.6.4. Figure from [83]

4.6.4 DEUTERIUM-DEUTERIUM (DD) NEUTRONS: CALIBRATION OF THE NR BAND AND YIELDS

Low energy neutrons from a **DD** generator was used to calibrate the **NR** response and signal yields for **LUX** in the **WIMP** search energy range. A photo and diagram of the calibration scheme are shown in Figure 43. Following Run03, **LUX** employed the **DD** generator to deliver a collimated beam of 2.45 MeV neutrons into the **TPC**. As Figure 43 shows, the generator was positioned outside the water tank, but when aligned with the neutron conduit (a Polyvinylchloride (**PVC**) tube of air), deposited neutrons into the **LXe** space. The **DD** calibration leverages known kinematics of neutron scattering, the known incoming neutron energies, and the known detector gains g_1 and g_2 to develop a complete characterization of low-energy **NR** in **LUX**. The method is summarized here, but details are available in [62].

First, charge yield was derived from a population of multiscatter events: those with one **S1** (the **S1s** are merged due to simultaneous collection of **S1s**) and two **S2s** (separated in space and z-position/drift time). Neutron scattering kinematics allow for the reconstruction of energy at the first scatter site, so the unknown first **S1** is not needed to ascertain the energy

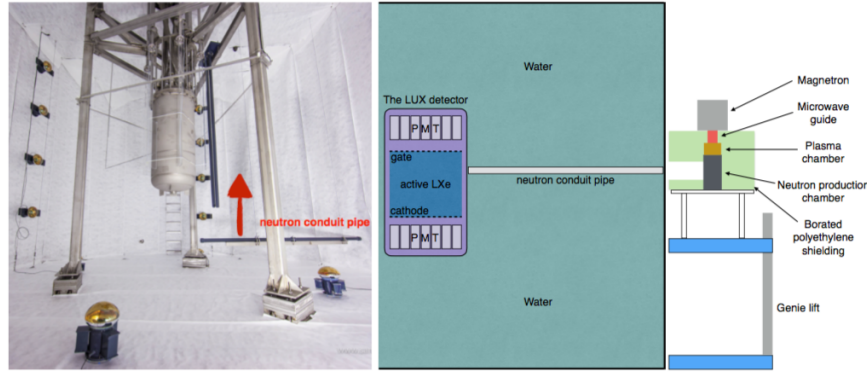


Figure 43: (Right) Photo of the water tank interior showing the neutron conduit, which is raised during **DD** calibration. (Left) Diagram of the **DD** generator and water tank neutron conduit during **DD** operation. Figure courtesy of E. Pease.

deposition. The charge yield is then obtained from the first S2 and the energy of the first scatter from kinematics.

Once the charge yield was obtained, a population of single scatter events was collected: one S1 and one S2. These events were from neutrons that scattered once the detector, and then exited. Here, the second scatter is not available to kinematically reconstruct energy, so instead the charge yield is employed to infer the energy of the single scatter. The light yield is then obtained from the S1 and the energy deposition inferred from charge yield.

It should be noted that though the **DD** generator produced monoenergetic neutrons of initial energy E_i , the energy deposited E_d by a neutron scatter is

$$E_d = E_i \frac{m_n M_{Xe}}{m_n + M_{Xe}} \sin^2 \theta_{CM} \quad (41)$$

Where m_n is the neutron mass, M_{Xe} is the xenon mass, and θ_{CM} is the scattering angle relative to the neutron conduit in the center of mass frame. The deposited energy, E_d then covers a range of energies, allowing for calibration of the **NR** band and yields over a range of energies. After determination of the light yield, the single scatter events were used to construct the **NR** band in Figure 44.

4.6.5 POWER OF LUX CALIBRATIONS

Although this thesis is concerned mainly with a search for **LIPs**, it should be noted that the extensive **LUX** calibrations allowed for excellent under-

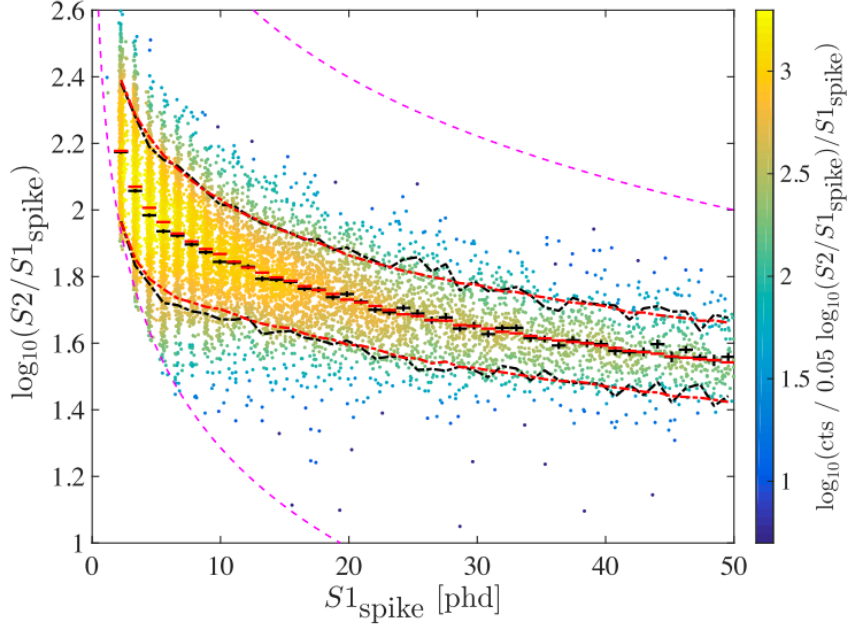


Figure 44: Calibration showing the [NR](#) band mean and width from the [DD](#) calibration. Figure from [62]

standing of the detector, resulting in a world-leading [WIMP](#) limit. In particular, the [DD](#) calibration (carried out after Run03) yielded a much better understanding of the [NR](#) band and yields, and therefore detector thresholds, than the initial AmBe neutron calibration which was carried out in the early days of [LUX](#). The power of the [DD](#) calibration can be seen in the difference between the first [LUX](#) result [67] and the Run03 re-analysis [86] shown in Figure 45. In particular, improved knowledge of the scintillation yields allowed a re-analysis threshold down to 1.1 keV_{nr} where the initial [WIMP](#) search adopted the more conservative threshold of 3.0 keV_{nr} . This improvement allowed [LUX](#) to exclude new spin-independent parameter space below a [WIMP](#) mass of 10 GeV.

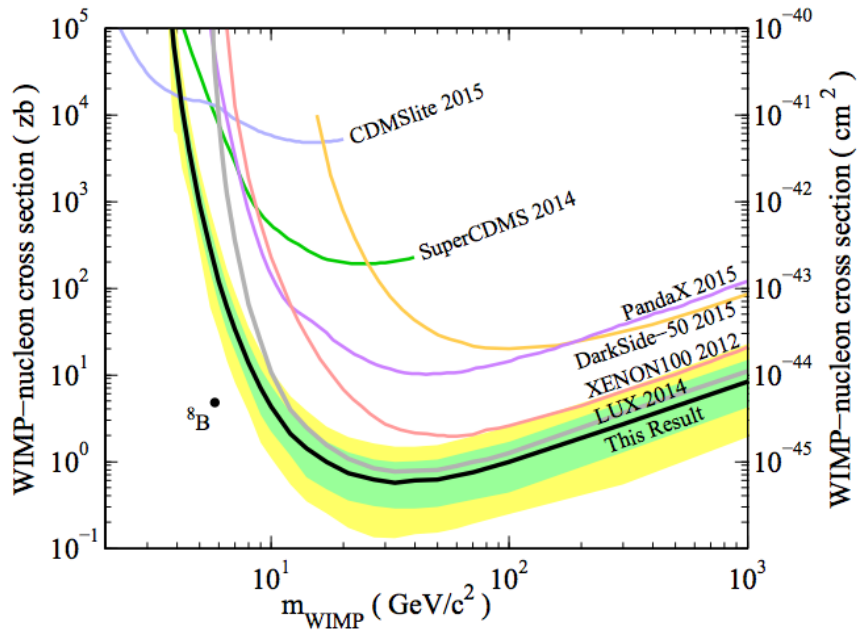


Figure 45: Improved spin-independent WIMP limit of the Run03 exposure following the DD calibration of LUX. The first Run03 limit is the gray line labelled “LUX 2014”, the improved Run03 observed limit is the black line labelled “This Result”. Figure from [86]

5

LIGHTLY IONIZING PARTICLE SEARCH

*And all this science I don't understand,
It's just my job five days a week*

— Elton John *Rocket Man*, 1972

5.1 MODELING LIP INTERACTION

5.1.1 COLLISION CROSS SECTION

A LIP interacting in the LXe volume loses energy via interaction with electrons. To model LIPs in LUX, the expression of interest is the collision cross section Collisional Cross Section (CCS). The differential CCS describes the energy lost to electrons in a single collision for incident energy of the LIP. For particles with charge ze and mass M heavier than the electron mass, m_e (“heavy” particles), the Rutherford cross section is a familiar differential CCS [87]:

$$\frac{d\sigma_R}{dE} = \frac{2\pi r_e^2 c^2 z^2}{\beta^2} \frac{1 - \beta^2 E/T_{max}}{E^2} \quad (42)$$

where r_e is the classical electron radius, E is the energy loss of incoming particle, $\beta = v/c$ of the incoming particle, and T_{max} is the maximum energy transfer possible in a single collision:

$$T_{max} = \frac{2m_2 c^2 \beta^2 \gamma^2}{1 + 2\gamma m_2/M + (m_e/M)^2} \quad (43)$$

Often the expression $T_{max} 2m_e c^2 \beta^2 \gamma^2$ for $2\gamma m_2/M \ll 1$ is used implicitly, or is referred to as the “low energy approximation” in older texts. The Rutherford cross section is a good starting point, but it describes the “hard interaction” or head-on, billiard-ball type collision of a particle interacting with free electrons. Real electrons are bound in atoms, and an incident particle can undergo “soft interactions”, in which virtual photons are exchanged. When the virtual photon matches the energy of electron

orbitals of the target material, there are resonances in the [CCS](#). The energy transfer, E , must also be finite in real atoms, where the dielectric properties modify the electromagnetic field of a moving charged particle and limit the growth of the cross section. This real-world behavior is described by a correction factor $B(E)$, also sometimes called an “inelastic form factor” [87]:

$$\frac{d\sigma_{CCS}}{dE} = \frac{d\sigma_R}{dE} B(E) \quad (44)$$

Various attempts, spanning a better half of the last century, have been made to take into account the real-world behavior of electrons bound in matter. Some of these can be found in [cite 18,27, 41-43 papers from Bichsel]. More well-known contributions are those of Bethe and Fano. In 1930, Bethe derived a cross section doubly differential in energy loss and momentum transfer using the first Born approximation for scattering on free atoms [88]. In 1963, Fano extended the method to describe atoms in solids [89]. Combining their two methods yields the Bethe-Fano cross-section, which has undergone much study and by our current understanding has been verified to be close to reality [90]. There is another method, called the Photo Absorption Ionization ([PAI](#)) model, that is easier to calculate than the Bethe-Fano cross section, and approximates the Bethe-Fano calculation very closely. This thesis uses the [PAI](#) model as a base, building the full signal model for [LIPs](#) interacting in the [LUX](#) detector.

5.1.2 PHOTO ABSORPTION IONIZATION MODEL FOR CHARGE PARTICLE ENERGY LOSS

The [PAI](#) model is also sometimes known as the Fermi Virtual Photon ([FVP](#)) or WeisÖcker-Williams approximation. A full description of the [PAI](#) model is described in detail in [91]. The complex dielectric constant $\epsilon = \epsilon_1 + i\epsilon_2$ can be thought of as encoding all the information about a medium. The real part ϵ_1 describes the polarization of the material and imaginary part ϵ_2 describes the absorptive properties. Typically both ϵ_1 and ϵ_2 are thought of as functions of ω , or incident photon energy. So $\epsilon(\omega) = \epsilon_1(\omega) + i\epsilon_2(\omega)$. This description is limited to free photons, but we desire to describe inelastic collisions as well. So $\epsilon(k, \omega)$, a generalized dielectric constant, is introduced to describe momentum transfer k to atomic electrons. The generalized dielectric constant $\epsilon(k, \omega)$ can be related to atomic matrix elements, and if desired, calculated completely and tediously. However, the [PAI](#) model allows us to avoid these tedious calculations by making specific approximations, which, when taken together, define the [PAI](#) model itself.

In particular, the PAI model approximates $\epsilon_2(k, \omega)$ by noting that typically, the momentum k transferred to an electron is much less than the energy transfer ω .

5.1.3 STRAGGLING

5.1.4 ENERGY RESOLUTION IN LUX

5.1.5 POSITION RESOLUTION IN LUX

5.2 LIP SEARCH

5.2.1 LUX RUN03 CONDITIONS

5.3 LIP SEARCH ANALYSIS

5.3.1 ENERGY CONSISTENCY

5.3.2 TRACK LINEARITY CRITERIA

5.3.3 BACKGROUND REJECTION

5.3.4 MUONS

5.3.5 GAMMAS

5.3.6 ELECTRON TRAINS?

5.4 RESULT: VERTICAL FLUX LIMIT

PART III

LITTLE SCIENCE

This section describes research with a small test bed at Lawrence Berkeley National Lab.

6

RESEARCH AND DEVELOPMENT FOR FUTURE LIQUID XENON TPCS

All systems go, are you sure?

— Peter Schilling *Major Tom, 1969*

A small test bed was built at Lawrence Berkeley National Laboratory to study various detector effects facing large [LXe TPCs](#). The test bed was built and instrumented over the course of about two years, from 2015 through 2016. This chapter describes some of the details of that instrumentation.

6.1 TEST BED APPARATUS OVERVIEW

The experimental apparatus consisted of an inner vessel, a vacuum outer vessel, and a xenon circulation system. The inner vessel was a Stainless Steel ([SS](#)) canister, topped with a 2.75 in Conflat-adaptable tower that allowed space for instrumentation cabling and [HV](#) feedthroughs. The inner vessel was offset below a 7.09 in ISO K flange, which held the (removable) vacuum outer vessel in place. Several Mini-CF ports were welded to the ISO K flange for instrumentation cabling. A large-scale overview is shown in Figure 46.

The inner vessel contained the [TPC](#). A [PTFE](#) housing cylinder fastened a [PMT](#) in place. Above the [PTFE](#) housing, a series of interlocking [PTFE](#) rings held strung wire grids and a segmented anode in place. During data taking, the entire [PMT](#) and housing were immersed in [LXe](#). The liquid level was chosen depending on the experiment at hand, approximated by the S2 width. In some cases, the [TPC](#) was “overfilled” by allowing the liquid level to rise above the anode. The segmented anode was instrumented with charge amplifiers for direct charge readout. When the [TPC](#) was overfilled, the charge amplifiers detected the ionization electrons directly from the liquid. During typical dual phase [TPC](#) operation, the charge amplifiers provided a secondary measurement of the ionization electrons in addition to S2. Two typical arrangements of the inner vessel are shown in Figure 47.

6.1 TEST BED APPARATUS OVERVIEW

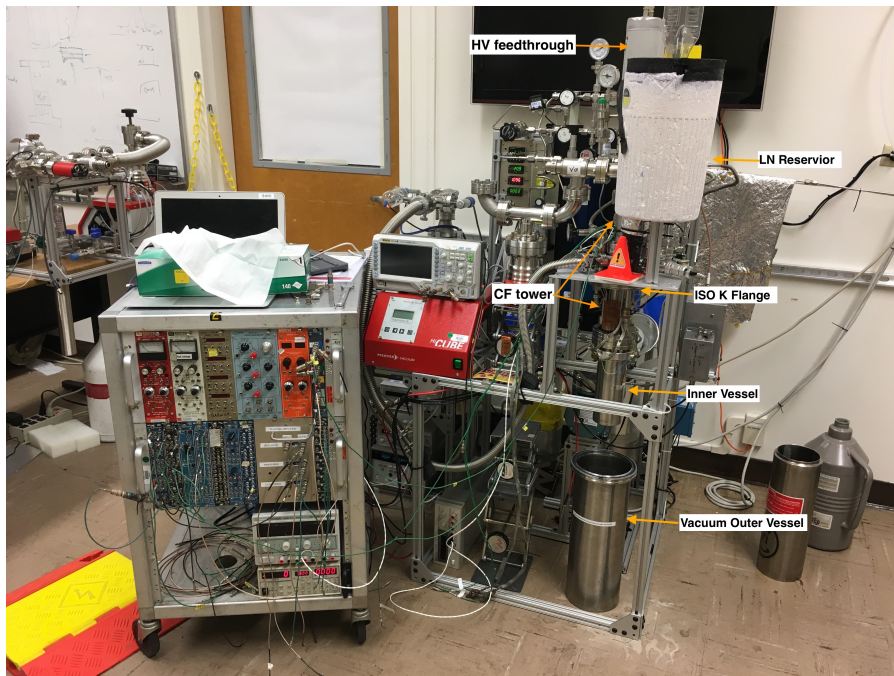


Figure 46: Large scale view of the experimental apparatus showing key parts.

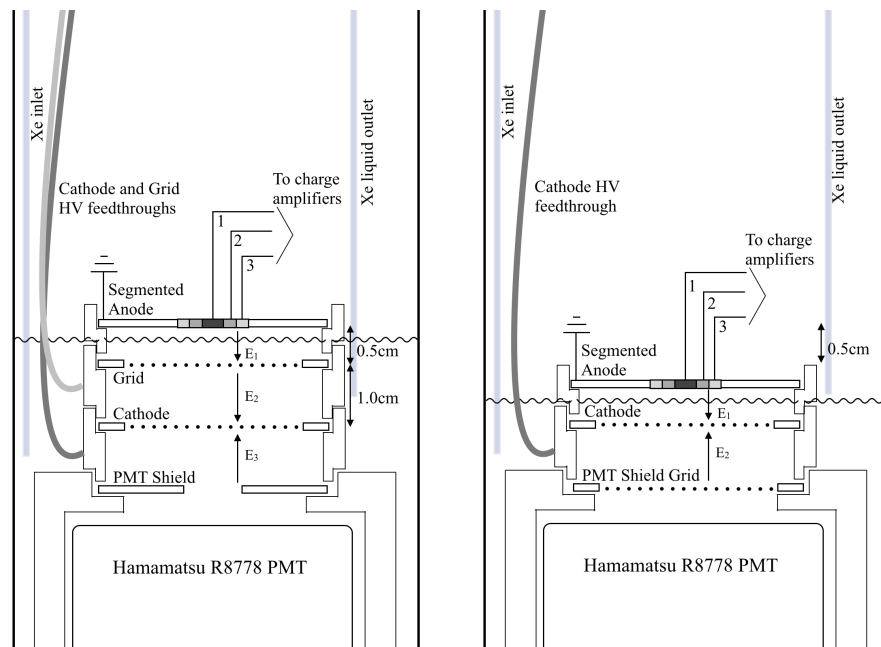


Figure 47: Diagrams of two often used internal arrangements. The configuration (left) has both a drift and extraction region. The configuration (right) is “extraction region only”.

6.2 CIRCULATION SYSTEM

The xenon circulation system is shown in Figure 48. A stainless steel capillary extending into the liquid drew xenon from the inner vessel during operation to be purified. Purified xenon that was returned to the vessel was directed into the liquid via a PTFE tube so it could condense quickly. A gas purge was added to the CF tower above the inner vessel to continually renew the gas column.

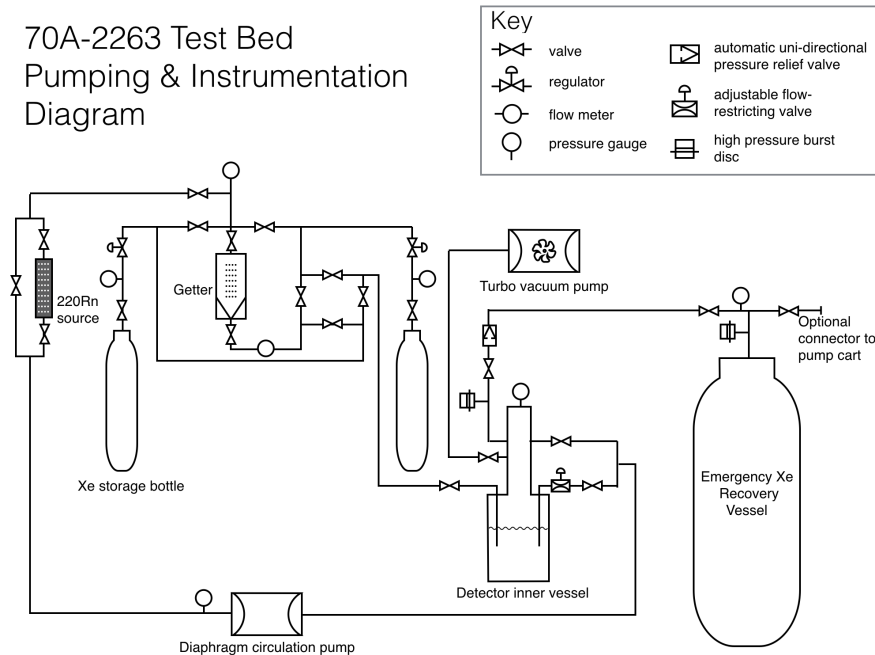


Figure 48: Pumping and instrumentation diagram of the test bed. Special symbols are labelled in the diagram, see key for other symbols. For readability, all gauges are not shown.

6.3 SLOW CONTROL

The slow control for the test bed consists of a few monitoring variables such as temperature and pressure, and a voltage supply that turns on heaters. The inner experimental vessel was instrumented with two platinum RTDs to monitor temperature and a capacitance manometer to monitor pressure. A flow meter in the circulation line determined the flow rate of xenon as it passed through the getter and returned to the inner vessel. These four variables are read using Omega i-series digital panel meters to provide a real-time display; two points of calibration are provided to the digital panel meters to translate voltage to human-readable pressure, tem-

perature, etc. In addition, two $25\ \Omega$ resistors are mounted, in parallel, on the cold-head. Supplying voltage to these resistors raises the temperature of the cold-head and decreases the cooling power delivered by the liquid nitrogen bath; the voltage supplied to the heaters was also recorded, but not shown with digital panel meters. The voltages for the monitoring variables and the heater voltages were fed into a USB Device from Measurement Computing, which interfaces with a computer. A slow control script on a lab computer recorded the monitoring variables and heater voltages. The script also determined if power should be supplied to the heaters and if text message and e-mail alarms should be sent for a variable out of expected range. A basic schematic of the slow control is shown in Figure 49.

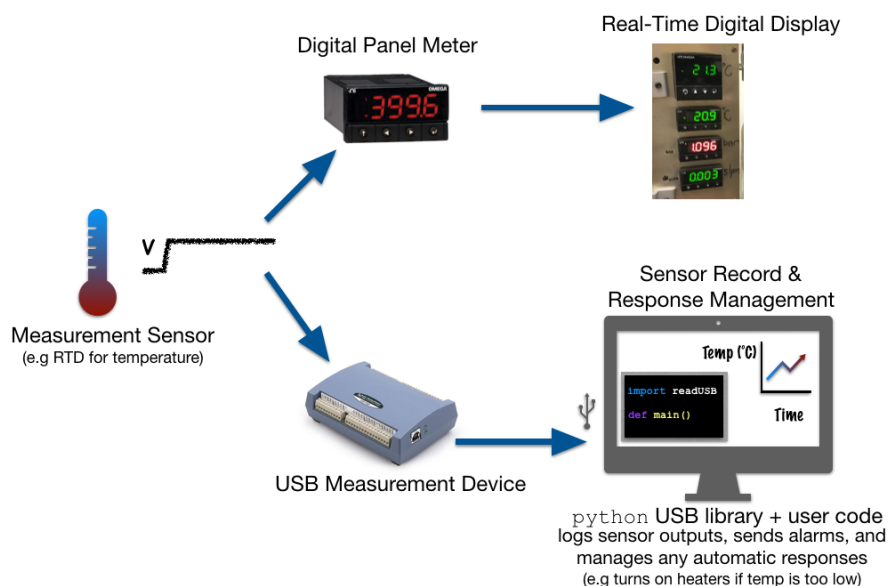


Figure 49: A diagram showing components of the slow control.

6.4 PMT

The test bed was instrumented with an R8778 PMT, the same PMTs used in LUX. Both LUX and LZ PMT bases were used. The radon daughters study presented in Chapter 7 exclusively used the LUX PMT base, the electron trains studies presented in Chapter 8 first used the LUX base, and later used the LZ base. The LZ base was favored for its larger capacitors. Various shaping amplifiers were used when digitizing the PMT over the course of these studies because the 8 ns sampling interval of the data acquisition was subject to aliasing the fast-rising alpha S1 signals.

6.5 CHARGE AMPLIFIERS

The TPC diagram in Figure 47 includes a segmented anode, the largest segment of which is held at ground. The anode is pictured in Figure 50 and relevant dimensions are included in Table 3.



Figure 50: (left) Segmented anode showing the xenon-facing anode segments.
 (right) The wires on the top of the anode which lead to the charge amplifiers.

Anode Segments	1	2	3	Full
Radius (mm)	3	6	9	24
Cumulative Area (mm ²)	28	113	255	1810

Table 3: Dimensions of the of the anode segments. 1 refers to the inner-most segment or “bullseye”, 2 refers to the inner ring, 3 to the outer ring and full to the entire anode, which includes inactive area that is not instrumented with charge amplifiers.

The segmented anode was instrumented with three CR-110 charge amplifiers from Cremat (Figure 51). The raw charge amplifier signals were each fed into a CR-160-R7 shaper evaluation board, also from Cremat. The evaluation board houses two more modules: one CR-200-X shaping amplifier and one CR-110 baseline restorer. The CR-200-X shaping amplifier is an X- μ s gaussian shaping amplifier; it was determined that 1 μ s was most appropriate for the test bed signals.

The shaper evaluation board produced gaussian pulses from raw charge signals as shown in Figure 52.

The charge amplifiers were originally placed inside the experimental vessel, mounted directly on the segmented anode. The functionality in

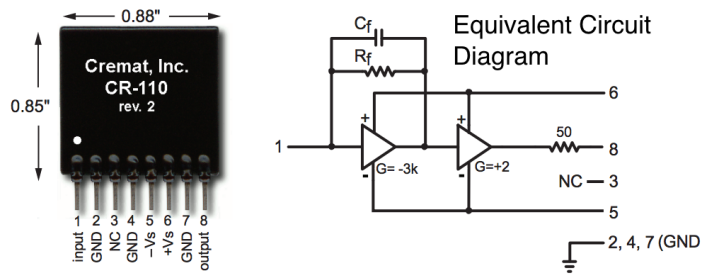


Figure 51: A picture of the CR-110 charge amplifier from the manufacturer's data sheet, shown with an equivalent circuit diagram.

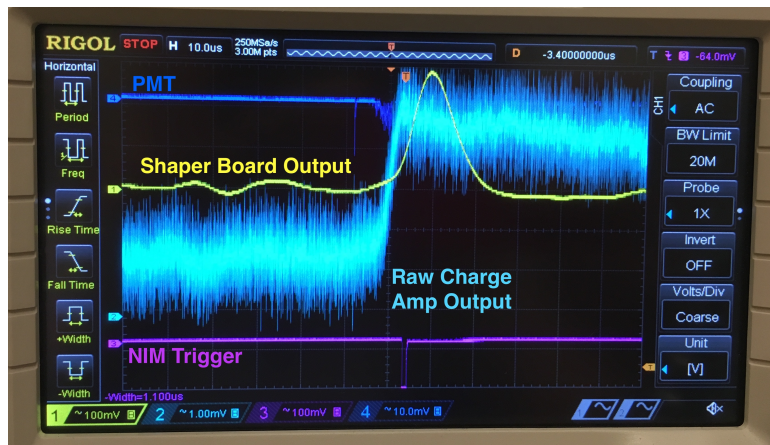


Figure 52: A raw and shaped charge amp signal taken in -100C gaseous xenon, with the radon source plumbed in

[LXe](#) conditions didn't deviate from manufacturer's specifications¹, however it was found that the CR-110 units generated enough heat to create a perpetual gas layer under the anode. In general this is not an issue, but for the purpose of the intended absolute electron extraction efficiency measurement, overfilling the [TPC](#) and using the charge amplifiers as a direct read-out of electrons in the liquid was required. The charge amplifiers were moved to the outer vessel space, surrounded by a small Faraday cage made of copper mesh. See Figure 53 for the charge amplifier mounting configurations.

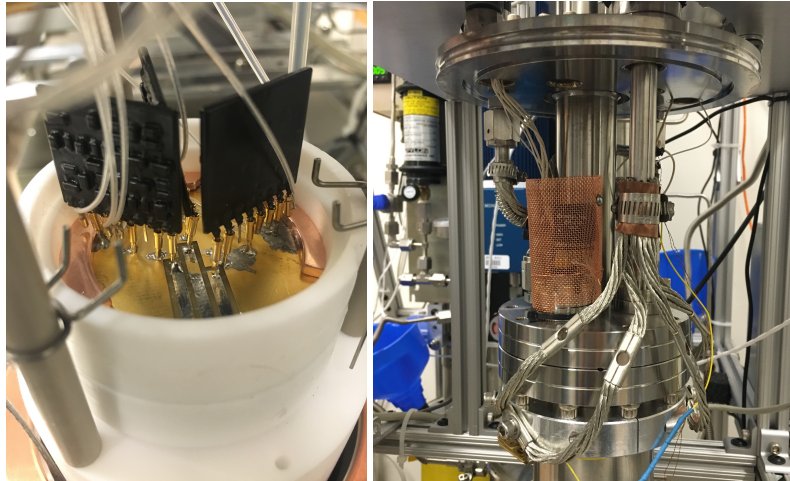


Figure 53: (Left) original mounting of CR-110 charge amplifiers inside the experimental vessel. (Right) Mounting in the outer vacuum reduced heat load on the TPC.

6.5.1 CHARGE AMPLIFIER NOISE BEHAVIOR

Charge amplifiers have baseline RMS noise proportional to the attached capacitance. Figure 54 shows the RMS noise of a CR-110 unit attached to different lengths of BNC cable. The longer the cable, the higher the RMS noise. [TPCs](#) are essentially capacitors, and when filled with [LXe](#) have a higher capacitance than when the detector is at vacuum. The capacitance of large [LXe](#) [TPCs](#) like [LUX](#) prohibit the use of charge amplifiers for direct readout of the S2 electrons because the RMS noise would swamp the signal.

¹ A test was done in a cryogenic fridge to ensure the behavior of the charge amps did not deviate when they were kept at -100 C. There was no change in pulse height (for a fixed input charge), or rise and decay times of the raw signals. This test was not possible in-situ, and so excludes the noise behavior described below, because the manufacturer's test board (CR-150-R5 evaluation board) was necessary to inject charge (via a square wave to an on-board 1 pF capacitor) into the amplifiers.

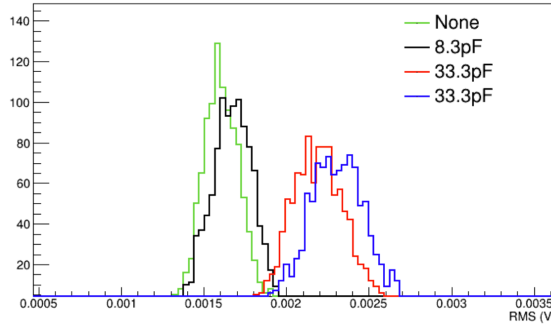


Figure 54: Different lengths of BNC cable attached to a CR-110 test board.

Charge amplifiers also respond to acoustics. Tapping a finger near a charge amplifier will show as a baseline-jumping response on an oscilloscope. This additional source of noise makes [LXe TPCs](#) challenging places to use charge amplifiers for signal readout because any bubbles in the [LXe](#) create micro-acoustic signals which the charge amplifiers pick up. By design, dual phase [LXe TPCs](#) are operated near the xenon liquid-gas boundary so the formation and dissipation of gas bubbles in the liquid is likely. Additional sources of acoustic noise like circulation of xenon into the experimental vessel also produce visible responses in charge amplifiers. The difference in micro-acoustic noise environments (gas phase but with-/without the circulation pump) is illustrated in Figure 55. The baseline restorer can be seen functioning on the gaussian shaped and amplified signals, but the raw charge signals are subject to baseline wandering (Figure 56). Figure 56 was taken in a liquid environment during filling, so the effect of bubbles, pressure changes, and other vibrations are visible.



Figure 55: (Left) Event showing charge amp with detector -100 C, 1.5 bar, gas only. (Middle) Effect of circulation pump on charge amp is to cause 500 Hz oscillation noise (-100 C, 1.5 bar, gas only). (Right) Same event as (middle), but zoomed-in time scale.

As [TPCs](#) are large capacitors, any transients coupling to the “[TPC](#) capacitor” may be picked up by the charge amplifiers. In particular, instabilities in the [HV](#) chain induce a current in the [TPC](#) capacitor that is picked up by the charge amps. Instabilities in [HV](#) can come from many places. It was observed that for the characteristic capacitance and impedance of the the

6.6 DATA ACQUISITION AND PROCESSING

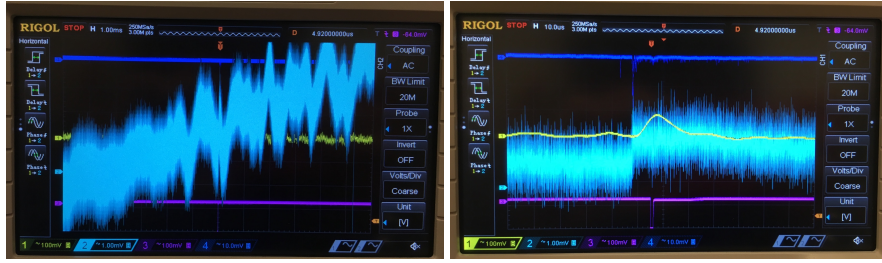


Figure 56: An event with the detector at -100 C, 1.5 bar, with liquid condensed to a level between extraction grid and anode. (left) is a long time trace view the raw and shaped charge amplifier signals. (right) is the same event, but zoomed in. The baseline restorer on the shaped charge signal allowed it to be used as a trigger.

test bed, partial breakdowns in a length of R60 cabling caused a disruption in the functionality of the charge amplifiers. It was also found that a standard laboratory HV supply, a Glassman 20 kV negative polarity unit, created pick-up in the charge amplifiers (see Figure 57).



Figure 57: (Left) Periodic noise from the Glassman 20 kV negative polarity voltage supply. (Right) Partial breakdown in R60 cable as picked up by charge amplifiers.

6.6 DATA ACQUISITION AND PROCESSING

Data were acquired with a Picoscope 5000a, a USB-compatible “oscilloscope.” The open source picoscope Python library was used to write voltage records of PMT and charge signals to ROOT files, which were opened later for reprocessing into reduced quantities such as pulse area or pulse height. The picoscope was run as a 14 bit ADC with 125 MHz (8 ns) sampling. For special cases, when only one channel was desired, it was possible to increase the sampling rate to 500 MHZ (2 ns).

6.6.1 ESTIMATING PICOSCOPE DEAD TIME

Each event was written to disk as it was acquired, which led to large a large dead time percentage. The manufacturer provided no information about dead time, but in general, dead times can be estimated in lab using the following method. Trigger the DAQ externally with, e.g., a square wave. Vary the rate of the external trigger, counting how many events are actually recorded by the DAQ in 1 minute. The number of events actually recorded gives the record rate. The record rate will level off at high external trigger rates because it is limited by transfer speed, write time, etc. Subtracting the actual event length from the real total time it takes to record an event gives the dead time per event. When estimating dead times, use the same conditions in data taking, e.g. if 4 channels are used for real data taking, use 4 channels when measuring the record rate. The dead time per acquisition is then the number of events in the acquisition multiplied by the dead time per event. This method is illustrated in Figure 58. Such a dead time estimate is used in Chapter 7 to calculate the rate in Bq of radon daughters observed.

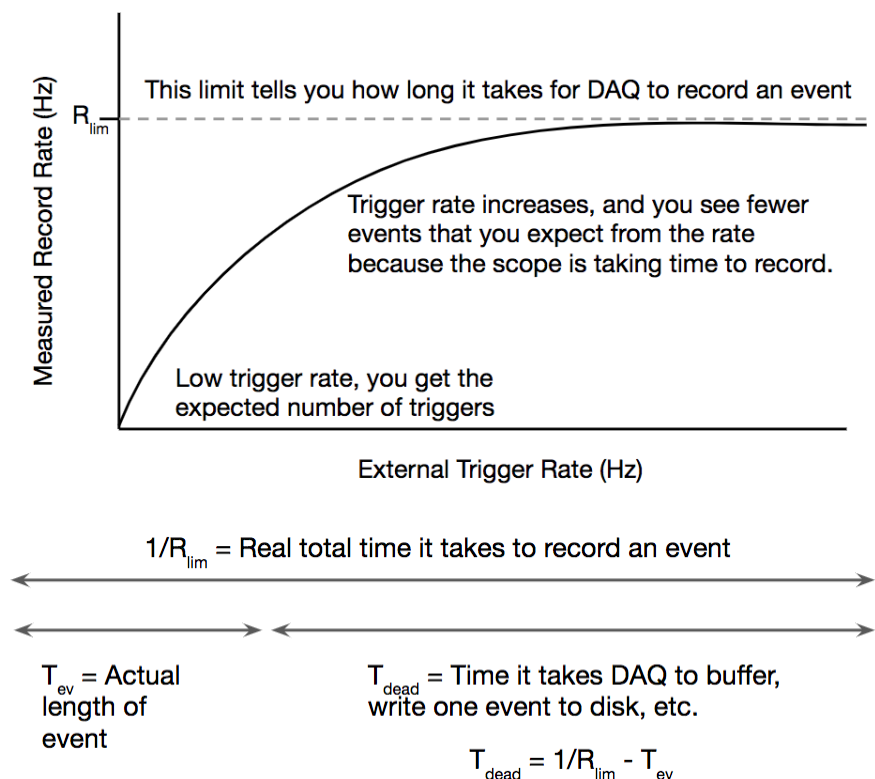


Figure 58: (top) Laboratory method to find the maximum DAQ record time time.
(bottom) Calculating dead time from maximum record rate.

6.6.2 PMT SIGNAL PROCESSING

A simple pulse finder was written in Python. Instead of searching for pulses left-to-right along a signal trace, the algorithm found the maximum of the trace, and then searched left and right until the trace went below a threshold. The trace was set to zero for the duration of the pulse, and then the next pulse was sought. Pulses were found until there were no more, or the number found was equal to some user-defined number of pulses. Thus, pulse starts and stops were acquired for each PMT trace. These pulse starts and stops were then used to calculate useful RQs such as pulse area, width, prompt fraction, etc. S1 and S2 identification was done later, based on these RQs. The definitions of S1, S2, and other high-level PMT RQs often changed because the internals of the test bed were typically changed on a weekly basis during development. A stable data processing framework was not maintained.

6.6.3 CHARGE AMPLIFIER SIGNAL PROCESSING

The shaped charge amplifier signals were used primarily as a trigger throughout the studies in Chapter 7 and Chapter 8. They were originally acquired and implemented because the raw charge signals were small and difficult to process. This was due to field strength, purity, and grid transparency; these issues are described in more detail in Chapter 8, but were all essentially solved by removing the grid to produce an “extraction region only” configuration (Figure 47 (right)). Various methods were explored to process the raw signals into the relevant charge RQ: step height (mV), which could then be translated to charge (Coulombs, then number of electrons) per the manufacturer’s specifications. For small, raw charge signals a fit function was found to out-perform a simple step algorithm; for larger raw signals the step algorithm was fast and robust. Both methods are illustrated below, the fit function in Figure 59 and the step algorithm in Figure 61. The fit function was a piece-wise defined linear function plus a falling exponential. The linear function was defined to be zero before some offset time t_o , and after the offset time plus rise time of the charge trace ($t_o + t_r$). The exponential was zero before $t_o + t_r$, and the two functions had equal values at $t_o + t_r$. The step algorithm produces a new trace with peak instead of a step by averaging $n_{samples}$ of the original charge amp voltage trace from $[i+n_{samples}, i+2n_{samples}]$ and subtracting the average of the waveform from a previous section, $[i, i+n_{samples}]$. If $n_{samples}$ is chosen to be the rise time of the trace, then the maximum of the new trace is equal to the step height. See Figure 60 for examples of two different choices of $n_{samples}$. In practice, the choice is complicated by charge amp noise, and so it was easier instead to find the peak of the new trace

to locate the approximate step position of the original trace, and take the average of several samples as the step height (Figure 61).

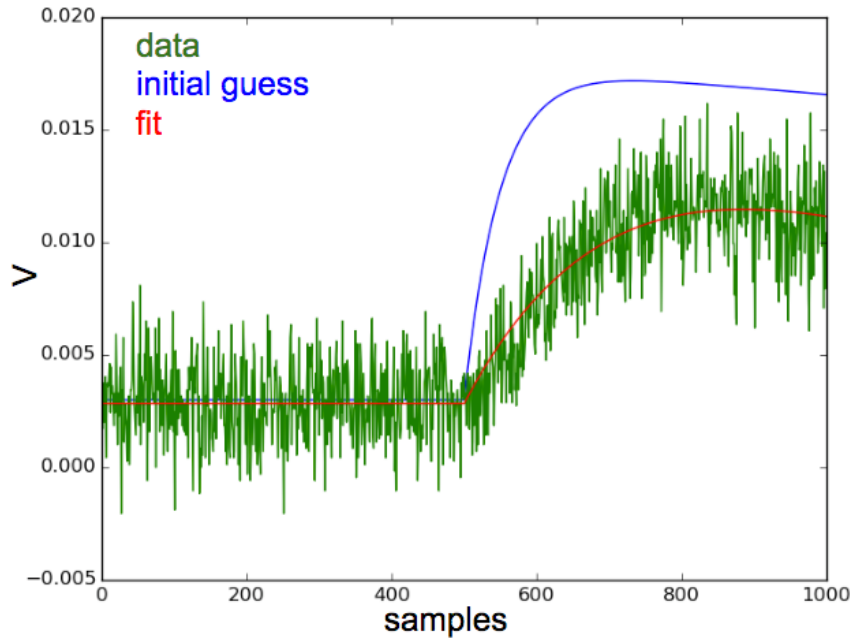


Figure 59: Fitting the charge traces with a piece-wise defined linear rise and exponential fall.

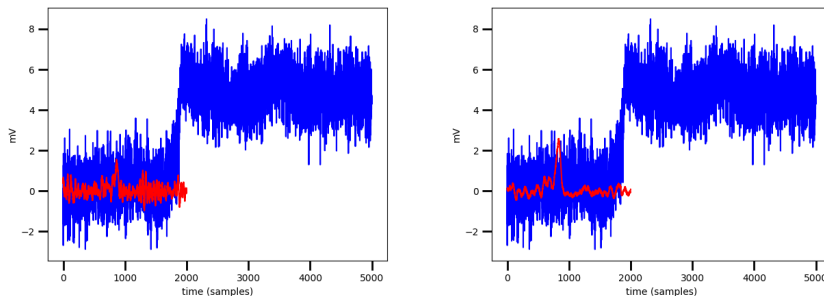


Figure 60: (left) A choice of

For the gaussian shaping amplifiers, the Shockley-Ramo effect is more evident, and can be corrected for by adjusting the maximum for any following dip. Shockley-Ramo effect refers to the Shockley-Ramo theorem, which says the instantaneous current i and charge Q induced on a given electrode due to the motion of a charge is

$$i = q\vec{v} \cdot E_0(\vec{x}) \quad Q = -qV_0((\vec{x})) \quad (45)$$

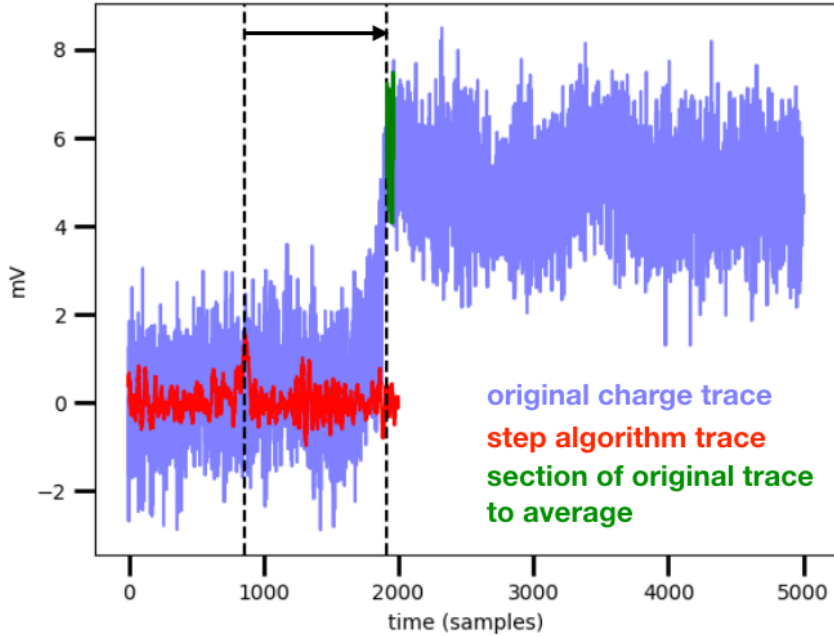


Figure 61

where q is the charge, \vec{v} is the instantaneous velocity of the charge, and $E_0(\vec{x})$ and $V_0((\vec{x}))$ are the electric field and potential that would exist at q 's instantaneous position \vec{x} under the following circumstances: the electrode of interest is at 1 V, all others are at 0 V, and all charges are removed. A helpful review of Shockley-Ramo and a discussion about its effect on charge sensing techniques can be found in [92]. The charge amplifiers are an integrator circuit, and the Shockley-Ramo theorem implies that even if a charge isn't directly underneath a given anode segment, that anode segment has field lines terminating on it as a result of the motion of the charge, and therefore an induced current. When an electron terminates on an anode segment, the other segments “see” the field change and register it as a positive charge, or an electron moving in the opposite direction; the response is a dip in the trace. These dips are present in the raw traces, but in general much less visible and aren't corrected for. In the amplified and gaussian-shaped traces, the dip is more visible, as in Figure 62.

The gains of the gaussian shaping amplifiers were not extensively characterized because they were never used to reconstruct a physical quantity. The shaping amplifiers were used primarily as a trigger because the unit had a baseline restorer, which the raw charge amplifiers did not (see Figure 55 and Figure 56 for the noise conditions on shaped and raw charge amplifiers).

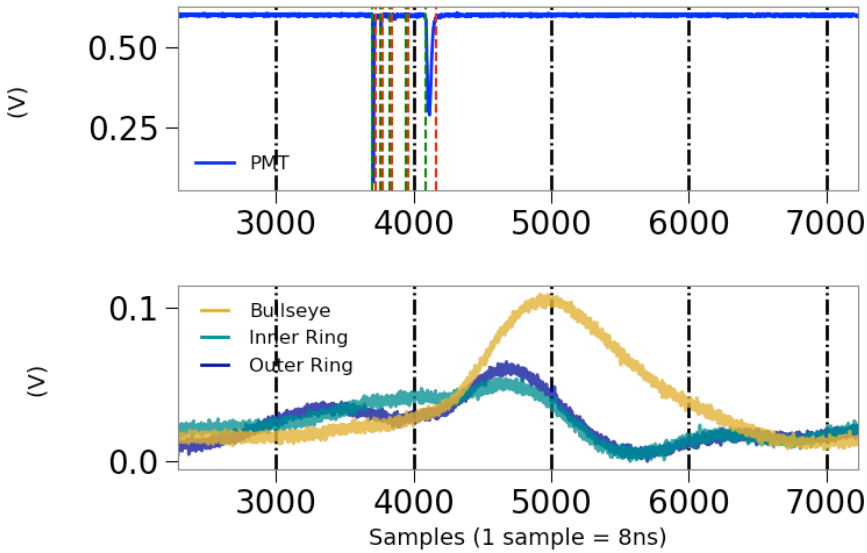


Figure 62: An alpha event showing the Shockley-Ramo effect on the inner and outer ring segments of the anode.

6.7 HIGH VOLTAGE FEEDTHROUGH DESIGN

A significant amount of time was spent developing and testing HV feedthroughs for the test bed. This section describes a few of the feedthroughs that were unsuccessful, leading to the final design, which is capable of delivering -11kV to the cathode with no observable breakdown or other effects. Extensive detail of the tests and procedures are not provided. Instead, the following vignettes are intended as an overview to be useful to a student tasked with designing a HV feedthrough.

6.7.1 OFF THE SHELF FEEDTHROUGHS

The first attempts at building feedthroughs were to use off-the-shelf products from typical vacuum supply vendors such as MDC and Kurt Lesker. Vacuum HV feedthroughs are intended to for use from air to vacuum, not air to LXe; we were attempting to operate them outside of their intended usage parameters. Additionally, by combining ceramic and metal (typically aluminum, stainless steel, nickel, copper) they are especially prone to breakdown at the meeting of these different materials, known colloquially as “triple points”. When there are interfaces between materials with different permittivities (dielectric constants), the electric fields are distorted. Electric field is “pushed” out of the higher dielectric material into the lower dielectric material. This creates a field enhancement where peak fields can be much higher than average fields in the system. The

field enhancement from triple points where there is an interface between a conductor and two dielectrics (e.g. conductor, ceramic insulator, and gaseous Xe) is a common source of breakdown along insulator surfaces. Good design practices, namely choices of geometry, reduce the field enhancements in these regions. With commercial feedthroughs, the geometry choice is set and may not be sufficient for the task.

Note that ceramic feedthroughs are not appropriate for low background experiments due to their high radioactivity, but for test beds, where low radioactivity is not a priority, they may be used.

The first few feed throughs used a 12kV Safe High Voltage (SHV) weldable feed though as shown in Figure 63. If used as operation is intended, the side indicated by A is used on the vacuum-side and B connects to the voltage supply. Instead, we trimmed the long B side and attached a copper, screw-port connector to make the 90 degree connection from vertical feed through to horizontal grid. This was done to avoid placing a conducting surface at high voltage (the tip of side A) in gaseous xenon, thereby increasing the risk of breakdown to the walls of the detector. The feed through's vertical placement is designed such that the copper connector is fully submerged in LXe (Figure ??).

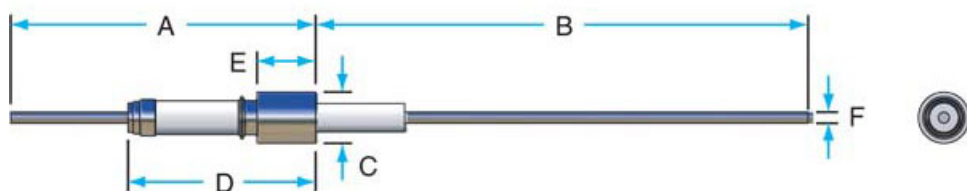


Figure 63: A 12kV SHV weldable connector from vacuum supplier Kurt Lesker.

Feed throughs were tested by performing a cool down, ramping the HV supply slowly, and watching an oscilloscope for a higher than baseline photon rate (Figure 66) or a full xenon breakdown (Figure 67). The effect of raising the voltage on the HV supply at a specific rate was also tested, and it was determined that the extremely slow and steady rate of a computer program was not necessarily superior to the imperfect method of the human experimenter – the construction of the feedthrough, itself, outweighed any gains from computer-supervised voltage ramping.

Iterations of the 12 kV SHV feed though were not able to reach and sustain more than about 7 kV for extended periods of time like those that would be required for data acquisition.

We also tried a stock 20 kV SHV feed through with a custom end cap designed by HV engineer Will Waldron, meant to smooth out typical triple point issues. This feed through was mounted on a CF flange far from the



Figure 64: (left) The copper tape in this picture is sitting on top of a 1/2 -in swage connector. The swage connector captures a 1/2 in pipe, which has the 12 kV SHV feedthrough welded to the end. (right) 12 kV SHV weldable connector, inverted, clipped, and attached with a machined copper connector. The connector uses a screw to capture the SHV feed though, and the same screw to capture a stranded wire, visible in this picture, which is then fed through a hole drilled in the PTFE to connect to the wire grid frames. The wire was wrapped around the grid frame.

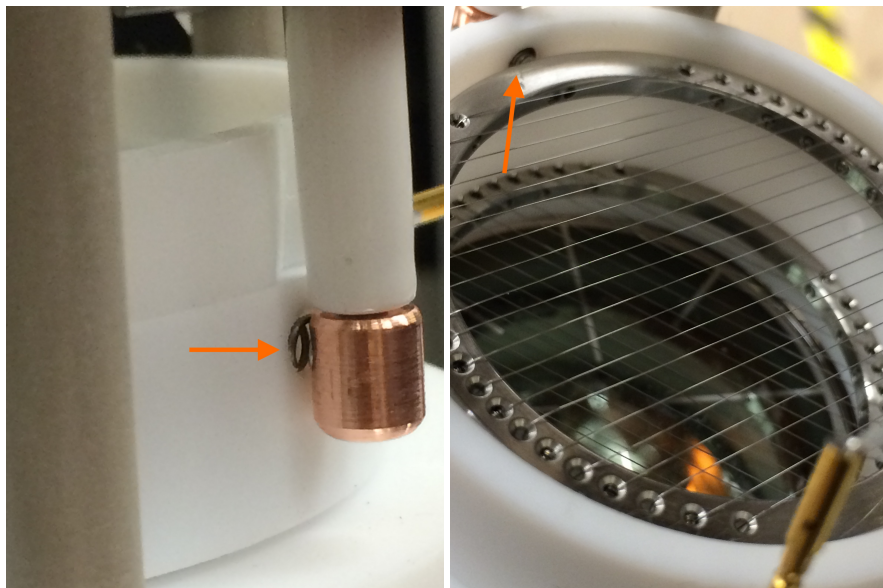


Figure 65: The same 12kV SHV feed through, now with a modified spring connection connecting the feed through to the grid frame. A close up of the cathode grid showing the spring connection is on the **right**

6.7 HIGH VOLTAGE FEEDTHROUGH DESIGN

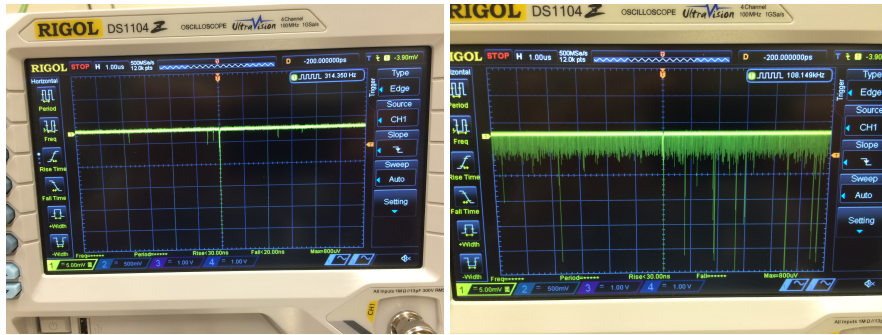


Figure 66: Oscilloscope showing baseline rate of single photons (left) compared to a high rate of single photons (right) caused by the high voltage feed through.

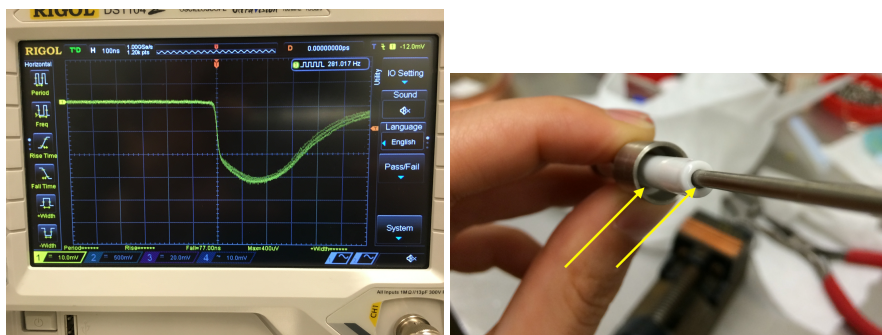


Figure 67: (Left) Full xenon breakdown as visible on the PMT trace. The large, saturated pulse is caused by the high intensity of light. This type of breakdown was often accompanied by an audible buzz, and a rise in current that would initiate a trip of the high voltage supply. (Right) a close up of the xenon-facing side of the feedthrough. Visible gaps where xenon gas is exposed to high fields are particularly problematic for breakdowns.

active region. A length of cable was stripped of grounding sheath for its entire length. A small section on one end was stripped of dielectric, this end was tied to the SHV feed though with copper wire, and the custom end cap was placed over this. The side of the cable making the connection to the cathode grid was drilled out for a short length on the bottom, leaving only a tube of dielectric with no conductor. A threaded rod was inserted into the cable, such that the rod made contact with the conductor. The cathode grid frame was screwed onto the threaded rod. The SHV-20 feed though is summarized in pictures in Figure 68, and was found to hold sufficient voltage (10 kV) for extended periods of time. However, it was found that the voltage capability of this feed though decreased over time; this is discussed in the next section.

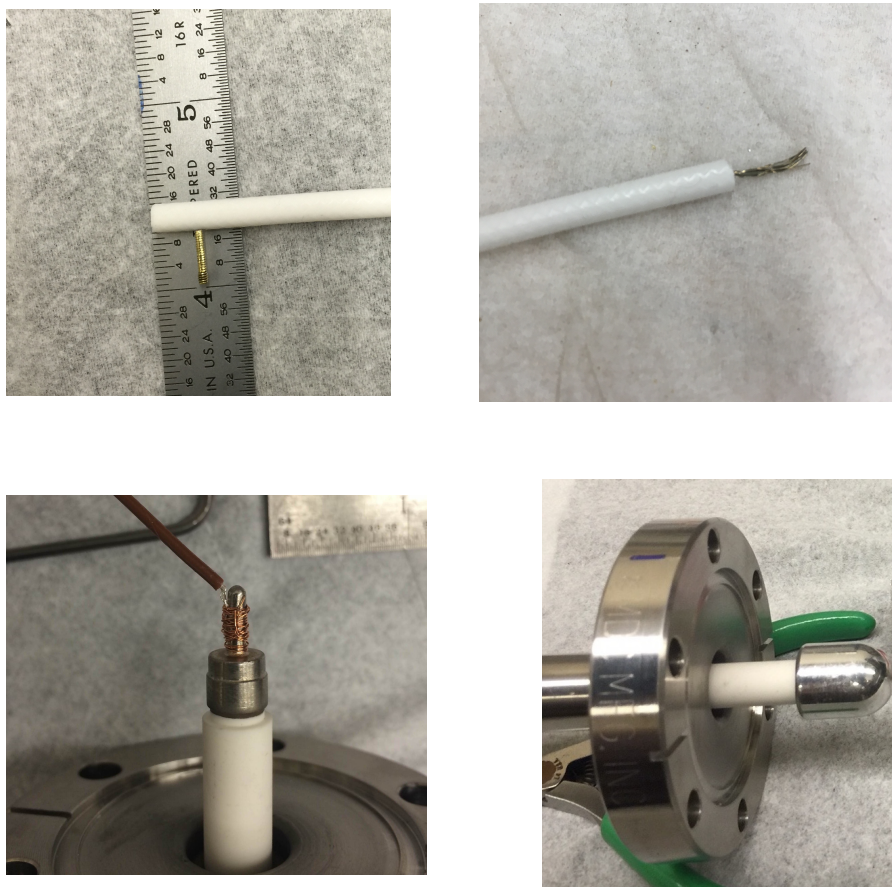


Figure 68: Top: (left) cathode connection side (right) SHV-20 connection side
Bottom: (left) an example showing how the cable was attached to the stock SHV-20 feed though end (right) a custom cap fit over the connection, smoothing out triple points.



Figure 69: Effect of holding the feed through in place with PEEK zip ties was explored, effects were minimal.

6.7.1 FEEDTHROUGH AGING

It was noticed during subsequent operation that the SHV-20 feed through was subject to some sort of aging process (black line in Figure 70). A month of use resulted in noticeably lower voltage capabilities. The issue could have been any point along the entire voltage chain: feed through - custom cap - connection to cable - cable - connection to grid - grid. Tests focusing on different parts of the voltage chain didn't reveal any weak points. Instead, it was found that the SHV-20 feed though, itself, was subject to aging (red line in Figure 70).

Feedthrough aging can be the result of arcing and discharges which cause local heating and carbonization of an insulator surface. Once there is a carbon path, the insulator is considered "tracked" and then holds a much lower voltage than before. Sophisticated HV systems keep peak currents and fault energies to a minimum using series resistors. In this way, a breakdown event does not degrade system performance in the future. In addition to carbon tracks, there can also be insulator degradation from exposure to UV if there is ionization in the region. Xenon ionization is in the UV region of the spectrum, and so any ionization near a feed though insulator may degrade the feed through performance. In the case of this particular feed though, the high field which caused the breakdowns or ionization was likely a result of poor triple-point geometry.

6.7.2 CUSTOM FEEDTHROUGHS

To achieve better voltage performance, we moved away from typical, stock feedthroughs composed of ceramic and metal. Figure 71 shows a feed through made with a Swagelock reducing union. This blue and white PTFE piece connects 1/4 in SS pipe to an 1/8 in PTFE tube, which then

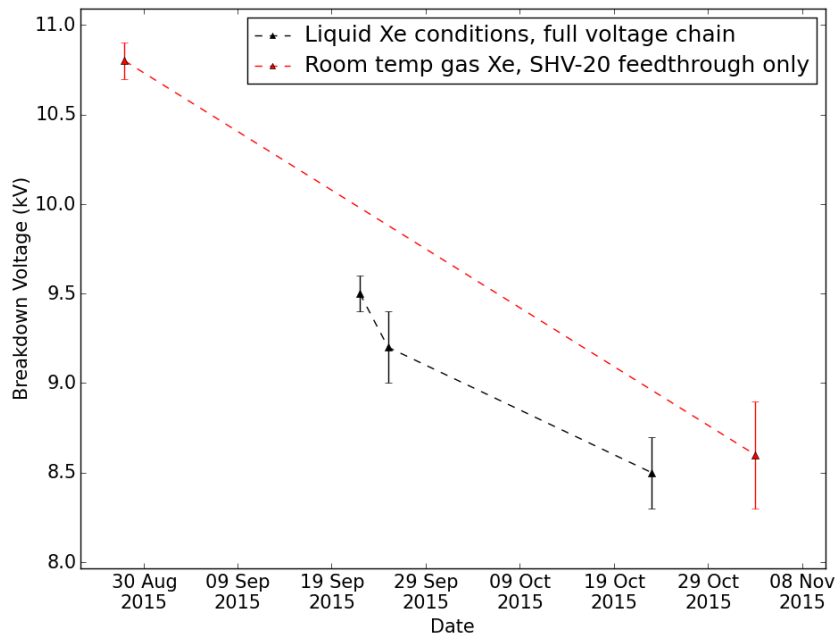


Figure 70: The black line shows the aging observed in the course of normal operations. The red line shows breakdown tests of the SHV-20 feed through in gas, illustrating that the aging observed during operation was due to aging of the feed though.

houses a [SS](#) rod. The rod is screwed onto a connector, which holds a wire to connect to the grid. This feed through had stable voltage performance, but could not achieve sustained voltages higher than about 9 kV. A woven [SS](#) shield was added to the feed though to reach higher voltages (Figure 71 (left)) but this actually decreased the voltage performance to a maximum of about 5 kV.



Figure 71: First attempt at a custom feed through built out of Swagelock parts combined with basic materials like [PTFE](#) and stainless steel rods. The orientation shown (left) was later inverted due to concerns of temperature stress and pressure stress on the [PTFE](#) ferrules. The feedthrough as assembled (center) was functional, but higher voltage capability was desired. The effect of adding a grounding braid (right) was found to decrease the voltage capability instead of increasing it.

There are two issues with the approach of adding a grounding braid in this method: (1) the braid is not tight to the dielectric, which introduces peak fields between the dielectric and the braid (Figure 72) (2) at the braid termination, a small effective radius creates an enhanced radial field through the dielectric and an enhanced field along the cable dielectric facing the high voltage. Peak fields can occur in unexpected places, greatly decreasing the voltage capability of a feedthrough that seems, naively, robust. The breakdown field of xenon gas depends on a variety of factors such as temperature (i.e density), purity, electrode shape, etc. Peak fields arising in gas regions in or around [HV](#) feedthroughs are sources of unwanted light and in the worst case complete breakdown and eventual degradation of the feedthrough.

Due to the poor performance of custom feedthrough, and concerns about the cold connection, a feedthrough was built out of a [SS](#) rod with [PTFE](#) dielectric and no shield braid (Figure 73) that enters the inner vessel from the top of tall CF tower, where the connection is warm. The end is a copper rod bent into a U-shape which connects to the [SS](#) conduction rod via a pin, and the other end, which is threaded, screws into to the cathode grid frame. The bare copper section is only exposed under the liquid level, elsewhere the [PTFE](#) dielectric helps contain the electric field and prevent breakdown to the inner vessel wall. This feedthrough had

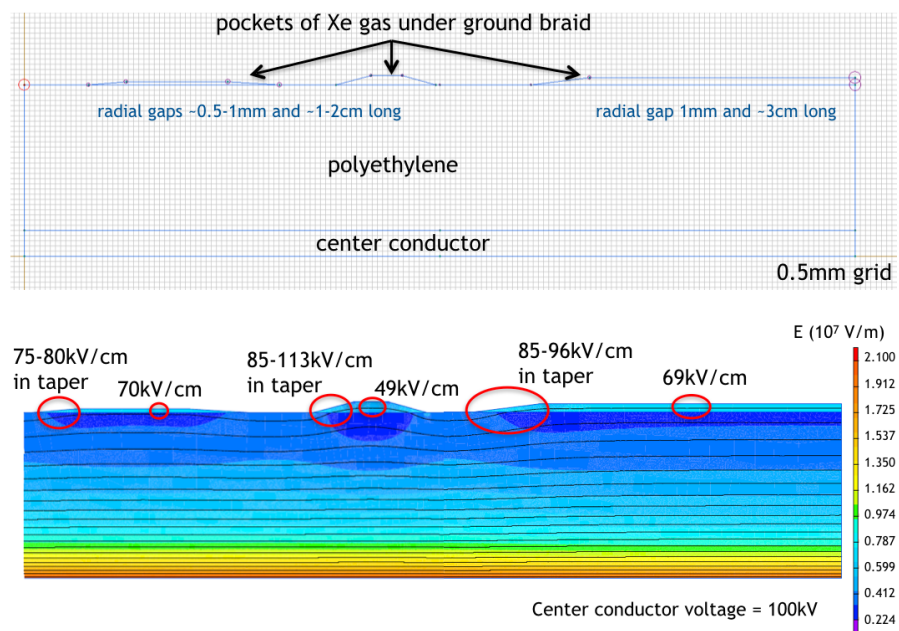


Figure 72: (top) Input to a COMSOL model simulating gaps between the grounding braid and dielectric of a high voltage feedthrough. (bottom) COMSOL output of the model, showing that peak fields arise when gaps exist between dielectric and grounding braid. Both images provided by W. Waldron.

good voltage performance, and there was no sign of aging. It was decided, however, that the charge amplifiers were more susceptible to detecting transients from an unshielded feedthrough, so another feedthrough with shielding was constructed (Figure 74). This feedthrough has an outer PTFE sheath to keep the shielding tight against the inner dielectric. This final feedthrough design was extremely successful, and has been in use for 2 years at the time of writing this thesis.

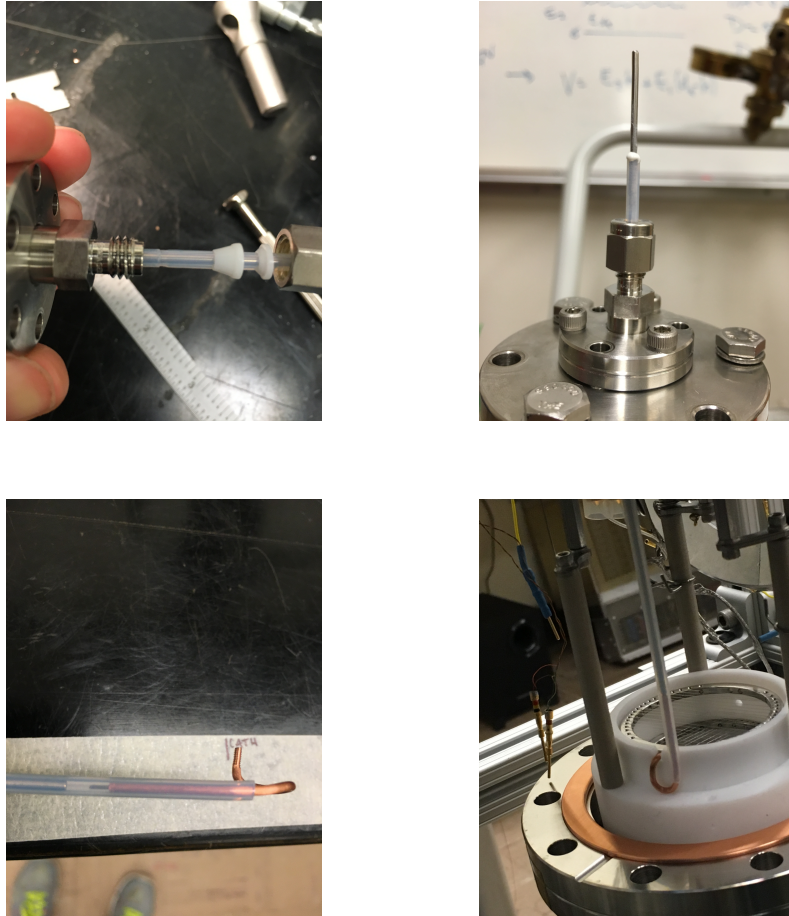


Figure 73: Top: (left) Close up showing the PTFE ferrules and notch. (right) Close up of the sealed top connection; epoxy was added to prevent leaks between the dielectric and conductor rod . Bottom: (left) Threaded U-bend cathode connector (right) Feed through assembled and installed.

6.8 ELECTRIC FIELDS IN TEST BED

Both peak fields, which occur on the grid wires, and fields at the liquid-gas boundary are important to understand. Peak fields are often at a “weak link” in the voltage chain where breakdown is most likely to occur. The field in the liquid near the gas boundary extracts electrons, making it im-



Figure 74: Top: (left) Sealed top connection with liberal epoxy use. A male Bendix pin was soldered to the cable conductor. (middle) SHV connector with female Bendix to mate with feedthrough (right) Grounded safety housing with SHV connector. Bottom: (left) Ends of the feedthrough were held in the Teflon stack. (middle) Close up showing cable conductor, PTFE dielectric, and grounding sheath pulled back (right) Grounding scheme for feedthrough cables.

portant for TPC function. The electric field changes as a function of liquid height, and can be calculated analytically following the McDonald lecture notes [93]. A COMSOL model with the test bed geometry and materials was also developed by E. Mizrachi, and the analytic calculation was found to agree. Figure 75 provides a summary of the electric fields on the grids wires for a case where there is only a cathode and anode, separated by 5 cm. The color scale on the COMSOL is misleading, The peak fields, which occur on the cathode wires, are ~ 130 kV/cm, which appears the same color as 20 kV/cm.

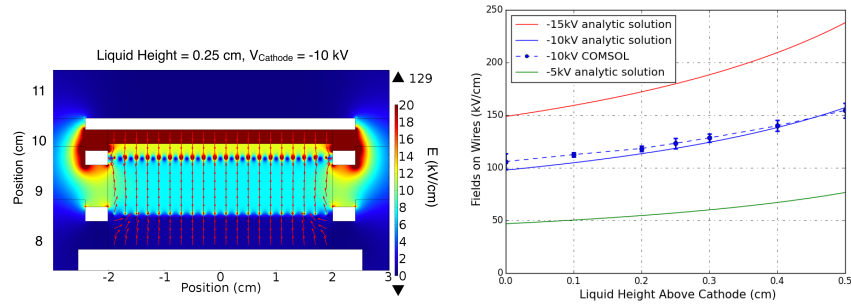


Figure 75: (left) COMSOL model with specific cathode voltage and liquid level. (right) Analytic calculation following the McDonald notes [93], which shows how the peak fields vary with change in liquid level and cathode voltage. The voltages in the legend refer to the cathode voltage; the anode is held at ground.

The COMSOL model shows that the fields in the liquid and gas do not vary very much with position, once there is sufficient distance from the wires. The fields do, however, vary with liquid level. Figure 76 shows how the liquid and gas electric fields vary with liquid level and cathode voltage; the TPC configuration is cathode and anode only, separated by 0.5 cm. The calculation is straightforward: the TPC is a essentially a capacitor with a dielectric. Cathode and anode provide boundary conditions on the voltage, and continuity of the derivatives at the liquid-gas boundary is the remaining boundary condition to solve Poisson's equation.

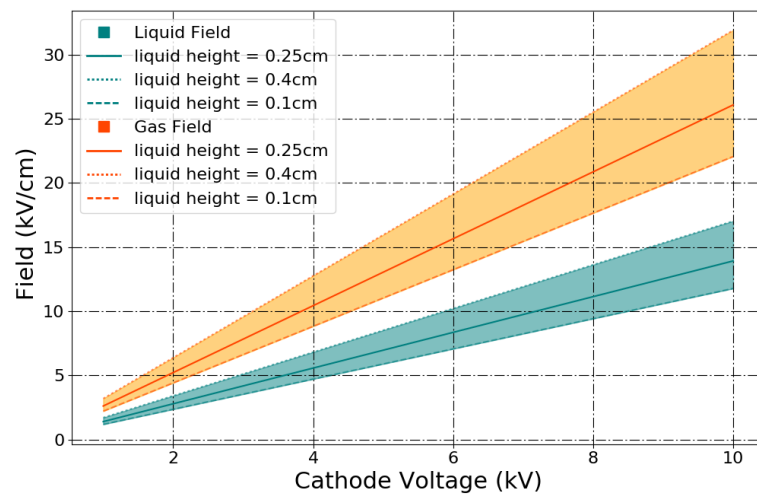


Figure 76: Ranges for the electric fields in gas and liquid for different cathode voltages and liquid levels.

7

SOLUBILITY OF RADON DAUGHTERS IN LIQUID XENON

Rare-event searches are very sensitive to backgrounds from radioactivity in and on detector materials. Some of the most omnipresent and troublesome are ^{222}Rn and its daughters. Decay products from ^{222}Rn plate out on detector surfaces and have typically been assumed to be fixed there. In this chapter, a series of experiments is described; the results provide evidence that radon daughters can dissolve in liquid xenon.

7.1 MOTIVATION

Radon and radon daughters produce problematic backgrounds for rare-event searches [67]. Of particular concern for liquid xenon dark matter detectors are “naked” beta decays. These ground-state to ground-state decays have no accompanying gammas and cannot be rejected via coincidence tagging. Rejection of these backgrounds in WIMP search experiments relies solely on being able to discriminate electron recoils from nuclear recoils. For example, the ER leakage fraction from the LUX Run03 tritium calibration is on the order of 2/1000 over the WIMP search region [**LUX:Tritium**] (See Chapter ?? for more details). The ^{222}Rn chain contains ^{210}Pb ($T_{1/2} = 22.23\text{ y}$), effectively splitting the decay chain into a “fast chain” and “slow chain” (Fig. 77). Radon can be introduced via two pathways: (1) during detector construction and (2) during detector operation (see Fig. 78). Great care is taken to ensure minimal contamination via pathway 2 because the fast chain naked betas, ^{214}Pb and ^{214}Bi , may decay in the fiducial volume before the purification system can remove them or before they can plate out on detector surfaces. In pathway 1, ^{222}Rn and daughters plate out onto detector surfaces during construction of parts, and construction of the detector itself. Models for plate out can be found in [94] and [95]. Typically it is assumed that once ^{222}Rn and daughters plate out, they remain fixed at that position, and can be rejected by a fiducial volume cut. This means that the slow chain naked betas of ^{210}Pb and ^{210}Bi from initial exposure during construction are assumed to occur outside the fiducial volume. However, evidence of ^{210}Bi mobility has been

observed in the liquid scintillator environment of KamLAND [96], [97] and Borexino [98]. If radon daughters are soluble in liquid xenon, the late chain naked betas (from both pathway 1 and 2) pose a serious background distributed throughout the fiducial volume.

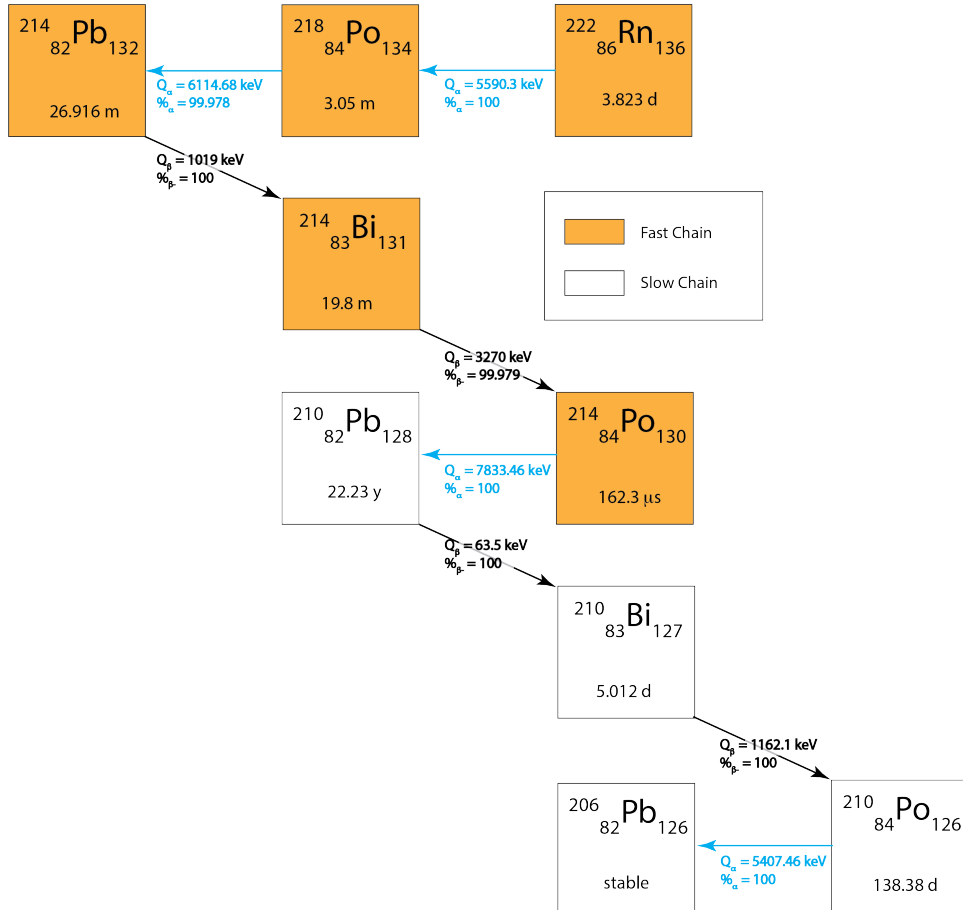


Figure 77: The ^{222}Rn decay scheme. The fast and slow chains are indicated.

In order to investigate the solubility of radon daughters in liquid xenon, a ^{220}Rn source was employed. The analogous long lived daughter in this chain, ^{212}Pb , has a half-life of 10.6 h, making it appropriate for a laboratory test. Investigating pathway 2 in the laboratory by introducing radon in a LXe environment will necessarily yield inconclusive results, because it is impossible to tell if the daughter decay of interest plated out before decaying. Therefore, we required the radon daughters to be on a surface.

Xenon gas was circulated through the ^{220}Rn source and detector components for a period of >24 h. The detector was then evacuated, thereby assuring the initial position of radon daughters on a detector surface. Any radon daughters subsequently observed in the bulk region after condensing liquid xenon must therefore have dissolved.

Pathways to Radon and Radon Daughters Contamination

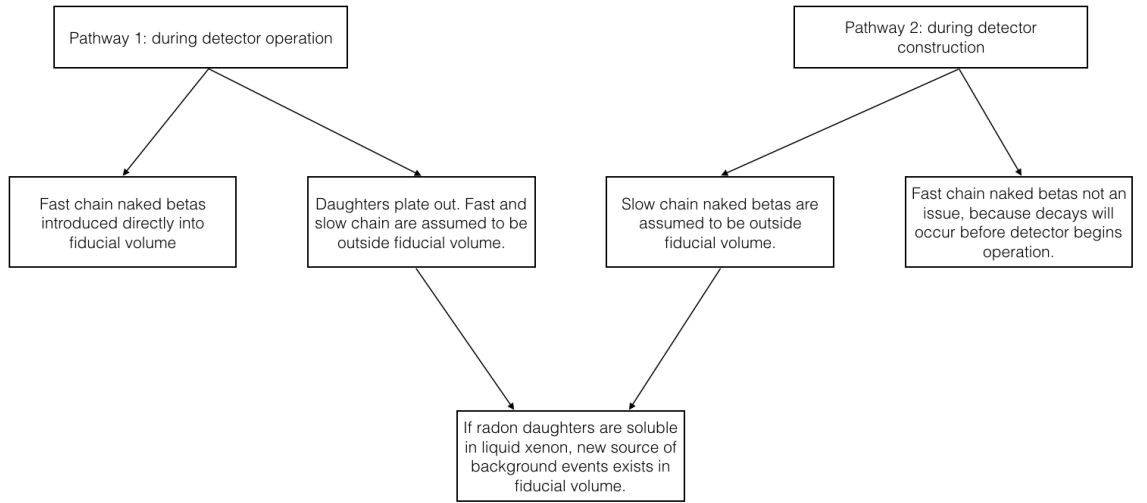


Figure 78: Pathways to radon and radon daughter contamination.

7.1.1 PLATE OUT

The term “plate out” is used above but not defined. The literature indicates that there two known types of radon daughter plate out [99]. The following terms are used in [99] to identify each type.

1. *implantation* Alpha recoil implantation of a daughter nucleus
2. *sticking* Daughters are sitting on the surface of a material, it is possible to wash a percentage of these off with various surface cleaning methods.

The percentages of daughters plated out in these different modes are not indicated, but [99] relates a story of researchers being unable to remove ^{214}Po from glass samples, where as ^{218}Po was easily removed with surface cleaning methods. This is explained by the fact that further down the ^{222}Rn chain, more alpha decays have occurred, so a late-state daughter has had more chance to be implanted. It is also noted that the durability of the implanted activity subject to change under different conditions, as is the implant integrity. The author cites factors such as humidity and temperature affecting whether daughters implant, and whether they remain implanted; since the conditions for plate out are different in pathways 1 and 2 and it logical to infer that implantation functions differently in these two environments for LXe TPCs.

The chemistry of radon has been studied as well, and may provide some context to the plate-out discussion. Radon is frequently regarded as a totally inert element. It is, however, classified as a “metalloid”, and exhibits some of the characteristics of both true metals and nonmetals. For example, it is known to react chemically with fluorine, halogen fluorides, dioxygenyl salts, fluoro-nitrogen salts, and halogen fluoride-metal fluoride complexes to form ionic compounds [100]. It is also known to co-crystallize with hydrogen chloride, hydrogen sulfide, sulfur dioxide and carbon dioxide [101]. In the latter case, the author notes that the radon is not forming true chemical bonds, but rather is held in place by weak Van der Waals forces. These chemical experiments found radon to be readily reactive at “room temperature and lower”, but the low temperate range is not stated. Chemical bonds formed by radon may make up a different type of plate out, or sub-type of ‘sticking’. Presumably weak surface Van der Waals forces belong in the ‘sticking’ type as well.

If we look to surface physics, the plate-out term ‘sticking’ is well defined by the terms physisorption and chemisorption. Physisorption is distinct from chemisorption in that it is a general phenomenon occurring between the adsorbed atom and surface, where chemisorption involves a chemical reaction between surface and adsorbate, and is characterized by higher bond strengths. Chemisorption potentials have been calculated for many atoms and surfaces [102] and are generally greater than 1 eV. Physisorption potentials, such as the well-known Van der Waals potential, are less than 1 eV and as low as 10 meV.

Plate out occurs with different rates on different materials [103], and can be an order of magnitude larger on PTFE than stainless steel, likely due to PTFE’s tendency to accumulate negative static charge [104]. Plate out of radon daughters can be reduced by employing a nitrogen gas purge or an electric field (approximately 90% of radon daughters are charged) [105]. However, [103], [104], and [105] do not distinguish between implantation and sticking, and only use the term “plate out”.

7.2 EXPERIMENTAL CONFIGURATION AND METHOD

A diagram of the TPC for this work is shown in Fig. 79. A 50 mm diameter cathode wire grid, extraction wire grid, and a planar, segmented anode were held in Teflon PTFE housing. The anode was instrumented with charge-sensitive preamplifiers. Both grids were constructed from a stainless steel frame strung with 4 μm diameter stainless steel wire on a 2 mm pitch. The xenon inlet was a PTFE tube which introduced xenon gas into the liquid region where it was condensed. The xenon liquid outlet was a thin stainless steel capillary that drew liquid from the TPC into the

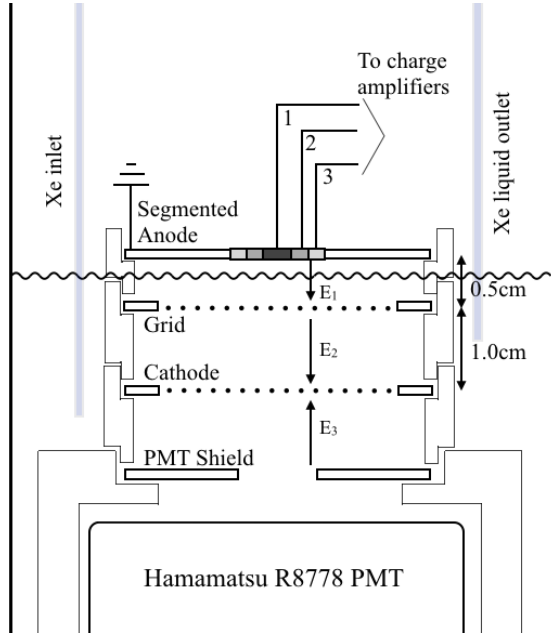


Figure 79: Diagram of the test bed. For this study, the cathode is held at -6.0 kV, and the grid is held at -4.0 kV. $E_1^{liq} \approx 5.0$ kV/cm, $E_1^{gas} \approx 10.0$ kV/cm $E_2 = 1.0$ kV/cm. $E_3 = 2.7$ kV/cm. The large gray regions represent the structural rings of PTFE. The line between the grid and anode represents the liquid xenon level. The xenon inlet pipes incoming gas directly into the liquid region, and the liquid outlet pulls from the level of the active region. A gas outlet (not pictured) also draws xenon gas into the circulation system to be purified.

purification system. Both inlet and outlet tubes were placed near holes drilled in the PTFE to aid circulation into the active volume.

A particle interaction in the liquid xenon volume produced primary scintillation photons (S1) and ionization electrons. The ionization electrons were drifted with an electric field into the gas phase, where they produced secondary scintillation light (S2). A single Hamamatsu R8778 VUV-sensitive PMT was installed in Teflon PTFE housing, facing upward to view the active region. Directly above the PMT was a copper shield mask, held at the same voltage as the PMT bias of -1250 V.

The TPC was filled with 1.5 bar of xenon gas at room temperature. The gas was circulated continuously through the TPC and a heated zirconium getter for at least 24 hours to remove contaminants. The TPC was then cooled to -100° C while circulating xenon gas. Circulation was stopped, and xenon was condensed into the TPC until the liquid level rose to between the extraction grid and anode. The process of filling the TPC took 4 to 5 hours. The liquid level was kept stable by keeping the temperature and pressure constant in the TPC. During data collection, xenon from the

TPC was circulated through a getter and re-condensed into the TPC to remove impurities.

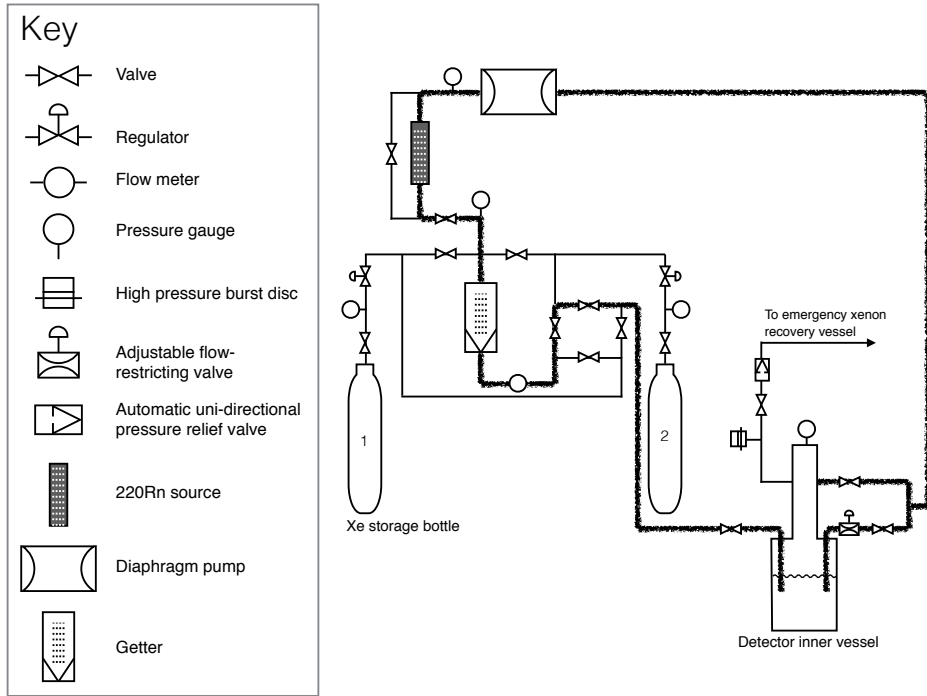


Figure 80: An example a circulation path used for plate out is shown on the pumping and instrumentation diagram. During data-taking the radon source was bypassed. The typical liquid level is indicated on the diagram to show that the outlet drew from the liquid via a capillary, ensuring purification of the liquid xenon. A gas purge also purified the gas column in the detector.

7.2.1 PLATE OUT OF ^{220}Rn DAUGHTERS

The procedure to plate out ^{220}Rn daughters on the inner surfaces of the detector was the same as described in Sec. ??, except that the circulation path was directed through a 2 kBq ^{220}Rn source. The ^{220}Rn is shown in Fig. 81. The rate of radon activity in the TPC was measured to be 4.5 ± 0.5 Hz during plate out. The total alpha rate was measured by taking repeated 1200 ms traces on an oscilloscope of the PMT with a falling edge trigger and counting the alpha decays. This rate was then halved to get the rate of radon decays. The 4.5 ± 0.5 Hz rate of radon activity represents activity for all of the space internal to the PTFE support structure. Decay daughters diffused until they contacted a wall or other surface, where they could plate out. Some percentage of decay daughters are expected to be positively charged ions. If the cathode grid was biased, charged decay

daughters drifted preferentially to the cathode grid. The cathode voltage during plate outs is noted in Table 4.

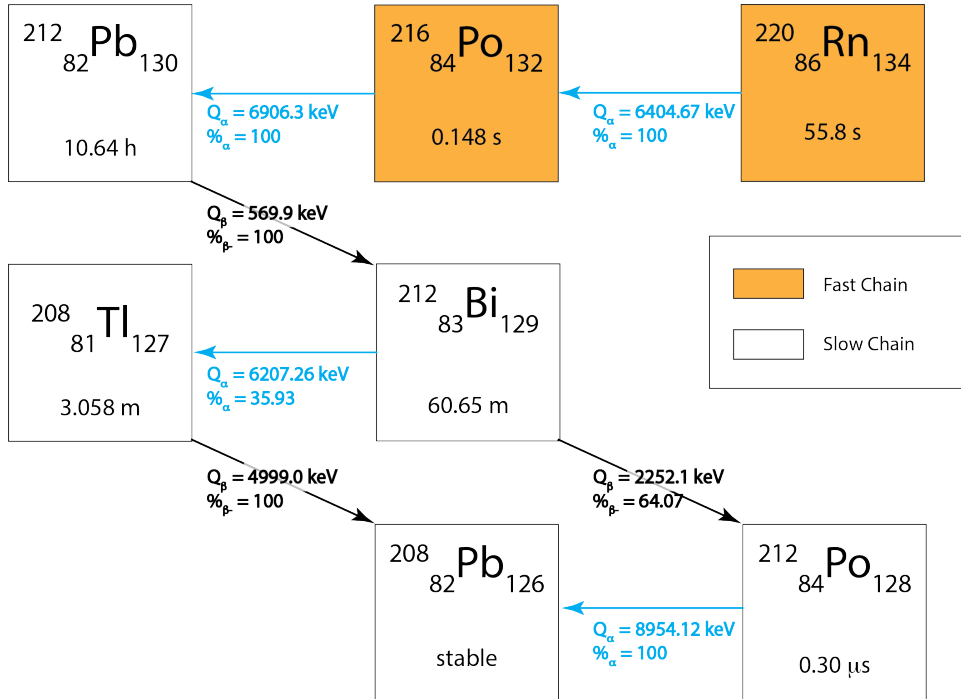


Figure 81: The ^{220}Rn decay scheme. The fast and slow chains are indicated. Events in the plate out data sets are from the slow chain.

Prior to filling the TPC with liquid xenon, the circulation was stopped and the xenon gas removed from the TPC and the circulation lines. A vacuum pressure of a few 10^{-4} Torr was achieved in a period of ten minutes. This step ensured removal of ^{220}Rn and decay daughters which are dissolved in the gas, leaving only those daughters which had plated out on a detector surface. Since the fill time of the TPC is 4 to 5 hours, there were no fast chain alpha decays of ^{220}Rn and ^{216}Po in the plate out data. Additional details are summarized in Table 4.

7.2.2 DATA COLLECTION

Voltage records from PMT and charge channels were collected with a 14-bit ADC with 125 MHz sampling and a 20 MHz low-pass filter. The trigger was a coincidence between the PMT and the central anode segment, used to select events in the central ($r < 3$ mm) column of xenon. This avoids any electric field fringing effects.

	dataset ID	A	B	C	D
Plate-Out	Circ thur ^{220}Rn Source	yes	yes	no	-
	Circulation Time (h)	24	48	24	-
	Cathode Voltage (kV)	-1	0	0	-
Data-Taking	Circ thur ^{220}Rn Source	no	no	no	yes
	Cathode Voltage (kV)	-6	-6	-6	-6
	Grid Voltage (kV)	-4	-4	-4	-4
Livetime (h)		12.02 ± 0.5	23.93 ± 0.5	25.02 ± 0.2	4.15 ± 0.2

Table 4: Summary of plate out and data-taking conditions. Data sets A and B are taken after circulating radon gas and data set C, background, had no radon circulation. Data set D was taken following dataset A, and radon was circulated in a liquid xenon environment, purposefully introducing radon into the detector bulk to calibrate the detector.

7.2.3 CALIBRATION

In order to identify a signal region for bulk radon daughters, the flow through ^{220}Rn source was employed directly following dataset A, allowing ^{220}Rn to flow into the liquid bulk of the TPC. The bulk daughter decay of interest, ^{212}Bi alpha, has an energy approximately equal to the ^{220}Rn alpha decay. The alpha signals were sufficient to saturate the biasing circuit of the PMT, so alpha decays within 1 MeV of each other were indistinguishable. Therefore, the region in S1 area vs. S2 area where the ^{220}Rn alphas appeared was also where ^{212}Bi alphas were expected (Fig. 86).

7.2.4 POSITION RECONSTRUCTION

The central anode segment was assumed to select events from the central column with 100% efficiency. Events occurring under one of the outer concentric segments can produce a signal on the central anode, but the signal was largest at the anode nearest the charge. It was not required that there be zero signal on the outer segments, so the (x,y) position of the event is treated as a source of uncertainty, which is taken into account in the calculation of fiducial volume. The drift time of the events was

calculated from the time difference between the S1 and S2 pulses, and a linear scaling of 2 mm/us was applied using the Miller (1968) electron drift velocity in LXe measurements.

7.2.5 FIDUCIAL VOLUME

Different values for the fiducial volume are presented below.

Anode Segments	1	2	3	Full
Radius (mm)	3	6	9	24
Area (mm^2)	28	113	255	1810
Volume (mL)	0.39 ± 0.03	1.6 ± 0.1	3.6 ± 0.3	25.3 ± 1.8
Mass (g)	1.1 ± 0.1	4.6 ± 0.3	10 ± 1	73.4 ± 5.2

Table 5: Calculations of fiducial volume. Liquid level is taken to be 14 ± 1 mm. Density of LXe near boiling point is 2.9 g/mL.

7.3 ANALYSIS

7.3.1 NUMBER OF ^{220}Rn DAUGHTERS IN THE TPC

As described in Sec. 7.2.1, the rate of ^{220}Rn in the TPC was measured to be 4.5 ± 0.5 Hz during plate out. From this, the number of daughter atoms ^{212}Pb and ^{212}Bi present in the TPC just prior to filling the liquid xenon were calculated. The number of daughter atoms as a function of the plate out time is shown in Fig. 82 along with the data acquisition periods for each dataset. This calculation assumes that the diffusion time in the PTFE walls was less than removal time via the capillary.

7.3.2 DATA SELECTION

The trigger described in Sec. 7.2.2 captured the slow chain decays as shown in Fig. 81. The ^{212}Bi beta decay is followed by the 300 ns alpha decay of ^{212}Po ; these decays are referred to herein as “Bi-Po”.

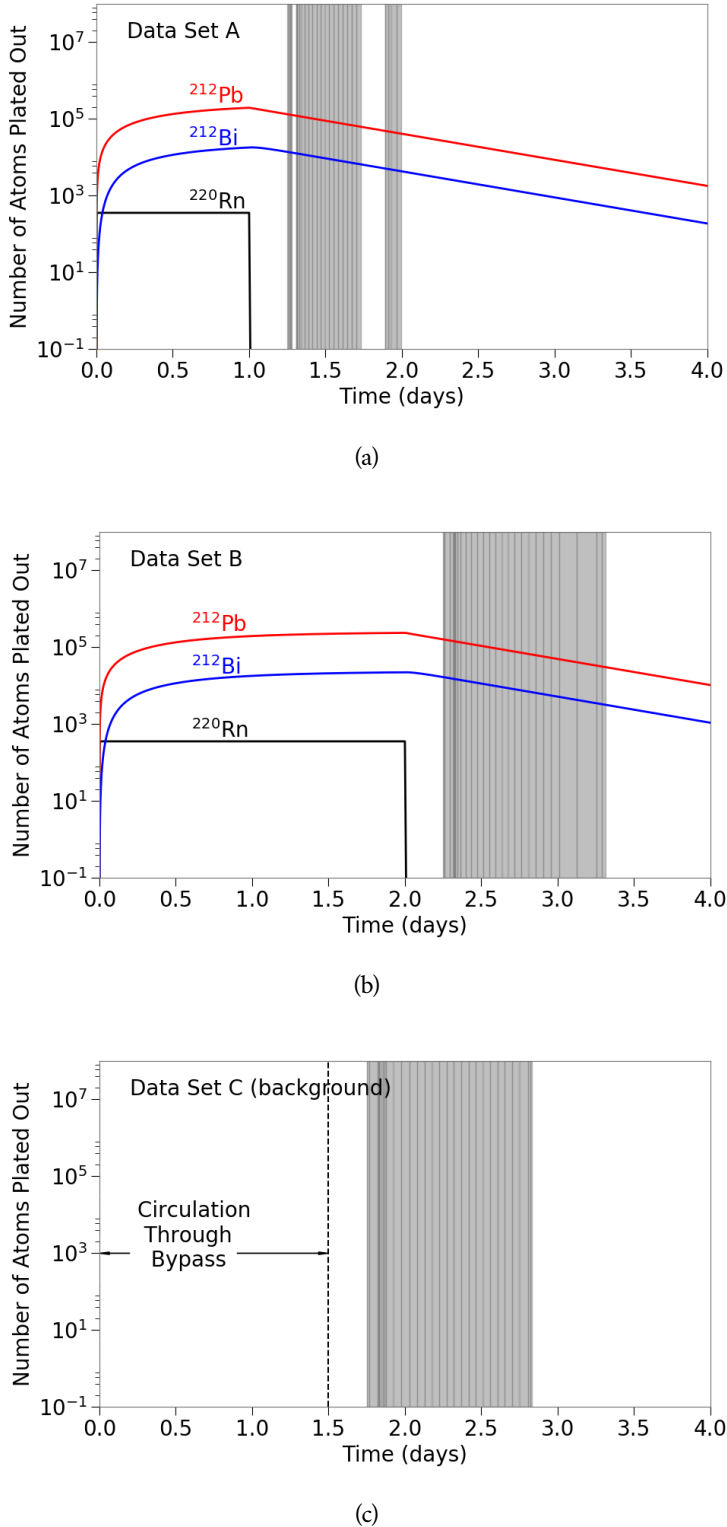


Figure 82: a) and (b) and (c) show the plateout conditions of datasets A, B, and C, respectively. The gray bands indicate time when data was being acquired. Dataset D (calibration) was taken following dataset A and consisted of a few hours.

The aim of this analysis was to reconstruct the z-position of radon daughter alpha decays via the timing difference between the S1 and S2 of an event. Therefore, Bi-Po events were rejected, as the two S2s presented a timing ambiguity. The focus was instead on identifying ^{212}Bi alpha decays. All events were expected to take place on detector surfaces, so ^{212}Bi alpha decays in the drift region indicate mobility of plated-out daughters ^{212}Pb and/or ^{212}Bi ; it was not possible to determine whether the original position was on the cathode wires, PTFE walls, or other detector surface.

The software cuts used to select ^{212}Bi alphas are described below:

1. **Data Cleaning** Remove events with any railed charge channel.
2. **Fiducialization** Require more signal in the central anode segment than the other two concentric anode segments.
3. **Select Alpha Events** The tallest pulse in an event was required to be an S1. Alphas are higher energy than the other decays in the ^{220}Rn chain, and have a characteristically high light yield, so this cut is generous in keeping all alpha events.
4. **Reject Bi-Po Topology** Of the alpha events, those with one S1 and one S2 (single-scatter) were classified as ^{212}Bi alpha. Events with two S1s (one of which is alpha-like), and one or two S2s were classified as Bi-Po.
5. **Reject Bi-Po Energy** There are two ways a Bi-Po event can mimic the topology of ^{212}Bi alpha: (i) alpha decay was prompt and so the scintillation signals from the beta and alpha were combined into one large S1 (ii) the beta was ejected into the cathode wire and therefore there was no signal detectable from the beta. To robustly identify ^{212}Bi , the alpha S1 areas of ^{212}Bi alpha and Bi-Po events from Step 2 were histogrammed and fit with Gaussian functions. ^{212}Bi alpha events were tightly selected with a high and low S1 area cut placed on single-scatter alpha events: anything above $(\mu - 3\sigma)_{\text{Bi-Po}}$ was considered a Bi-Po event and anything below $(\mu + 3\sigma)_{\text{Bi-alpha}}$ was considered a beta or gamma, and discarded (Fig. 83). It should be noted that this cut doesn't affect the signal region for ^{212}Bi alpha in bulk; it affects the region for ^{212}Bi alpha on the cathode. This cut is conservative in discarding Bi-Po events, as this leads to a more conservative fraction for dissolved fraction of ^{212}Bi alphas.
6. **Z-position Cut** Events in the cathode region were separated from events in the bulk region with a z-position cut (discussed further below).

7. **Bulk Signal Area Cut** Only ^{212}Bi alpha tagged events which also fell in a signal region expected from calibration with the ^{220}Rn flow though source (Fig. 86h) were considered to be daughters which have dissolved.

In order to choose the value for the z-position cut in Step 4, a Monte Carlo approach was used. A Bi-Po decay with a prompt alpha (appears as single-scatter) where the beta penetrates into the bulk region, could mimic a ^{212}Bi alpha bulk event. To better understand Bi-Po cathode events and the danger of mis-identifying them as ^{212}Bi alphas in bulk, a Monte Carlo study was done with the ^{212}Bi beta spectrum (the highest energy beta in the ^{220}Rn chain) to determine the maximum distance a beta could penetrate into the bulk region. The study yielded a maximum beta penetration of $z_{max,MC} = 0.12$ cm, see Fig. 84. The z position cut separating cathode from bulk was then defined to be $z_{cut} = z_{max,MC} + 3\sigma_{fit}$, where σ_{fit} is just the width of a Gaussian fit for the position of the cathode. Figures 85a and 85c show the cathode position fits as well the the location of z_{cut} . The cathode position fit error, σ_{fit} , was the same for both datasets A and B, and was also used to determine z_{cut} for the background and calibration sets.

One feature that merits further discussion from Figure 85 is the strong anti-correlation in S1 Pulse Area vs. S2 Pulse Area apparent in cathode events. The cathode region was subject to very high, non-uniform fields due to the thin wires that comprised the cathode grid. Events that occurred on the wires encountered different fields depending on their position on the surface of the wire. Additionally, two events that occurred at exactly the same spot encountered different fields depending on which direction the decay particle (alpha, beta, etc.) traveled. The amount of scintillation and ionization from an interaction in liquid xenon depends on the field at the interaction site. Higher fields result in more ionization electrons being separated from the interaction site and therefore more S2. Mono-energetic events occurring in a uniform field have small anti-correlated fluctuations in S1 and S2 size. Non-uniform fields greatly exaggerate the typical variation in S1 and S2 size resulting in the spread out cathode region (blue) observed in Figures 85 and 86 (right). Events in the bulk region encounter a relatively low, uniform field resulting in a compact signal region in S1 vs. S2 (visible in red region of calibration data, Dataset D).

7.4 RESULTS AND DISCUSSION

We observed 11 bulk ^{212}Bi alphas for dataset A, 20 for dataset B, and 1 background event in the signal region from dataset C. The counts of cath-

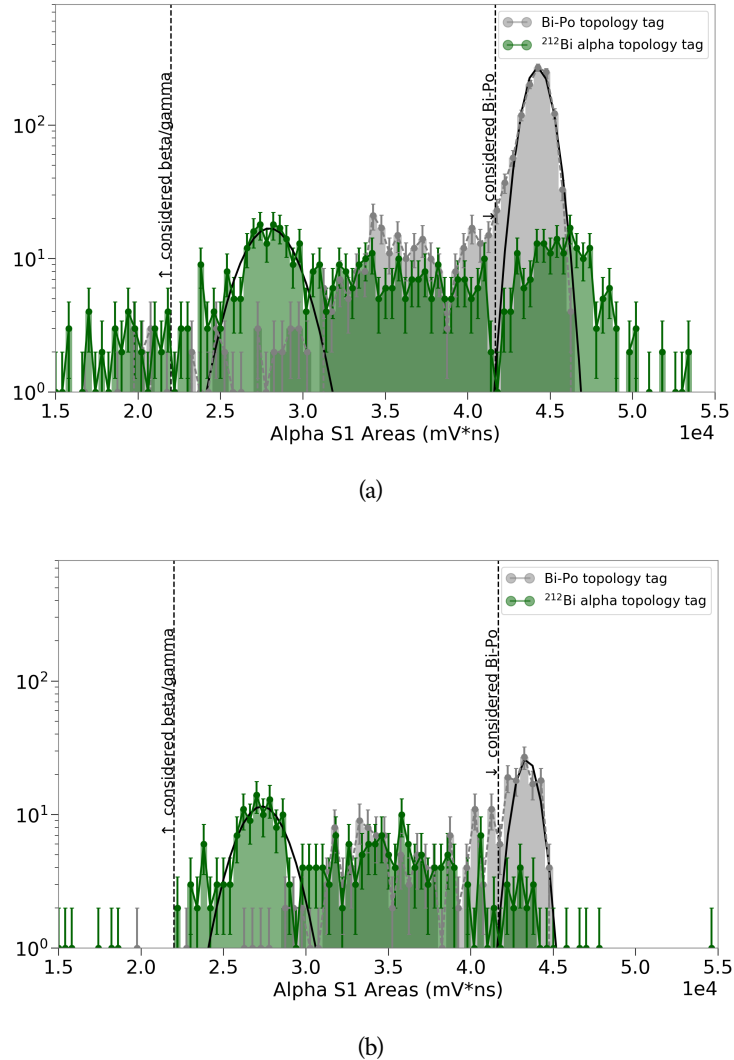


Figure 83: The S1 areas of events that were tagged using topological features.

These distributions were then used to employ the cuts in Step 3. The branching ratio for ^{212}Bi is 36:64 for α :Bi-Po. Dataset (a) showed 10:90 and dataset (b) showed 35:65. It is unclear why the branching ratios for dataset (a) deviate so much from expectation. The trigger is more efficient for Bi-Po events because those decays would produce more a larger charge signal. It's possible that the cathode being left on during the plate out procedure had some effect on the geometrical distribution of daughters on the cathode wires, which further biased the trigger.

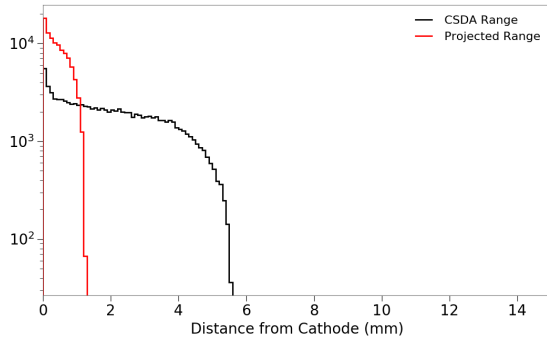


Figure 84: Monte Carlo study to find the maximum distance a ^{212}Bi beta (2.2 MeV) on the cathode could penetrate into the drift region. The projected range (red) is the relevant curve for this analysis; it shows a beta is not expected to travel more than 1.2mm from the cathode.

ode region ^{212}Bi alphas are presented in Table 6. There was only one background event observed in the signal region, so with 95% confidence the true background count is at most 4.74. The observed counts for dataset A and B lie far above the 95% confidence limit for background, indicating they are true observations of ^{212}Bi alphas in bulk. Defining dissolved fraction as N_{bulk} / N_{cath} , the dissolved fraction of ^{212}Bi alphas for dataset A (≈ 13 h livetime) is 0.035 ± 0.010 , and for data set B (≈ 25 h livetime) is 0.099 ± 0.020 .

These results indicate that either ^{212}Pb or ^{212}Bi itself is soluble to a small degree in liquid xenon.

Table 6: Number of detected alpha particle events whose energy determination was consistent with ^{212}Bi decay to ^{208}Tl . Live times are quoted in Table 4

dataset ID:	A	B	C
Bulk Events	11	20	1
Cathode Events	300	183	4

The solubility is presented in the following units:

$$\frac{\frac{Bq (dissolved)}{kg LXe}}{\frac{Bq (plated out)}{cm^2 (detector surface)}}$$

7.4 RESULTS AND DISCUSSION

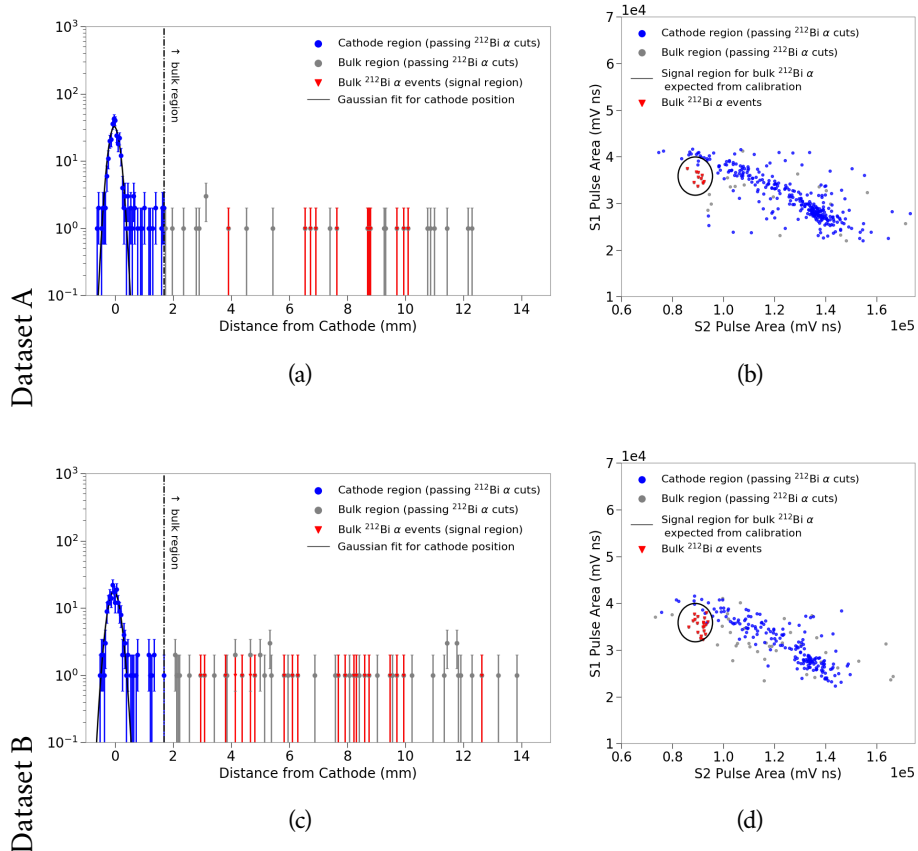


Figure 85: For datasets A and B: **(left)** Distribution of events in z . **(right)** The same events distributed in the S1-S2 plane, showing selection criteria for candidate ^{212}Bi alpha events in the bulk liquid xenon.

7.4 RESULTS AND DISCUSSION

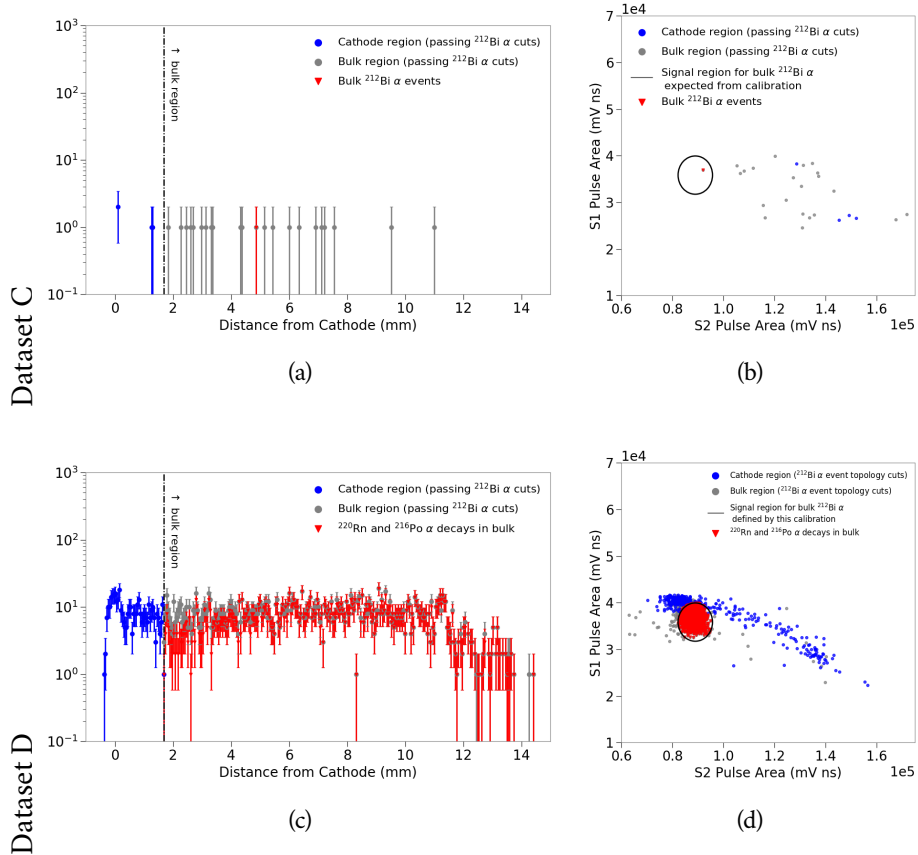


Figure 86: For datasets C and D: **(left)** Distribution of events in z . **(right)** The same events distributed in the S1-S2 plane, showing selection criteria for candidate ^{212}Bi alpha events in the bulk liquid xenon.

The solubility calculation is subject to errors from the following factors. Where appropriate, it is noted how the error taken into account in the calculation; otherwise, the assumption is stated.

1. Liquid height (folded into fiducial volume)
2. Area over which charge amps are sensitive (calculation using different fiducial volumes)
3. Area over which daughters are plated out (varying area over which ^{212}Bi is distributed; assume 10% error in area calculation)
4. Initial activity of plated out daughters (assume circulation time for gas to leave inner PTFE stack > decay time of ^{216}Po)
5. Live time calculation (uncertainty included)

The solubility found in dataset A is at worst $84 \pm 26 \text{ Bq/kg/Bq/cm}^2$ and at best $0.091 \pm 0.030 \text{ Bq/kg/Bq/cm}^2$. For dataset B, the worst case is $58. \pm 18. \text{ Bq/kg/Bq/cm}^2$ and the best case is $0.064 \pm 0.021 \text{ Bq/kg/Bq/cm}^2$.

These results are first evidence that the ^{220}Rn daughters ^{212}Pb and/or ^{212}Bi are soluble in liquid xenon. The dissolved events are a small fraction of events that are plated-out on detector surfaces. These daughters are proxies for the isotopes ^{210}Pb and/or ^{210}Bi , which undergo naked beta decays in the ^{222}Rn chain and pose a problem for liquid xenon dark matter detectors. Our study counts dissolved ^{212}Bi alpha events as well as ^{212}Bi alphas plated out on the cathode. We found 11 counts in dataset A and 20 counts in dataset B consistent with ^{212}Bi decay in the bulk region; these counts are significantly above a background count of 1. The experimental apparatus is not characterized extensively. Regardless, we carried through the solubility calculation, taking into account uncertainties to arrive at a ‘best case’ and ‘worst case’ result.

The limit derived from LUX observations, stated in the LZ projected sensitivity paper [106], is $0.1 \mu \text{ Bq/kg LXe}$ for ^{212}Bi mobility, given 50 nBq/cm^2 on PTFE panels. Our observed solubility is much greater than this. One explanation is that we are sensitive to the ‘stuck’ radon daughters that wash off easily in the first few days of an experiment due to the introduction of [LXe](#). Large TPCs may then expect an increased rate of radon daughter decays in the fiducial volume at the beginning of a search, but a decreasing rate as these are removed by the getter or are implanted in detector materials.

Another, testable, explanation that would reconcile the different solubilities in the ^{220}Rn and ^{222}Rn chain is beta ejection. Referring to Figures ?? and ??, both bottleneck decays, ^{XXX}Pb , are beta decays. However, ^{212}Pb in the ^{220}Rn chain has a beta decay endpoint of 570 keV, which

about 10 times of the endpoint energy for ^{210}Pb in the ^{222}Rn chain. Daughter recoils from beta decay are indeed small; the endpoints are approximately 0.6 eV for the recoil from ^{212}Pb decay in the ^{220}Rn chain and 0.006 eV for the recoil from ^{210}Pb decay in the ^{222}Rn chain. The physisorption potential in for both cases is expected to be below 1 eV. Depending on the exact value, which is unavailable, the ^{212}Pb decay could provide enough energy to liberate the daughter ^{212}Bi most of the time, whereas ^{210}Pb decay produces a maximum recoil value below the potential depth.

Further study, where a known amount of ^{220}Rn daughters are plated out on a known area is necessary to measure dissolution rates. Additional studies that compare the solubility of radon daughters adsorbed on different materials, and under different conditions (e.g. temperature) would also be useful. The effect of cleaning these surfaces before searching for dissolved daughters should also be investigated.

If beta recoil, not ‘washing’ by the LXe , is the cause of radon daughter solubility, then the high rate seen by this study of ^{220}Rn can be reconciled with the low rate of ^{222}Rn daughter dissolution seen in large experiments.

7.4 RESULTS AND DISCUSSION

Table 7: Using observations from 6, proceed through solubility calculation.

dataset ID:	A	B
Total Inferred Bi decays	20 ± 6	36 ± 11
Livetime (hours)	12.02 ± 0.5	23.93 ± 0.5
μBq Bi in bulk	460 ± 140	420 ± 130
Bq (dissolved) / kg LXe (smallest fiducial)	0.42 ± 0.13	0.38 ± 0.12
Bq (dissolved) / kg LXe (largest fiducial)	0.0063 ± 0.0020	0.0057 ± 0.0018

Plate-Out Areas		
	Area	
Total Internal Area Including PMT	496 cm^2	
Active Region PTFE	36 cm^2	

dataset ID:	A	B
Number of ^{212}Bi Plated-Out	13191	17280
Bq (plated-out)	2.5	3.2
Bq (plated) / cm^2 min	0.0050 ± 0.0005	0.0065 ± 0.0007
Bq (plated) / cm^2 max	0.069 ± 0.007	0.089 ± 0.009

Solubility		
dataset ID:	A	B
Solubility min	0.091 ± 0.030	0.064 ± 0.021
Solubility max	$84. \pm 26.$	$58. \pm 18.$

8

STUDIES OF DELAYED SINGLE ELECTRON SIGNALS

8.1 MOTIVATION FOR STUDYING DELAYED SINGLE ELECTRON SIGNALS

Delayed single electron signals, known colloquially as “electron trains”, are a generic single electron background in dual-phase [LXe TPCs](#). Proportional scintillation signals consistent with those of single electrons, emitted regularly over time, are known to follow high energy depositions. These electron trains can last $O(10 - 100)$ ms, which is the equivalent of several event windows for most [LXe TPCs](#). Single electron signals were observed and investigated by ZEPLIN [107] [108], Xenon100 [109], and LUX [110].

[LUX](#) collaborator J. Xu investigated delayed electron signals in [LUX](#) [110]. A plot of an electron train from [LUX](#) is shown in Figure 87. Note that the time window is orders of magnitude greater than the [LUX](#) event window of 400 μ s, and the maximum drift time for Run03 of 300 μ s. In addition to electron trains, the [LUX](#) collaboration colloquially refers to one type of delayed electron signal as “electron burps” or “e-burps”. They are characterized by the sudden emission of $O(100 - 1000)$ electrons. Xu noted that e-burps can be part of an electron train, but unlike electron trains in general, he found e-burps to be uncorrelated with the size of the previous event (see inset of Figure 87).

In Section 3.3.2, we discussed several dark matter searches that differ from the standard [WIMP](#) search and how they can be completed with dual-phase [LXe TPCs](#). In particular, recall the Xenon10 search for low-mass [WIMPs](#) [71]. The S2-sensitive trigger threshold was set to the level of a single electron, but an analysis threshold of 4 electrons was required for S2 size. The reason behind this is illustrated in Figure 90. Although single electrons following a high-energy event can be positively identified as belonging to an electron train, electron trains can last $O(10 - 100)$ ms. In any event window following the start of electron train, it is unknown whether the single electron is truly a small energy deposition from a low-mass dark matter event or if it belongs to an electron train. Moreover, sin-

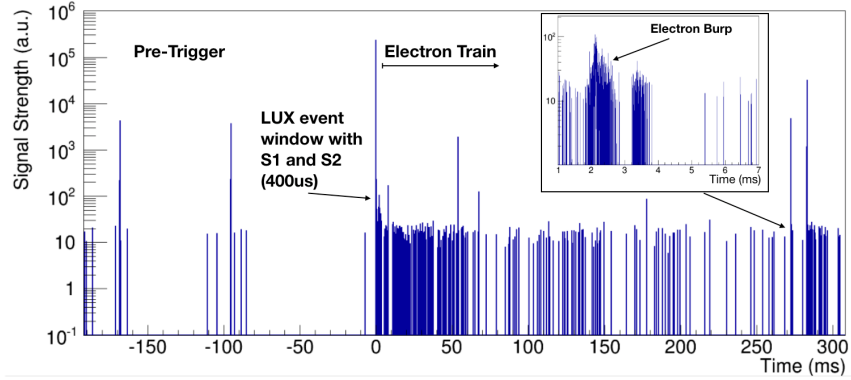


Figure 87: An electron train spanning several ms. Pre-trigger and electron train regions are indicated along with the LUX event that originated the electron train. The inset shows the shorter time structure of e-burps. The y-axis is a proxy for phd/sample. Such figures of electron trains are generated from .dat files, not from .evt files. Figure courtesy of J. Xu.

gle electrons from a train can pile up in time, creating energy depositions the size of 2 and more electrons – so an analysis threshold of 2 electrons is not sufficient to cut out electron train backgrounds. In general, electron trains are irritating for WIMP searches because some percentage of the detector livetime is taken up by electron train pile-up; but they greatly limit the discovery potential for low-mass searches, as the expected signal size (S2 of 2 or 3 electrons) is possibly electron train pile-up, and therefore must be considered as such.

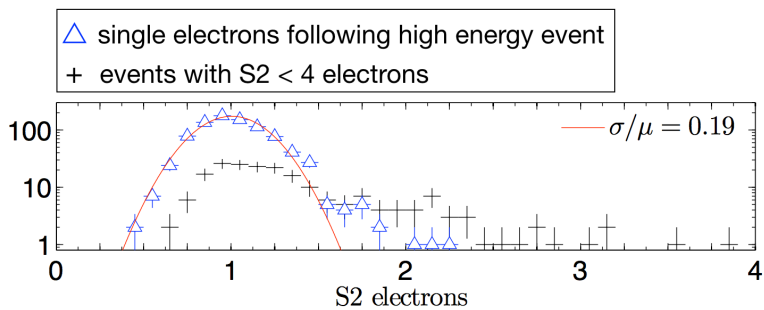


Figure 88: Figure adapted from [71].

Xenon100 measured the rates of 1-, 2-, and 3-electron signals following an S2 [109]. They saw a relation of the time constants $\tau_3 \approx \tau_1/3$ for 3-electron signals compared to 1-electron signals, and $\tau_2 \approx \tau_1/2$ for 2-electron signals. They note that if multi-electron signal results arise from

accidental time coincidences of single electrons, these time relations can be explained.

8.2 ORIGIN OF DELAYED SINGLE ELECTRON SIGNALS

While the origin of delayed single electron signals is still an area of active research, some behavior of electron trains are fairly well understood. An electron train can be split into two time regions: the primary event window ($O(100)$ μ s, e.g. 400 μ s in LUX), and the following train, which continues for $O(10 - 100)$ ms. A few features are typically evident in the primary event window, which have origin in physical phenomena. These phenomena and what is found in the literature are discussed in the following subsections. The testbed study and its result, which shed more light on the origin of delayed single electron signals, are presented later in the chapter.

8.2.1 PHOTOIONIZATION ON GRIDS

The large number of VUV photons in big S2s are capable of liberating electrons from metallic electrodes. Electrons can be photoionized on any grid in the TPC, but the effect is largest on the grids closest to the gas gap where the S2 is generated. Photoionized electrons from the anode aren't detected because they have essentially no space in which to proportionally scintillate. Photoionized electrons from extraction grid are directed toward the gas gap, extracted and then undergo proportional scintillation. These electrons join the S2 signal at a delay approximately equal to the distance between the extraction grid and the liquid-gas interface. Large S2s have tails that are composed of electrons photoionized from the extraction grid. An average of many high-energy S2s, clearly shows the photoionization feature (Figure 89).

8.2.2 PHOTOIONIZATION OF IMPURITIES

Electronegative impurities in the liquid (e.g. O₂, N₂) capture ionization electrons from events as they are drifted to the gas region (e.g. O₂ binds an electron at 0.45 eV to become O₂⁻). Just as the VUV photons can ionize electrons from grids, they can also ionize electrons attached to impurities. Xenon100 found that the rate of single electrons in the primary event window scaled with S2 size, as well as the concentration of impurities [109] (see Figure ??). Some of the electrons in the primary event window of

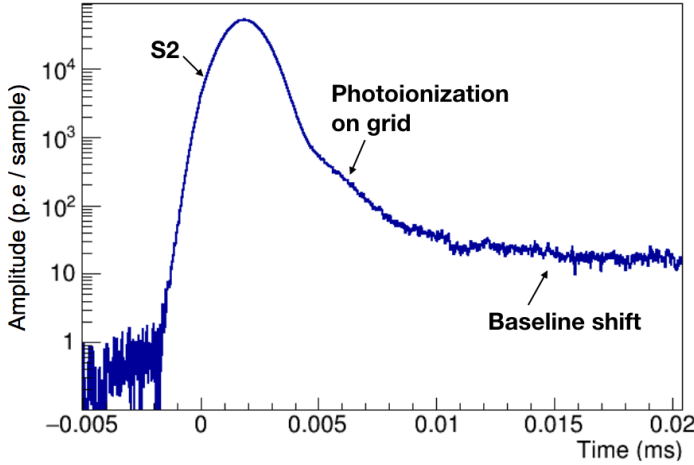


Figure 89: The average of many high energy S2s from LUX, plotted with logarithmic y-scale, showing a prominent photoionization feature. After the photoionization, an instrumental effect is visible: for the highest-energy events, one to a few PMTs often do not return to baseline quickly, which gives the single electrons in the following train artificially higher areas. Figure from J. Xu.

an electron train are now believed to come from photoionized impurities. This is supported by Xenon100 data which showed that the rate of single electrons has a sharp cut off corresponding to the maximum drift time, and the the PMT hit pattern of the multi-electron signals are not localized around one PMT but rather spread over the PMT array [109].

8.2.3 DELAYED EXTRACTION OF TRAPPED ELECTRONS

Dual-phase LXe TPCs depend on the ability to extract electrons from liquid into gas. This is accomplished with some efficiency, called the EEE. Gushchin et al. measured the absolute EEE in xenon and argon in 1982 as function of electric field [111] (see Figure 91). Their result extends to an extraction field of 5 kV/cm in the liquid. It is common practice for modern experiments that achieve an extraction field $\gtrsim 5\text{keV}/\text{cm}$ to assume they have 100% extraction, an assumption based on the Gushchin result. Relative extraction efficiency is measured only by the size of the S2 scintillation light and inferred number of initial ionization electrons based on calibration source energy and knowledge of recombination. Relative measurements of EEE as a function of extraction field assume 100% extraction at the highest field and scale the other points accordingly. In contrast, absolute extraction efficiency measurements measure the num-

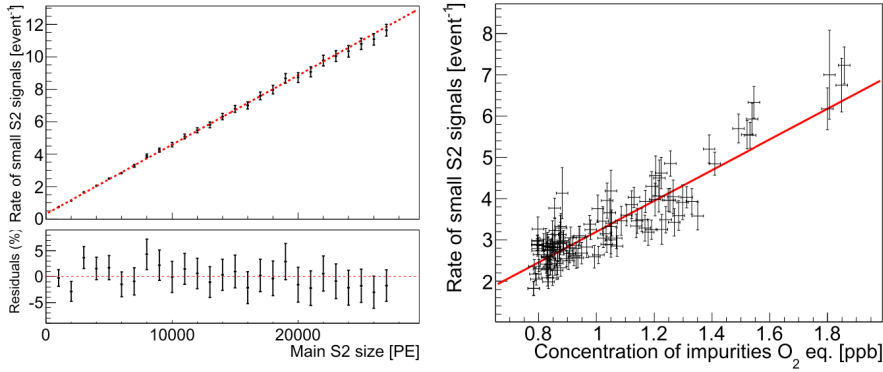


Figure 90: (left) The per-event rate of single electron signals 20 to 150 μ s after the main S2 of a single-scatter type event as a function of the main S2 size. The fit line and residuals show a good proportionality in the relation. (right) The per-event rate of single electron signals, for events with the main S2 between 5000 and 10000 phe, as a function of the O₂-equivalent concentration of impurities in liquid xenon. Figures from [109].

ber of electrons generated in the liquid as well as how many are extracted with no scaling.

Since there does not exist a second absolute measurement of EEE out to higher extraction fields, it is uncertain when 100% EEE is reached in LXe. However, it is well known that the number of extracted electrons depends on the extraction field. In addition to photoionization of impurities, it is thought that the unextracted electrons are liberated from the liquid surface at a later time, making up some component of electron trains [109], [112]. To understand why we must consider the energy of the electrons in the liquid, and the potential barrier they encounter in order to escape into gas.

When an electron approaches a dielectric boundary held at a constant potential, a potential barrier results from its image charge. This barrier, called the Shottky barrier, takes the form:

$$\phi_b = \frac{e^2}{8\pi\epsilon_0 z} \frac{\epsilon - 1}{\epsilon + 1} \quad (46)$$

where z is often taken to be the lattice spacing of the medium, ϵ is the dielectric constant of the medium, and ϵ_0 is the usual vacuum permittivity. If LXe is arranged in a simple cubic lattice, $z \approx 4 \text{ \AA}$, and the calculation yields $\phi_b = 0.61 \text{ eV}$ [113]. The potential barrier of liquid xenon was measured by Tauchert to be 0.67 eV [114]. There are two modes for emission of electrons across a surface boundary: (1) “hot” electrons accelerated by an electric field gain enough energy to overcome the barrier and be ex-

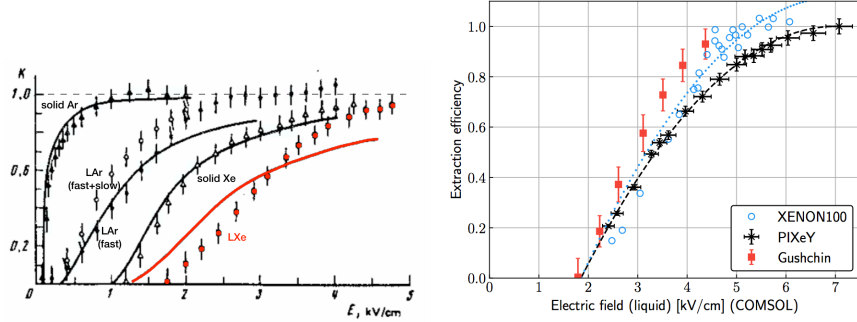


Figure 91: (left) The absolute EEE measured by Gushchin from [111]. The LXe points were re-colored red. (right) Two relative EEE measurements from modern experiments, Xenon100 and PIXEY, compared to Gushchin. The plot is from the PIXEY result [112], where the authors fit their result with a quadratic function ($y = ax^2 + bx + c$). The fit to the PIXEY data (black dashed line) is scaled by a constant and applied to the Xenon100 data (blue dotted line).

tracted (2) emission of thermal electrons, where only electrons in the tail of the velocity distribution have enough energy to escape the boundary. For an external field E , the Schottky barrier is lowered by

$$\Delta\phi_b = e \left(\frac{eE}{4\pi\epsilon_0 z} \frac{\epsilon - 1}{\epsilon + 1} \right)^{1/2} \quad (47)$$

The E field also results in the aforementioned heating of the electrons. The new energy distribution f can be determined by solving the Boltzmann equation as in [115], but this is not shown here. With f and adjusted barrier height, the EEE as a function of electric field can be calculated. It is the fraction of electrons with energy expectation value above $\phi_b - \Delta\phi_b$:

$$\kappa = \int_{\phi_b - \Delta\phi_b}^{\infty} K^{1/2} f(K) dK / \int_0^{\infty} K^{1/2} f(K) dK \quad (48)$$

$K = K(E)$ is the electron energy, which is implicitly a function of the electric field and $f(K)$ is the energy distribution of the electrons under the influence of an electric field. The factor within the integral is $K^{1/2}$ instead of the usual K in order to select only electrons that have an upward velocity component. The red LXe line in Gushchin's EEE result (Figure 91 (left)) is from this calculation with the assumption that $\phi_b = 0.61$ eV. Bolozdynya follows a similar approach and notes that electrons which are not emitted as hot electrons are thermalized by collisions and can be emitted later as thermal electrons [116]. Others have treated the potential barrier as a free parameter and fit to data. Gushchin, seeing that the line

did not fit the data for LXe , treated the value of ϕ_b as free in the integral above. He found $\phi_b = 0.85$ eV was a better fit [111], but the agreement is still not very satisfying. Sorensen implemented an n -th chance model for electrons approaching the liquid-gas boundary, and found that with $\phi_b = 0.34$ eV and $n = 20$, his model fits Gushchin's data [113]. If the n -th chance model is applied, with some assumptions about the relaxation time for electrons to be thermalized, the time constant for emission of thermal electrons is $O(10)$ ms. Both Bolozdyna and Sorensen note that the relaxation time is dependent on field (strength and direction), temperature. Sorensen adds possible diffusion effects, fluid flow, varying surface height, etc. Although research is still on-going into how to properly model the physics of electron extraction, there is agreement that a fast component from extracted hot electrons yields the initial S2 and a thermal component from the unextracted electrons contributes in part to the electron train.

8.3 TEST BED STUDIES OF ELECTRON TRAINS

An initial goal of the test bed described in Chapter 6 was to complete an absolute measurement of EEE . Unlike typical TPCs , the testbed can be “overfilled”, with the liquid level above the anode, and the generation of ionization electrons in the liquid can be measured with the charge amplifiers. The liquid level can then be dropped between the anode and extraction grid for a measure of extracted electrons with S2 (and with the charge amplifiers). During the multi-year process of instrumenting and understanding the test bed, this goal changed and evolved. In order to provide a record, the remainder of this chapter briefly describes the attempts made with the radon source and configuration as in Chapter 7. Finally, the most recent results published in [117], which used the ^{210}Po source described below, are summarized.

8.3.1 RADON SOURCE AND "FULL TPC CONFIGURATION"

Here, full TPC configuration refers to the same detector configuration as in the previous chapter (Chapter 7); specifically, there is a 1 cm drift region and an 0.5 cm extraction region. Both cathode and extraction grids are employed. The ^{220}Rn flow through source was initially chosen for electron train studies because of some nice properties of alpha decays. The fast chain alphas from ^{220}Rn are:

- **High Energy** The alpha events in the ^{220}Rn fast chain have energies of 6.4 MeV (^{220}Rn) and 6.9 MeV (^{216}Po). $W_{\text{LXe}} = 13.7$ quanta/eV, so these alphas generate $O(500,000)$ quanta. Although 90%

of alpha energy goes into S1 [59], that still leaves $O(50,000)$ electrons to be detected. In contrast, a 662 keV ^{137}Cs button source produces $O(50,000)$ quanta, but this value is \sim halved by recombination. Alpha light and charge yields also do not vary greatly with applied field (Figure 18 (right)), which is convenient from an experimental standpoint of tagging a signal region and adjusting trigger conditions.

- **Uniformly Distributed with Compact Track** The ^{220}Rn can be deposited directly into the LXe , yielding a uniformly distributed source which can be fiducialized to the inner-most anode segment to avoid field edge effects. Alphas do not travel far, and so a deposition could be realistically expected to deposit all its energy in the (x, y) resolution of the detector, i.e. under one and only one anode segment. This is contact to betas, which can travel; recall the 2.2 MeV beta that could travel 1.2 mm from Chapter 7).

We expected to be able to select the monoenergetic alpha signal of either ^{220}Rn or ^{216}Po with the PMT signal. However, PMT saturation merged the two fast chain alphas in the S1 spectrum. There are two types of PMT saturation effects relevant to the R8778 PMT s used in LUX : anode saturation and capacitor depletion [54]. The effects of the two types of saturation are shown in Figure 92. Quoting directly from [54]:

- **Anode Saturation** The repulsive field created by a large number of electrons confined to a small spatial extent (an effect known as space-charge) yields nonlinear signal production. Since the electron cloud density is exponentially larger at the latter stages of the photomultiplier, this effect is most dominant at the anode. Anode saturation is only dependent on the instantaneous (peak) current value of the output signal. Anode saturation prevents the electron signal in the anode from further increasing. When the anode is fully saturated, the output signal cannot increase in size any further. As such, anode saturation defines the maximum peak signal that the PMT can output. Increasing the voltage across the latter stages can provide a modest increase in anode linearity.
- **Capacitor Depletion** A PMT is a current source. Due to the nature of the electron multiplication process, the signal current direction is opposite to that from the bias current. When a large signal current pulse is generated at the anode, the PMT bias current in the last resistor decreases proportionally and the last dynode stage becomes temporarily unbiased. This effect leads to a decrease in signal size (smaller gain) and can completely turn off the multiplication process if the signal current is comparable to the bias current.

A common method for mitigating the dynode voltage loss effect is to add capacitors that can provide reserve charge during a signal current pulse. These capacitors are called decoupling capacitors. Saturation effects from capacitor depletion occur when the reserve charge in the decoupling capacitors is insufficient to counteract the signal current and prevent PMT un-biasing. Whereas anode saturation is caused by the instantaneous current, capacitor depletion is caused by the total charge drawn for a signal

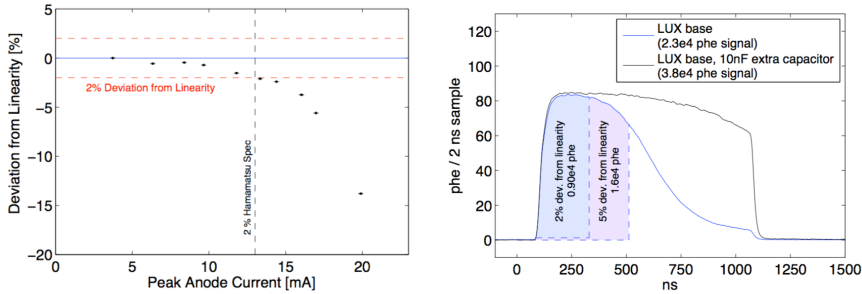


Figure 92: (left) Effect of anode saturation measured as deviation from signal linearity as a function of the peak anode current. (right) Capacitor depletion in the R8778. The blue trace shows the largest S2-like pulse that can be generated with a LUX voltage divider base (generated with a $1 \mu\text{s}$ square pulse on a blue LED); the 2% and 5% deviations from linearity is shown. The fall-off indicates the capacitor is depleted and the photomultiplication process is temporarily turned off. The black trace shows the effect of adding an extra capacitor between dynodes Dy9-Dy10. Figures are from [54], which also contains more information about the LUX PMTs and bases.

It is noted in C. Faham's thesis that any signal within $50 \mu\text{s}$ after a large pulse is also subject to non-linearity [54]; therefore, the S2 signals also did not yield a usable spectrum for separating ^{220}Rn from ^{216}Po decays. Operating the PMT at a bias voltage than $\lesssim 1000 \text{ V}$ resulted in less visible saturation, but single photoelectron sensitivity was lost below an operating bias voltage of $\lesssim 1200 \text{ V}$. Since single electron proportional scintillation signals are comparatively small, single phe sensitivity was desired for electron train studies. A series of masks were implemented to try reduce the overall light collection, while still retaining single phe sensitivity. Of course, on the other side, over-masking and not collecting enough photons would also result in inability to distinguish peaks. The masks are shown in Figure 94. Initially, we started with the smallest mask and thought we had made the mistake of cutting out too many photons. However, even with the smallest mask size, which reduced the effective PMT

cathode area by ~98%, the anode current was estimated to be ~50 mA, which from Figure 92 is far past where the effects of anode saturation cause loss in signal linearity. The anode current can be estimated using the following relations:

$$I_{PMT} \approx \frac{N_{photons} \cdot G \cdot e}{S1_{width}} \quad (49)$$

Where G is the **PMT** gain. Note that the numerator gives the charge at the **PMT** anode and the $S1_{width}$ is in units of time; thus the equation above is a simple current = charge / time relation. For the 2% mask, the highest voltage without visual saturation was 1250 mV. The single phe peak was at 35 mV/ns for that bias voltage, which corresponds to a gain of 8.7×10^6 . **PMT** gains can be calculated by the relation:

$$G = \frac{SPHE \cdot 1 \times 10^{-12}}{R \cdot e} \quad (50)$$

Where $SPHE$ is the pulse area of a single photoelectron in mV/ns, obtained from a spectrum of dark current pulses; an example of a single phe spectrum in Figure ?? shows a single phe peak at about 80 mV/ns. R is the effective output resistance of the **PMT** base, $R = 25\Omega$ for the **LUX PMT** bases [54]. The factor 1×10^{-12} reflects that the original photoelectron was amplified by the 12 dynodes of the R8778. The average alpha pulse area with the 2% mask and the **PMT** at 1250 mV bias was 37500 mV/ns, so combining with the single phe size, $N_{photons} = 1070$. Combined with a typical $S1_{width}$ of 30 ns, this yields $I_{PMT} \sim 50$ mA,

While **PMT** saturation was the main challenge for selecting a monoenergetic source from the ^{220}Rn fast chain alphas, geometrical signal efficiency was also an issue. The central anode segment was only 1% of the total anode area, so most of the signal was not in this area. The radon could be distributed directly into the teflon stack (with a **PTFE** tube) for a higher rate, but this increased the noise environment for the charge amplifiers. In theory the charge spectra should have had two distinct populations for the ^{220}Rn and ^{216}Po alphas, but with the slow trigger rate and ambient background radiation (β, γ) depositing various amounts of charge across the anode segments, two peaks could not be distinguished. A large loss in charge was also observed across the extraction grid (see Figure ??), which decreased the signal to noise ratio. Bunemann's equation describes the necessary condition for grid transparency for transiting charges, i.e. it

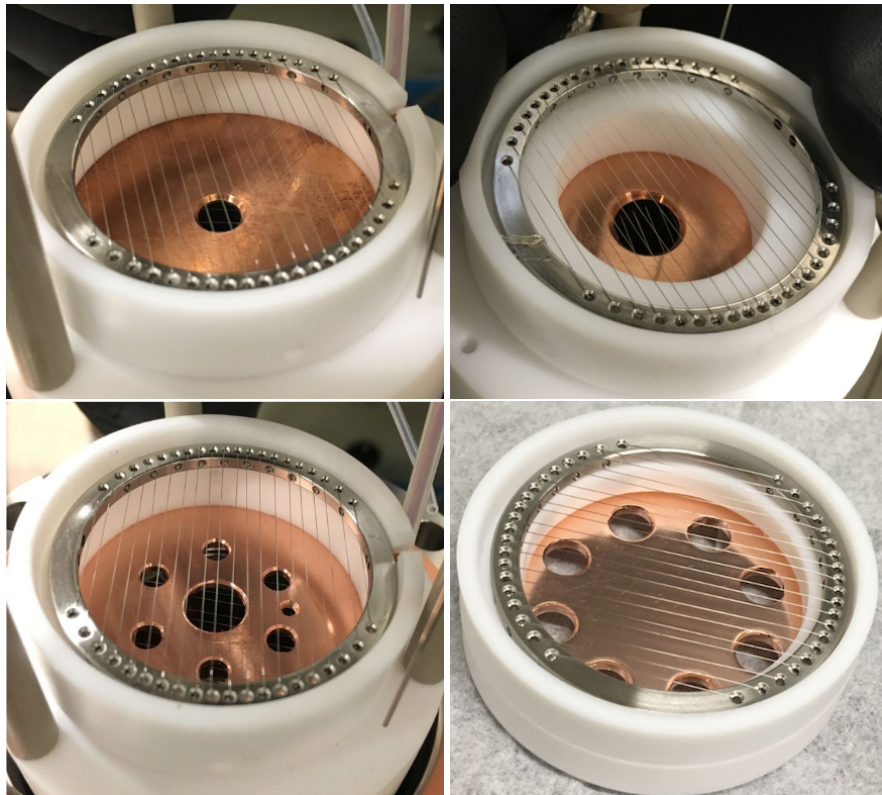


Figure 93: A series of [PMT](#) masks made from [CF](#) blanks which reduced the light collection area of the [PMT](#) to approximately 2%, 5%, 15%, and 10% (clock-wise from top left). The masks were installed in place of the [PMT](#) shield grid, and similarly to the [PMT](#) grid, they were kept at the same bias voltage of the [PMT](#).

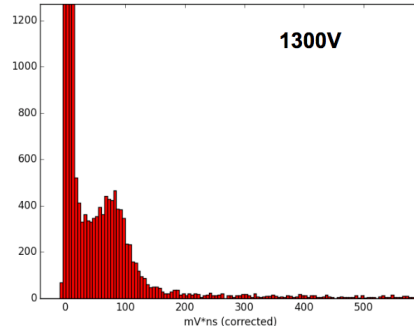


Figure 94: The single phe spectrum from the [PMT](#) with a bias voltage of 1300 V. The spectrum was obtained by using a variable gain amplifier to 100x amplify the [PMT](#) signal (at room temperature, in vacuum). A **NIM!** quad discriminator was used to externally trigger the picoscope. The waveforms were summed in a fixed window, and the results were histogrammed.

describes what relative voltages of cathode, grid, and anode result in zero electric field lines from the cathode terminating on the grid [118] [119]:

$$\frac{V_A - V_G}{V_G - V_C} \cdot \frac{D_{C-G}}{D_{G-A}} \geq \frac{1 + \rho[1 + \frac{d}{4\pi D_{G-A}}(\rho^2 - 4\ln\rho)]}{1 - \rho[1 + \frac{d}{4\pi D_{C-G}}(\rho^2 - 4\ln\rho)]} \quad (51)$$

Where C denotes cathode, G denotes grid, and A denotes anode. d is the grid pitch, D_{C-G} and D_{G-A} are respectively the distances between $C-G$ and $G-A$ and ρ is defined as $\rho \equiv 2\pi \frac{r}{d}$ where r is the grid wire radius. An example set of possible cathode voltages for a grid voltage of 2.5 kV is shown in Figure 95. The charge-vs-drift plot in Figure 96 shows a loss of charge across the grid for voltage setting $V_G = -4.0$ kVm, $V_C = -6.0$ kV, and $V_A = 0$ V. According to Bunemann's equation plotted in Figure 95, a cathode voltage of $V_C = -6$ kV should have resulted in a transparent grid. Different voltages of V_C were also tried, but they resulted in smaller drift fields, which reduces the charge yield from alphas. It is possible the grid transparency condition was affected by the relative angle of the cathode grid wires to those of the extraction grid; this was not investigated further.

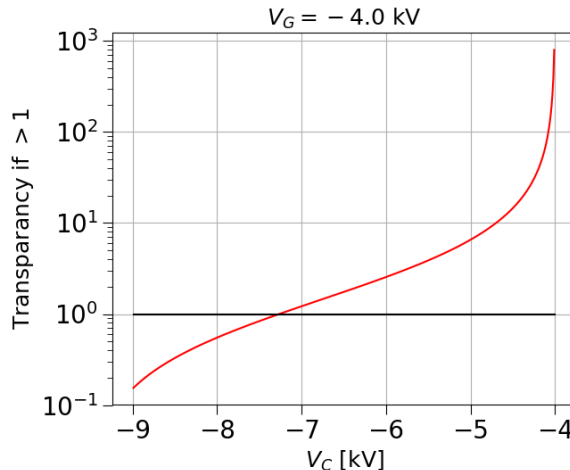


Figure 95: Bunemann's condition for grid transparency. Cathode voltages from -7.24 kV to -4 kV should result no charge being collected on the grid.

Recall from Chapter 7 that the late chain alphas were separable on a basis of PMT S1 signal. The possibility of using the plated out alpha decays of ^{212}Bi and ^{212}Po for electron train studies was also investigated, but it was difficult to reach the purity necessary to gain a robust signal from the cathode. Note that the bullseye charge amplifier signals approach noise level for signals from the cathode (Figure 96 (right)). Again, it should in

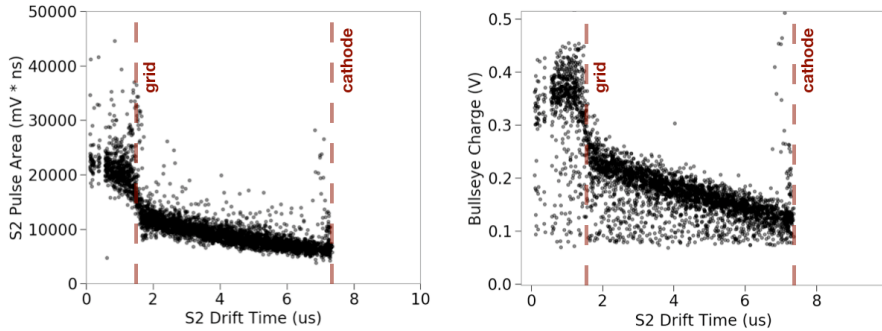


Figure 96: Ionization charge vs. drift time presented in both S2 (left) and charge amplifier voltage from the central anode segment (right). A ~50% drop in signal is visible between events occurring above the grid and events occurring below the grid. The effect of purity is also visible in the fall off charge signal with drift time. The points under the obvious line in the charge amplifier plot are from events which share charge with other anode segments.

theory have been possible to distinguish two peaks in the charge spectra alone, but this time there was an additional complication of the beta spectrum (recall a ^{212}Bi beta precedes the ^{212}Po alpha decay, this is the Bi-Po) to the issues described above. The trigger efficiency was biased to events with more charge, which made collection of a population of ^{212}Bi alphas more difficult, and the beta spectrum polluted the charge spectrum.

8.3.2 POLONIUM SOURCE AND "EXTRACTION REGION ONLY" CONFIGURATION

The grid was removed and the separation from cathode to anode was reduced to 0.5 cm. This configuration mimics the extraction region of a TPC; there is no separate drift region. A diagram of the configuration is shown in Figure 97. The PMT base was changed to an LZ! (LZ!) PMT base, which has larger capacitors. However, capacitor depletion was still evident in the PMT trace for alpha decays.

Literature refers to the spontaneous deposition, an irreversible adsorption process, of polonium from an HCl solution on copper, silver, and nickel [120] [121]. A solution of aqueous ^{210}Po (PoCl_4) was obtained and the efficacy of this process on stainless steel was tested on a ~1 mm segment of the central cathode wire. A dropper was used to immerse the wire segment in the ^{210}Po solution, and the solution was allowed to evaporate. A $\frac{1}{4}$ in blank gasket was placed under the wire to hold the drop of solution in place during evaporation. The grid was then placed in the TPC and xenon was condensed as normal. The ^{210}Po deposition on the cath-

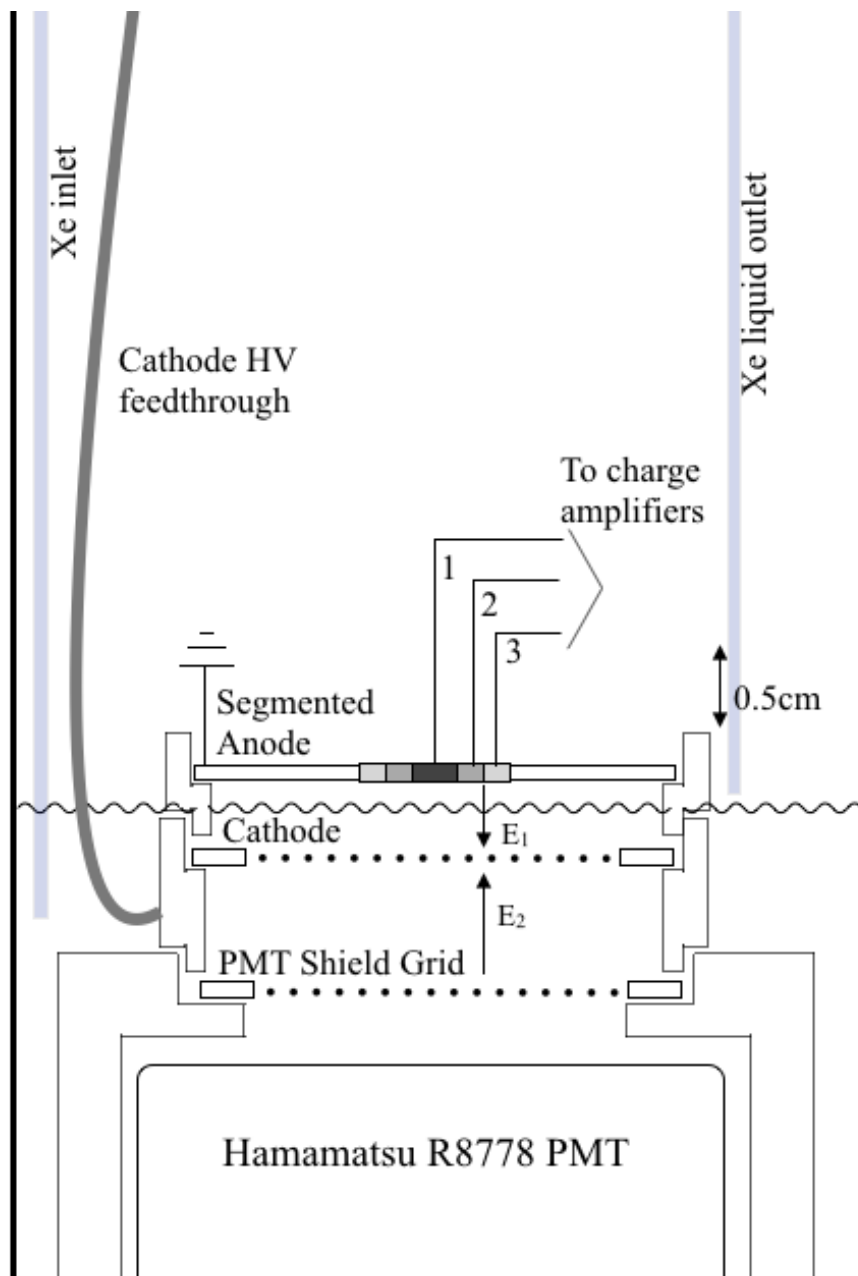


Figure 97

ode wire was robust to dissolution in the [LXe](#) (Figure 98). The ^{210}Po was also found to remain on the grid over the course of multiple fills, and the rate observed was slightly lower than, but statistically consistent with the ^{210}Po half-life. There were no background data sets acquired to investigate whether the few events in Figure 98 (right) with drift times shorter than those consistent with the cathode were consistent with background.

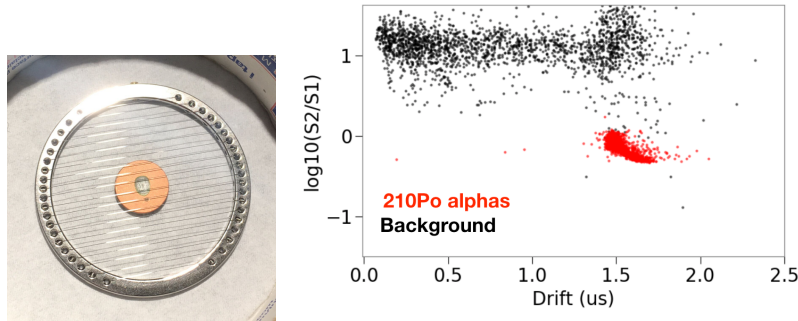


Figure 98

^{210}Po is a 5.3 MeV alpha-emitter, so it has the same high energy / many quanta generated benefit as noted above (see Figure 99 for a decay scheme). The deposition location was chosen to be directly under the central anode segment, which increased detection efficiency. The effect of non-uniform recombination on the grid wires is visible in polonium source, as it was visible in the plated-out radon daughters. At longer drifts, the ratio S2/S1 decreases, indicating that the decays occurred in a lower-field region (see Figure 100.)

Both ^{210}Po alpha decay and, in the case the alpha went into the wire, recoils of the ^{206}Pb nucleus were observable (Figure 101). The trigger used to observe these events was similar to that described in Chapter 7: a coincidence between [PMT](#) and central anode segment was required. If ^{206}Pb were desired, the [PMT](#) discriminator was adjusted to selectively trigger on smaller traces. As visible in Figure 101, the ^{210}Po alpha provided a much richer electron train, and so these events were used in the study described in the following section.

8.4 ELECTRON TRAIN STUDY SUMMARY

The study done with the ^{210}Po cathode wire source and the extraction only [TPC](#) configuration is described in detail in [117]. Here, a short summary follows. Data were taken with cathode voltages of 3 kV, 4 kV, 5 kV, and 6 kV, and ^{210}Po alpha events were selected. The waveforms of the events were stacked, as in Figure 102. Two distinct time components are

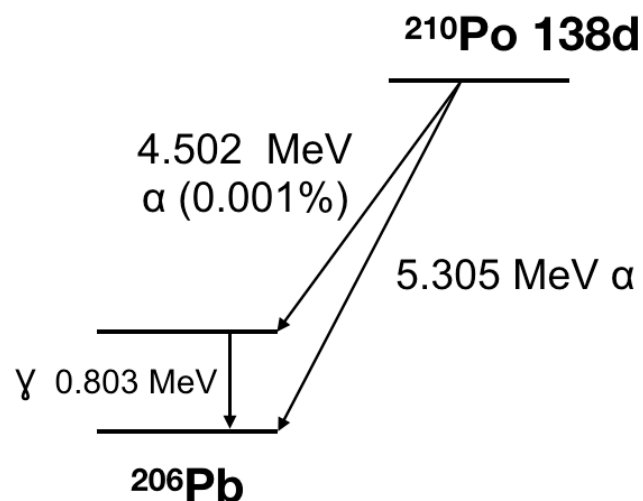
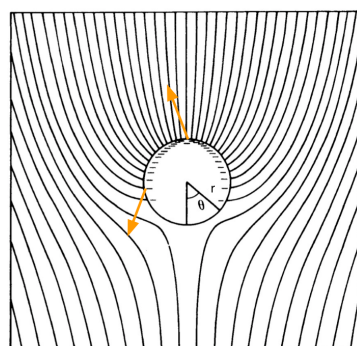
Figure 99: ^{210}Po decay scheme.

Figure 100: Different field strength depending on particle trajectory. Adapted from [122]

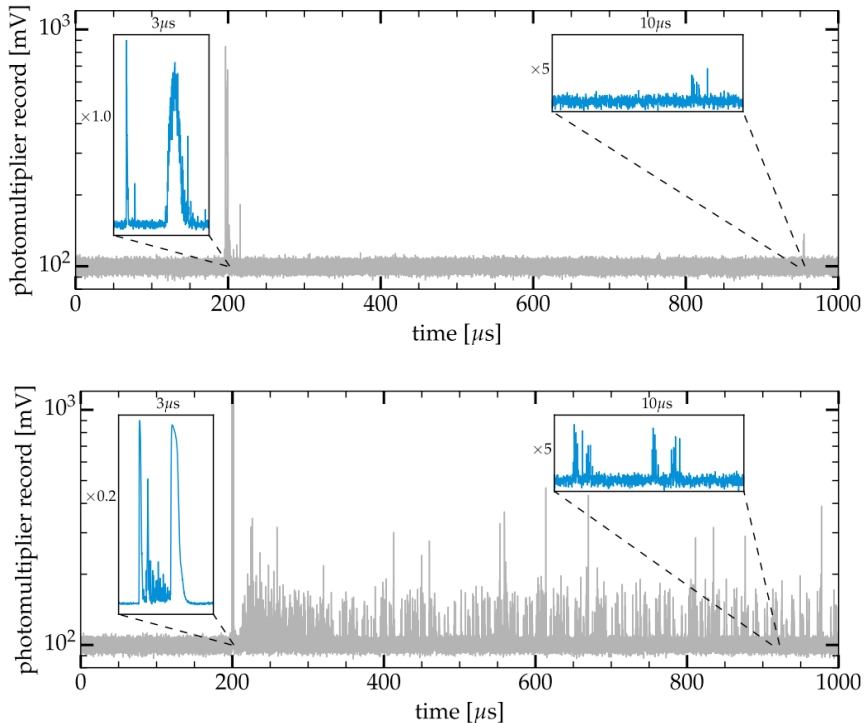


Figure 101: (top) Recoiling ^{206}Pb nucleus. (bottom) ^{210}Po alpha decay. Capacitor depletion is visible in the S2 shape, and $\sim 20 \mu\text{s}$ dead time between the S2 and start of the electron train. Insets on both (top) and (bottom) show detail of the event S1 and S2, and electron train segments.

From [117]

evident in the electron train: fast and slow. Notice the large dip in the **PMT** signal followed by a rise back to the electron train – this is the classic signature of capacitor depletion-type **PMT** saturation. Due to the **PMT** saturation, we were unable to observe any photoionization on grids feature following the S2.

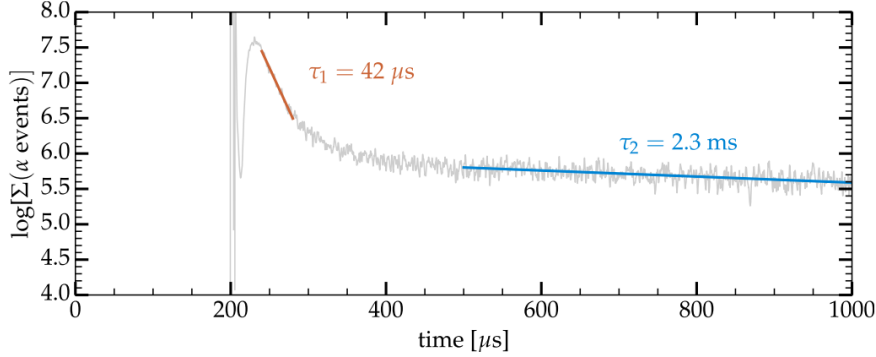


Figure 102: Stacked waveforms and fits from a dataset with cathode voltage at -4 kV. From [117]

The quantity of interest is the number of electrons in each component of the electron train compared to the previous S2. Since the S2 saturates the **PMT** biasing circuit capacitors, the measurement of S2 electrons is done with the charge amplifiers. It was found for **PMT** voltages above ~ 1100 V in gas or 600 V in liquid, the raw charge amplifier signal mirrored the **PMT** trace (see Figure 103). The effect was likely caused by the size of the generated at S1 and S2, which was in turn dependent on **PMT** bias voltage. Two Frisch grids (cathode and **PMT** shield grid) were located between the anode and the **PMT** so the charge amplifiers should not have been able to “see” the electron cascade in the **PMT**. The **OV!** (**ovi**) electronics were investigated for a location where the **PMT** signal could have been picked up, but none was found. The effect was likely due to pickup on the charge amplifier electronics within the **IV!** (**IV!**), as the charge signal output cables were unshielded; however, the **PMT** signal output cable was shielded, with the shield at ground, so it is unclear how the signals became coupled. To solve the issue, the **PMT** was merely turned off and the charge signal was acquired separately. Since a trigger threshold could be set for the charge amplifiers with the **PMT** at some low, nominal voltage, it was assured alpha events were being collected and not some background. The step height of the raw charge signals from the central anode segment were found using the step finding algorithm described in Section 6.6.3. Several events were histogrammed and the mean of a gaussian fit was found and converted to the number of electrons (Figure 104).



Figure 103: Examples of the charge amplifier mirror effect on one anode segment. The example (left) is an event where charge is collected on the anode segment, and so the charge amplifier signal trace shows a step. The example (right) shows the charge trace mirroring the PMT, but with no charge collected on the anode segment.

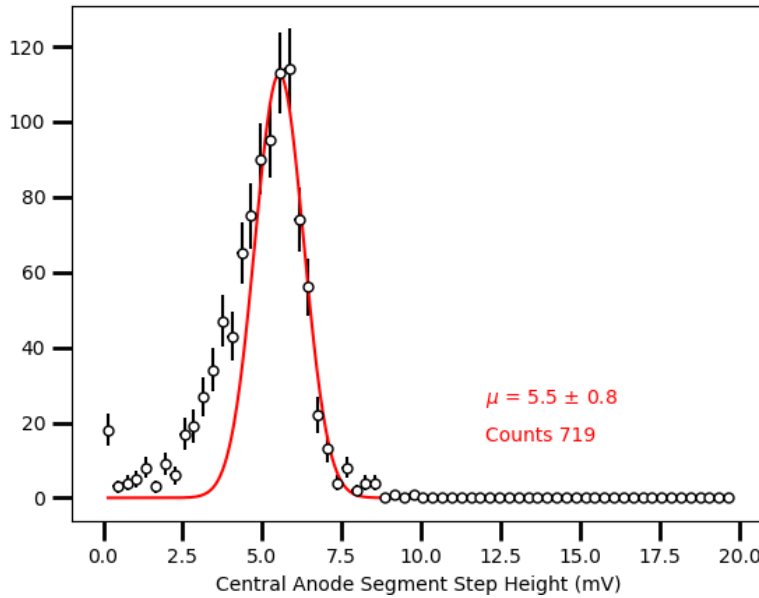


Figure 104: Histogram of charge amplifier step height for a cathode voltage of -3 kV. The histogram is skewed by wire position-dependent recombination; the same effect is visible in Figure 98 (right). This mean of the fit was converted to electrons using the manufacturer's specification of charge amplifier gain, 1.4 V/pC. 5.5mV converts to 24500 electrons.

The number of electrons in the train were reconstructed by summing the PMT area above the rms-noise level, and dividing the result by the single electron size, which was measured at each cathode voltage. Based on the time constants of the fast and slow components, the number of electrons in each component was extrapolated forward to infinity and backward to the S2, correcting for the other time component. This method was preferred to pulse-funding and counting the single electrons because single electrons pile up in time, resulting in multi-electron pulses, which would have introduced a new source of error. The single electron peak was acquired with a similar method as the single photoelectron peak described above; the obvious difference being that the PMT was immersed in liquid xenon and the ^{210}Po was generating the electrons. An example of the single electron and photoelectron peaks is shown in Figure 105.

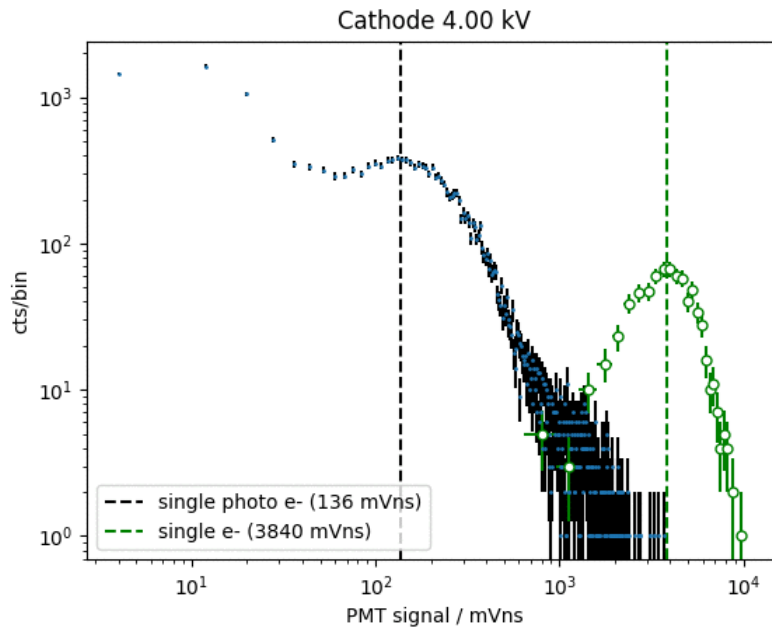


Figure 105: Single electron and photoelectron peaks obtained in liquid conditions for a PMT bias voltage of 1500 V.

The number of electrons in the fast and slow components found in the PMT trace, as a fraction of the number of electrons found in the S2 via the charge amplifiers is shown in Figure ??.

The fast component of the train decreases in amplitude relative to the prompt electrons as electric field increases. This is the behavior expected if delayed extraction is the cause of electron trains. The slow component, however, increases slightly with electric field, which does not make sense if the slow part of the train has physical origin in the delayed extraction of electrons. The TPC was left under stable operating conditions for 5

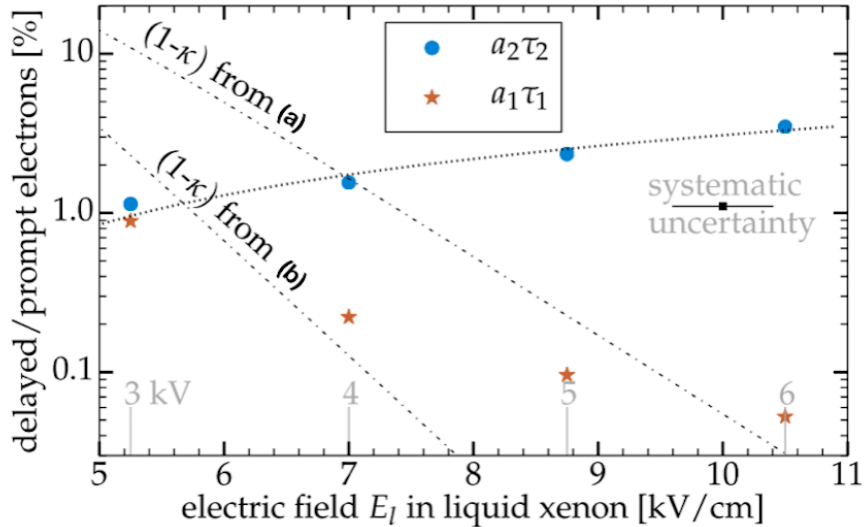


Figure 106: κ is the extraction efficiency as in Equation 48, so unextracted electrons should scale as $(1 - \kappa)$. In this thesis, (a) is reference [111], an absolute measurement of EEE; (b) is reference [112], a relative measurement of EEE. The methods use different methods and assumptions; they are shown to illustrate that the fast component follows the behavior trend of what is expected from unextracted electrons.

days, during which time the xenon was continuously purified through the getter. Typical flow rates were 0.2 slm, which correspond to a turn-over time of the entire liquid mass of \sim 6 hours. The same data were acquired again, and it was found the slow amplitude decreased by a half, while the fast amplitude was unchanged (Figure 107). The behavior of the fast and slow amplitudes with increased purity indicates that the slow component has physical origin in electronegative impurity content of the xenon.

The time constants, themselves, were also observed to be dependent on applied electric field. This behavior is not yet understood. We found that $\tau_1 = \exp(2.62 + 0.157E_l)$ and $\tau_2 = \exp(6.32 + 0.214E_l)$

8.5 DISCUSSION

The study described in the previous section revealed two distinct time components for electron trains. The fast component amplitude decreases with increased extraction field and is not affected by purity. The drift time for the configuration of the TPC during the study was only \sim 2 μ s, so while it is possible that photoionization of impurities was a component of the fast amplitude, it was dominated by behavior that is consistent with increasing extraction efficiency. The slow component behav-

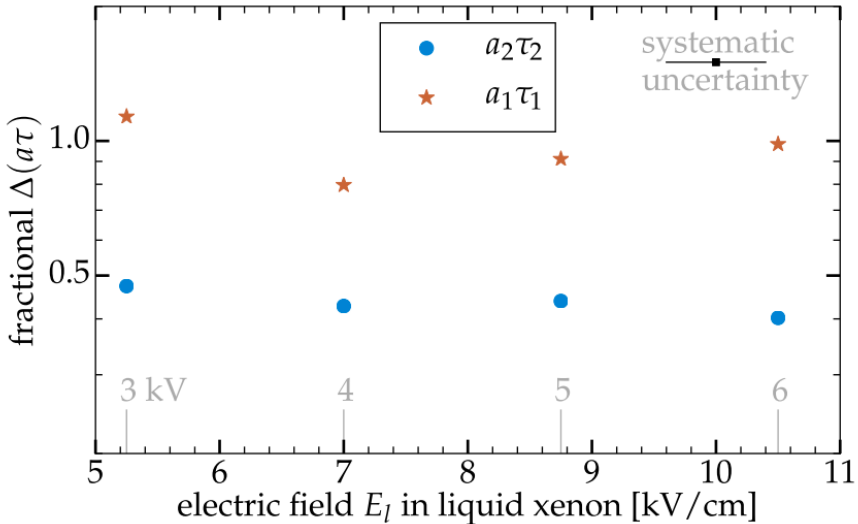


Figure 107

ior is extremely interesting: it matches the observations of delayed electron noise continuing long past a drift length in large TPCs, and it is tied with xenon purity. This suggests the physical origin of the delayed single electrons is the release of electrons from electronegative impurities. Photoionization of impurities is one possible mechanism for liberating electrons; however, other mechanisms are also possible. Exploring the timescales of such mechanisms can help lead to a positive identification of the origin of delayed electrons.

Electrons can be liberated from impurities by collisional detachment, tunneling, and, as already discussed, photoionization. Collisional detachment refers to the impurity's collision with other atoms, which could provide enough energy for the electron to be released. Collisional detachment can be expected to have timescales of $t \approx 10$ s [117], which is longer than the timescales observed in both the test bed and the larger TPCs discussed in the beginning of the chapter. Additionally, the late time component amplitude was observed to increase slightly with a higher applied electric field, which should have no effect on collisional detachment. On the other hand, electrons tunneling out of their binding potential (0.45 eV for oxygen) should increase with applied field. However, if tunneling were the case, one would expect the timescale τ_2 to decrease with applied field, which is counter to our observation. Photoionization of impurities by the UV xenon scintillation light has been discussed already, but other sources of light are also possible. Detector materials can fluoresce following exposure to the UV light. Fluorescence is characterized by delayed emission at a lower wavelength than was absorbed by the material. Of course, any light emitted in the visible spectrum would be seen in the PMT,

but light in the infrared spectrum would not be seen by the [PMT](#) and is sufficient in energy to photoionize electrons from impurities. Teflon has been observed to fluoresce in the visible region [123] [124], but depends on the content and synthesis of the Teflon. Other sources of fluorescing materials could be the impurities themselves.

One other possible source of delayed UV light is the xenon itself. Recall from Chapter ?? that prompt scintillation light in the xenon is the result of de-excitation of the lowest bound state (singlet and triplet) of the excited xenon dimer (excimer). The excimer also has higher bound states [125], which may decay more slowly and release UV photons, which in turn can photoionize impurities. The lifetimes of higher xenon excimer states have not been measured. It's reasonable to expect that some of the deexcitation photons of the higher bound state do not go into liberating electrons from impurities, but are instead observed directly by the [PMT](#). We investigated the electron trains for the presence of such single photons, but due to the close spacing of single electrons in the tail, could not distinguish for certain that single photons were not the simply result of helium after-pulsing.

Further investigation that more closely characterizes the delayed single electron behavior with purity is planned; purity (electron lifetime) can be even measured with the ^{220}Rn source, which remains plumbed into circulation system. The [PTFE](#) can also be removed to investigate if fluorescence of Teflon is a concern. Infrared LEDs were installed to investigate the feasibility of periodically flooding the [TPC](#) with photons that would not interfere with the [PMT](#) but that would be sufficient to photoionize the impurities.

PART IV

APPENDIX

A

DUMMY APPENDIX

BIBLIOGRAPHY

- [1] F Zwicky. “Die Rotverschiebung von extragalaktischen Nebeln”. In: *Helv. Phys. Acta* **6**: (1933), pp. 110–127. ISSN: 0018-0238. arXiv: [arXiv:1011.1669v3](https://arxiv.org/abs/1011.1669v3). URL: http://adsabs.harvard.edu/cgi-bin/nph-data/_query?bibcode=1933AchPh...6.110Z&link_type=GIF%5Cnpapers2://publication/uuid/E29E0909-762A-4A9D-B5B6-B850822D944A.
- [2] Gianfranco Bertone and Dan Hooper. “A History of Dark Matter”. In: (2016), pp. 1–88. arXiv: [1605.04909](https://arxiv.org/abs/1605.04909). URL: <http://arxiv.org/abs/1605.04909>.
- [3] Vera C Rubin and W Kent Ford. “Rotation of the Andromeda Nebula From a Spectroscopic Survey of Emission Regions”. In: *Astrophys. J.* **159**:February (1970).
- [4] J.P. Ostriker and P.J.E Peebles. “A Numerical Study of the Stability of Flattened Galaxies: Or, Can Cold Galaxies Survive?” In: *Astrophys. J.* **186**: (1973), pp. 467–480.
- [5] Vera C Rubin, W Kent Ford, and Norbert Thonnard. “Rotational Properties of 21 Sc Galaxies with a Large Range of Luminosities and Radii, from NGC 4605 (R=4kpc) to UGC 2885 (R=122kpc)”. In: *Astrophys. J.* **238**: (1980), pp. 471–487.
- [6] M. Milgrom. “A Modification Of the Newtonian Dynamics as a Possible Alternative to the Hidden Mass Hypothesis”. In: *Astrophys. J.* **270**: (1983), pp. 365–370.
- [7] M. Milgrom. “A Modification of the Newtonian Dynamics: Implications for Galaxies”. In: *Astrophys. J.* **270**: (1983), pp. 371–383.
- [8] M. Milgrom. “A Modification of the Newtonian Dynamics: Implications for Galaxy Systems”. In: *Astrophys. J.* **270**: (1983), pp. 384–389.
- [9] T. S. van Albada, J. N. Bahcall, K. Begeman, and R. Sanscisi. “Distribution of Dark Matter in the Spiral Galaxy NGC 3198”. In: *Astrophys. J.* **295**: (1985), pp. 305–313.
- [10] Julio F. Navarro, Carlos S. Frenk, and Simon D. M. White. “The Structure of Cold Dark Matter Halos”. In: *Astrophys. J.* **462**: (1996), p. 563. ISSN: 0004-637X. arXiv: [9508025 \[astro-ph\]](https://arxiv.org/abs/astro-ph/9508025). URL: <http://adsabs.harvard.edu/doi/10.1086/177173>.

- [11] W. J. G. de Blok, Stacy S. McGaugh, Albert Bosma, and Vera C. Rubin. “Mass Density Profiles of Low Surface Brightness Galaxies”. In: *Astrophys. J.* **552**:1 (2001), pp. L23–L26. issn: 0004637X. arXiv: [0103102 \[astro-ph\]](https://arxiv.org/abs/0103102). URL: <http://stacks.iop.org/1538-4357/552/i=1/a=L23>.
- [12] W. J. G. de Blok, Stacy S. McGaugh, and Vera C. Rubin. “High-Resolution Rotation Curves of Low Surface Brightness Galaxies. II. Mass Models”. In: *Astron. J.* **122**:5 (2001), pp. 2396–2427. issn: 00046256. arXiv: [0107326 \[astro-ph\]](https://arxiv.org/abs/0107326). URL: <http://stacks.iop.org/1538-3881/122/i=5/a=2396>.
- [13] Kyle A. Oman et al. “The unexpected diversity of dwarf galaxy rotation curves”. In: *Mon. Not. R. Astron. Soc.* **452**:4 (2015), pp. 3650–3665. issn: 13652966. arXiv: [1504.01437](https://arxiv.org/abs/1504.01437).
- [14] Davide Martizzi, Romain Teyssier, and Ben Moore. “Cusp-core transformations induced by AGN feedback in the progenitors of cluster galaxies”. In: *Mon. Not. R. Astron. Soc.* **432**:3 (2013), pp. 1947–1954. issn: 00358711. arXiv: [1211.2648](https://arxiv.org/abs/1211.2648).
- [15] Jonah Herzog-Arbeitman, Mariangela Lisanti, Piero Madau, and Lina Necib. “Empirical Determination of Dark Matter Velocities Using Metal-Poor Stars”. In: *Phys. Rev. Lett.* **120**:4 (2018), p. 41102. issn: 10797114. arXiv: [1704.04499](https://arxiv.org/abs/1704.04499). URL: <https://doi.org/10.1103/PhysRevLett.120.041102>.
- [16] Lina Necib, Mariangela Lisanti, and Vasily Belokurov. “Dark Matter in Disequilibrium: The Local Velocity Distribution from SDSS-Gaia”. In: (2018), pp. 1–21. arXiv: [1807.02519](https://arxiv.org/abs/1807.02519). URL: <http://arxiv.org/abs/1807.02519>.
- [17] Denis Erkal, Sergey E. Koposov, and Vasily Belokurov. “A sharper view of Pal 5’s tails: Discovery of stream perturbations with a novel non-parametric technique”. In: *Mon. Not. R. Astron. Soc.* **470**:1 (2017), pp. 60–84. issn: 13652966. arXiv: [1609.01282](https://arxiv.org/abs/1609.01282).
- [18] Nilanjan Banik, Gianfranco Bertone, Jo Bovy, and Nassim Bozorgnia. “Probing the nature of dark matter particles with stellar streams”. In: *J. Cosmol. Astropart. Phys.* **2018**:7 (2018). issn: 14757516. arXiv: [1804.04384](https://arxiv.org/abs/1804.04384).
- [19] M. Markevitch, A. H. Gonzalez, L. David, A. Vikhlinin, S. Murray, W. Forman, C. Jones, and W. Tucker. “A Textbook Example of a Bow Shock in the Merging Galaxy Cluster 1E0657-56”. In: (2001). issn: 0004-637X. arXiv: [0110468 \[astro-ph\]](https://arxiv.org/abs/astro-ph/0110468). URL: <http://arxiv.org/abs/astro-ph/0110468{\%}0Ahttp://dx.doi.org/10.1086/339619>.

- [20] Douglas Clowe, Marusa Bradac, Anthony H. Gonzalez, Maxim Markevitch, Scott W. Randall, Christine Jones, and Dennis Zaritsky. “A direct empirical proof of the existence of dark matter”. In: (2006). ISSN: 0004-637X. arXiv: [0608407 \[astro-ph\]](#). URL: <http://arxiv.org/abs/astro-ph/0608407{\%}0Ahttp://dx.doi.org/10.1086/508162>.
- [21] George F. Smoot. “COBE observations and results”. In: *Conf. 3K Cosmol.* (1999), pp. 1–10. arXiv: [9902027 \[astro-ph\]](#). URL: <http://aip.scitation.org/doi/abs/10.1063/1.59326>.
- [22] Wayne Hu. “Lecture Notes on CMB Theory: From Nucleosynthesis to Recombination”. In: (2008). arXiv: [0802.3688](#). URL: <http://arxiv.org/abs/0802.3688>.
- [23] Planck Collaboration. “Planck 2018 Results VI Cosmological parameters”. In: **62**: (2018), pp. 1–71. arXiv: [arXiv:1807.06209v1](#). URL: <https://pla.esac.esa.int>.
- [24] Adam G. Riess et al. “Observational Evidence from Supernovae for an Accelerating Universe and a Cosmological Constant”. In: (1998). ISSN: 00046256. arXiv: [9805201 \[astro-ph\]](#). URL: <http://arxiv.org/abs/astro-ph/9805201{\%}0Ahttp://dx.doi.org/10.1086/300499>.
- [25] S. Perlmutter et al. “Measurements of Omega and Lambda from 42 High-Redshift Supernovae”. In: (1998), pp. 1–33. ISSN: 0004-637X. arXiv: [9812133 \[astro-ph\]](#). URL: <http://arxiv.org/abs/astro-ph/9812133{\%}0Ahttp://dx.doi.org/10.1086/307221>.
- [26] Barbara Ryden. “Introduction to Cosmology”. 2006. ISBN: 0470849096. arXiv: [9904502 \[hep-ph\]](#). URL: <http://arxiv.org/abs/hep-ph/9904502>.
- [27] Edward W. Kolb and Michael S. Turner. “The Early Universe”. In: *Front.Phys.* **69**: (1990), pp. 1–547.
- [28] Chris Quigg. “Cosmic Neutrinos”. In: (2008). arXiv: [0802.0013](#). URL: <http://arxiv.org/abs/0802.0013>.
- [29] Steen Hannestad. “Cosmological neutrinos”. In: (2004). arXiv: [0404239 \[hep-ph\]](#). URL: <http://arxiv.org/abs/hep-ph/0404239{\%}0Ahttp://dx.doi.org/10.1088/1367-2630/6/1/108>.
- [30] Savas Dimopoulos, Stuart A. Raby, and Frank Wilczek. “Unification Of Couplings”. In: *Phys. Today* **44**:10 (1991), pp. 25–33. ISSN: 19450699.

- [31] Jonathan L. Feng. “Dark Matter Candidates from Particle Physics and Methods of Detection”. In: (2010), pp. 495–547. issn: 0066-4146. arXiv: [1003.0904](https://arxiv.org/abs/1003.0904). URL: <http://arxiv.org/abs/1003.0904>[\%]0A[http://dx.doi.org/10.1146/annurev-astro-082708-101659](https://dx.doi.org/10.1146/annurev-astro-082708-101659).
- [32] Mariangela Lisanti. “Lectures on Dark Matter Physics”. In: (2016). arXiv: [1603.03797](https://arxiv.org/abs/1603.03797). URL: <http://arxiv.org/abs/1603.03797>[\%]0A[http://dx.doi.org/10.1142/9789813149441__0007](https://dx.doi.org/10.1142/9789813149441__0007).
- [33] Particle Data Group. “61 . Axions and Other Similar Particles”. In: October (2017), pp. 1–27.
- [34] R. Foot and S. Vagnozzi. “Dissipative hidden sector dark matter”. In: **023512**: (2014), pp. 1–23. issn: 1550-7998. arXiv: [1409.7174](https://arxiv.org/abs/1409.7174). URL: <http://arxiv.org/abs/1409.7174>[\%]0A[http://dx.doi.org/10.1103/PhysRevD.91.023512](https://dx.doi.org/10.1103/PhysRevD.91.023512).
- [35] R. Essig et al. “Dark Sectors and New, Light, Weakly-Coupled Particles”. In: (2013). arXiv: [1311.0029](https://arxiv.org/abs/1311.0029). URL: <http://arxiv.org/abs/1311.0029>.
- [36] Bob Holdom. “Two U(1)’s and ϵ charge shifts”. In: *Phys. Lett. B* **166**:2 (1986), pp. 196–198. issn: 03702693.
- [37] S. A. Abel, M. D. Goodsell, J. Jaeckel, V. V. Khoze, and A. Ringwald. “Kinetic mixing of the photon with hidden U(1)s in string phenomenology”. In: *J. High Energy Phys.* **2008**:7 (2008). issn: 11266708. arXiv: [0803.1449](https://arxiv.org/abs/0803.1449).
- [38] Martin L. Perl. “Searches for Fractionally Charged Particles: What Should Be Done Next?” In: *Nucl. Phys. B - Proc. Suppl.* **189**:C (2009), pp. 5–8. issn: 09205632.
- [39] R Foot, H Lew, and R.R. Volkas. “Electric Charge Quantization”. In: *J. Phys. G. Nucl. Part. Phys.* **12**: (1993), pp. 361–372. issn: 0954-3899.
- [40] K. S. Babu and Rabindra N. Mohapatra. “Quantization of electric charge from anomaly constraints and a Majorana neutrino”. In: *Phys. Rev. D* **41**:1 (1990), pp. 271–277. issn: 05562821.
- [41] A. N. Schellekens. “Electric charge quantization in string theory”. In: *Phys. Lett. B* **237**:3-4 (1990), pp. 363–369. issn: 03702693.
- [42] Xiao Gang Wen and Edward Witten. “Electric and magnetic charges in superstring models”. In: *Nucl. Physics, Sect. B* **261**:C (1985), pp. 651–677. issn: 05503213.
- [43] P. A. M. Dirac. “P. A. M. Dirac”. In: *Proc. R. Soc. London* **A133**:60 (1931).

- [44] Björn Penning. “The pursuit of dark matter at colliders—an overview”. In: *J. Phys. G Nucl. Part. Phys.* **45**:6 (2018), p. 063001. ISSN: 0954-3899. URL: <http://stacks.iop.org/0954-3899/45/i=6/a=063001?key=crossref.d3fb31b11773e9c891463947d7d31ee2>.
- [45] A. A. Prinz et al. “Search for Millicharged Particles at SLAC”. In: **94309**: (1998), pp. 7–10. arXiv: [9804008 \[hep-ex\]](https://arxiv.org/abs/hep-ex/9804008). URL: <http://arxiv.org/abs/hep-ex/9804008{\%}0Ahttp://dx.doi.org/10.1103/PhysRevLett.81.1175>.
- [46] Sacha Davidson, Steen Hannestad, and Georg Raffelt. “Updated Bounds on Milli-Charged Particles”. In: (2000). ISSN: 1029-8479. arXiv: [0001179 \[hep-ph\]](https://arxiv.org/abs/hep-ph/0001179). URL: <http://arxiv.org/abs/hep-ph/0001179{\%}0Ahttp://dx.doi.org/10.1088/1126-6708/2000/05/003>.
- [47] D. S. Akerib et al. “Chromatographic separation of radioactive noble gases from xenon”. In: *Astropart. Phys.* **97**: (2018), pp. 80–87. ISSN: 09276505. arXiv: [1605.03844](https://arxiv.org/abs/1605.03844).
- [48] E. Aprile et al. “Removing krypton from xenon by cryogenic distillation to the ppq level”. In: *Eur. Phys. J. C* **77**:5 (2017). ISSN: 14346052. arXiv: [1612.04284](https://arxiv.org/abs/1612.04284).
- [49] Carl Eric Dahl. “The physics of background discrimination in liquid xenon, and first results from Xenon10 in the hunt for WIMP dark matter.” In: PhD Thesis (2009).
- [50] J. Mock, N. Barry, K. Kazkaz, D. Stolp, M. Szydagis, M. Tripathi, S. Uvarov, M. Woods, and N. Walsh. “Modeling pulse characteristics in Xenon with NEST”. In: *J. Instrum.* **9**:4 (2014). ISSN: 17480221. arXiv: [arXiv:1310.1117v2](https://arxiv.org/abs/1310.1117v2).
- [51] K. Abe et al. “XMASS detector”. In: *Nucl. Instruments Methods Phys. Res. Sect. A Accel. Spectrometers, Detect. Assoc. Equip.* **716**: (2013), pp. 78–85. ISSN: 01689002. arXiv: [1301.2815](https://arxiv.org/abs/1301.2815).
- [52] XMASS Collaboration. “A direct dark matter search in XMASS-I”. In: (2018), pp. 1–23. arXiv: [1804.02180](https://arxiv.org/abs/1804.02180). URL: <http://arxiv.org/abs/1804.02180>.
- [53] F. Neves, A. Lindote, A. Morozov, V. Solovov, C. Silva, P. Bras, J. P. Rodrigues, and M. I. Lopes. “Measurement of the absolute reflectance of polytetrafluoroethylene (PTFE) immersed in liquid xenon”. In: *J. Instrum.* **12**:1 (2017). ISSN: 17480221. arXiv: [1612.07965](https://arxiv.org/abs/1612.07965).

- [54] C Faham. "Prototype, Surface Commissioning and Photomultiplier Tube Characterization for the Large Underground Xenon (LUX) Direct Dark Matter Search Experiment". In: PhD Thesis (2014).
- [55] M. Auger et al. "The EXO-200 detector, part I: Detector design and construction". In: *J. Instrum.* 7:5 (2012). issn: 17480221. arXiv: [1202.2192](https://arxiv.org/abs/1202.2192).
- [56] D. S. Akerib et al. "Signal yields, energy resolution, and recombination fluctuations in liquid xenon". In: *Phys. Rev. D* 95:1 (2017), pp. 1–12. issn: 24700029. arXiv: [1610.02076](https://arxiv.org/abs/1610.02076).
- [57] C. H. Faham, V. M. Gehman, A. Currie, A. Dobi, P. Sorensen, and R. J. Gaitskell. "Measurements of wavelength-dependent double photoelectron emission from single photons in VUV-sensitive photomultiplier tubes". In: *J. Instrum.* 10:9 (2015). issn: 17480221. arXiv: [1506.08748](https://arxiv.org/abs/1506.08748).
- [58] D. S. Akerib et al. "Calibration, event reconstruction, data analysis and limits calculation for the LUX dark matter experiment". In: *Phys. Rev. D* 97:10 (2017), p. 102008. issn: 24700029. arXiv: [1712.05696](https://arxiv.org/abs/1712.05696). URL: <http://arxiv.org/abs/1712.05696>.
- [59] E. Aprile and T. Doke. "Liquid xenon detectors for particle physics and astrophysics". In: *Rev. Mod. Phys.* 82:3 (2010), pp. 2053–2097. issn: 00346861. arXiv: [0910.4956](https://arxiv.org/abs/0910.4956).
- [60] J Lindhard, V Nielsen, M Scharff, and P V Thomsen. "Integral equations governing radiation effects". In: *Det Kgl. Danske Videnskabernes Selskab Matematisk-fysiske Meddelelser* 33:10 (1963). URL: <http://www.sdu.dk/bibliotek/materiale+efter+type/hostede+ressourcer/matfys>.
- [61] Peter Sorensen and Carl Eric Dahl. "Nuclear recoil energy scale in liquid xenon with application to the direct detection of dark matter". In: *Phys. Rev. D - Part. Fields, Gravit. Cosmol.* 83:6 (2011), pp. 1–6. issn: 15507998. arXiv: [1101.6080](https://arxiv.org/abs/1101.6080).
- [62] LUX Collaboration et al. "Low-energy (0.7–74 keV) nuclear recoil calibration of the LUX dark matter experiment using D-D neutron scattering kinematics". In: (2016), pp. 1–24. issn: 15502368. arXiv: [1608.05381](https://arxiv.org/abs/1608.05381). URL: <http://arxiv.org/abs/1608.05381>.
- [63] J. D. Lewin and P. F. Smith. "Review of mathematics, numerical factors, and corrections for dark matter experiments based on elastic nuclear recoil". In: *Astropart. Phys.* 6:1 (1996), pp. 87–112. issn: 09276505. arXiv: [1410.6160](https://arxiv.org/abs/1410.6160).

- [64] Laura Baudis. “WIMP dark matter direct-detection searches in noble gases”. In: *Phys. Dark Universe* **4**: (2014), pp. 50–59. issn: 22126864. arXiv: [1408.4371](#). URL: <http://dx.doi.org/10.1016/j.dark.2014.07.001>.
- [65] V. Chepel and H. Araújo. “Liquid noble gas detectors for low energy particle physics”. In: *J. Instrum.* **8**:4 (2013). issn: 17480221. arXiv: [1207.2292](#).
- [66] U Oberlack. “First limits on WIMP dark matter from the XENON10 experiment”. In: *J. Phys. Conf. Ser.* **110**:6 (2008), p. 062020. issn: 1742-6596. URL: <http://stacks.iop.org/1742-6596/110/i=6/a=062020?key=crossref.bfd78c6898a820849cdc54a2974555a3>.
- [67] D. S. Akerib et al. “First results from the LUX dark matter experiment at the Sanford Underground Research Facility”. In: *Phys. Rev. Lett.* **112**: (2014). issn: 0031-9007, 1079-7114. arXiv: [arXiv:1310.8214v2](#). URL: <http://arxiv.org/abs/1310.8214>.
- [68] E. Aprile et al. “First dark matter results from the XENON100 experiment”. In: *Phys. Rev. Lett.* **105**:13 (2010), pp. 9–13. issn: 00319007. arXiv: [1005.0380](#).
- [69] P. Sorensen et al. “Lowering the low-energy threshold of xenon detectors”. In: *Proc. Sci.* (2010). issn: 18248039. arXiv: [arXiv:1011.6439v1](#).
- [70] Peter Sorensen. “Anisotropic diffusion of electrons in liquid xenon with application to improving the sensitivity of direct dark matter searches”. In: *Nucl. Instruments Methods Phys. Res. Sect. A Accel. Spectrometers, Detect. Assoc. Equip.* **635**:1 (2011), pp. 41–43. issn: 01689002. arXiv: [1102.2865 \[astro-ph.IM\]](#).
- [71] J. Angle et al. “Search for light dark matter in XENON10 data”. In: *Phys. Rev. Lett.* **107**:5 (2011), pp. 1–6. issn: 10797114. arXiv: [1104.3088](#).
- [72] Rouven Essig, Aaron Manalaysay, Jeremy Mardon, Peter Sorensen, and Tomer Volansky. “First direct detection limits on Sub-GeV dark matter from XENON10”. In: *Phys. Rev. Lett.* **109**:2 (2012), pp. 1–5. issn: 00319007. arXiv: [1206.2644](#).
- [73] D. S. Akerib et al. “A search for annual and diurnal rate modulations in the LUX experiment”. In: (2018), pp. 1–12. arXiv: [1807.07113](#). URL: <http://arxiv.org/abs/1807.07113>.
- [74] D. S. Akerib et al. “First Searches for Axions and Axionlike Particles with the LUX Experiment”. In: *Phys. Rev. Lett.* **118**:26 (2017), pp. 1–7. issn: 10797114. arXiv: [1704.02297](#).

- [75] Nicole A Larsen. “An Effective Field Theory Analysis of the First LUX Dark Matter Search”. In: PhD Thesis (2016).
- [76] A. Dobi, C. Davis, C. Hall, T. Langford, S. Slutsky, and Y. R. Yen. “Detection of krypton in xenon for dark matter applications”. In: *Nucl. Instruments Methods Phys. Res. Sect. A Accel. Spectrometers, Detect. Assoc. Equip.* **665**: (2011), pp. 1–6. ISSN: 01689002. arXiv: [1103.2714 \[astro-ph\]](https://arxiv.org/abs/1103.2714). URL: <http://dx.doi.org/10.1016/j.nima.2011.11.043>.
- [77] D. S. Akerib et al. “The Large Underground Xenon (LUX) experiment”. In: *Nucl. Instruments Methods Phys. Res. Sect. A Accel. Spectrometers, Detect. Assoc. Equip.* **704**: (2013), pp. 111–126. ISSN: 01689002. arXiv: [1211.3788](https://arxiv.org/abs/1211.3788).
- [78] D.S. Akerib et al. “Radiogenic and muon-induced backgrounds in the LUX dark matter detector”. In: *Astropart. Phys.* **62**: (2015), pp. 33–46. ISSN: 09276505. arXiv: [1403.1299](https://arxiv.org/abs/1403.1299). URL: <http://dx.doi.org/10.1016/j.astropartphys.2014.07.009><http://linkinghub.elsevier.com/retrieve/pii/S0927650514001054>.
- [79] D. S. Akerib et al. “FPGA-based trigger system for the LUX dark matter experiment”. In: *Nucl. Instruments Methods Phys. Res. Sect. A Accel. Spectrometers, Detect. Assoc. Equip.* **818**: (2016), pp. 57–67. ISSN: 01689002. arXiv: [1511.03541](https://arxiv.org/abs/1511.03541).
- [80] A Currie et al. “Position Reconstruction in a Dual Phase Xenon Scintillation Detector”. In: *IEEE* **59**:6 (2012), pp. 3286–3293.
- [81] D. S. Akerib et al. “Position reconstruction in LUX”. In: *J. Instrum.* **13**:2 (2018). ISSN: 17480221. arXiv: [1710.02752](https://arxiv.org/abs/1710.02752).
- [82] D. S. Akerib et al. “83m-Kr calibration of the 2013 LUX dark matter search”. In: *Phys. Rev. D* **96**:11 (2017), p. 112009. ISSN: 2470-0010. arXiv: [arXiv:1708.02566v1](https://arxiv.org/abs/1708.02566v1). URL: <https://link.aps.org/doi/10.1103/PhysRevD.96.112009>.
- [83] D. S. Akerib et al. “Tritium calibration of the LUX dark matter experiment”. In: *Phys. Rev. D* **93**:7 (2016). ISSN: 24700029. arXiv: [1512.03133](https://arxiv.org/abs/1512.03133).
- [84] D. S. Akerib et al. “3D modeling of electric fields in the LUX detector”. In: *J. Instrum.* **12**: (2017), P11022.
- [85] D. S. Akerib et al. “Results from a Search for Dark Matter in the Complete LUX Exposure”. In: *Phys. Rev. Lett.* **118**:2 (2017), pp. 1–8. ISSN: 10797114. arXiv: [1608.07648](https://arxiv.org/abs/1608.07648).

- [86] D. S. Akerib et al. “Improved Limits on Scattering of Weakly Interacting Massive Particles from Reanalysis of 2013 LUX Data”. In: *Phys. Rev. Lett.* **116**:16 (2016), pp. 1–7. ISSN: 10797114. arXiv: [1512.03506](https://arxiv.org/abs/1512.03506).
- [87] C. et al. Patrignani. “Passage of Particles Through Matter”. In: *PDG (Particle Data Group)* (2017). ISSN: 1434-6044. URL: <http://dbcompas.ihep.su/2006/reviews/passagerpp.pdf>.
- [88] H. Bethe. “Zur Theorie des Durchgangs schneller Korpuskularstrahlen durch Materie”. In: *Ann. Phys.* **5**: (1930), pp. 325–400. ISSN: 15213889.
- [89] U Fano. “Penetration of Protons, Alpha Particles, and Mesons12”. In: *Ann. Rev Nucl. Scei* **123**: (1963), pp. 1–66. URL: <https://www.google.com/books?hl=tr&lr={\&}id=I6wrAAAAYAAJ{\&}oi=fnd{\&}pg=PA287{\&}dq=Fano%2C+U.+%281964%29.+Penetrations+of+protons%2C+alpha+particles%2C+and+mesons.+Studies+in+Penetra-tion+of+Charged+Particles+in+Matter%2C+1133%3A287.+%28cited+on+pages+15%2C+16%2C+and+17%29{\&}ots=PYmM1cE>.
- [90] Hans Bichsel. “A method to improve tracking and particle identification in TPCs and silicon detectors”. In: *Nucl. Instruments Methods Phys. Res. Sect. A Accel. Spectrometers, Detect. Assoc. Equip.* **562**:1 (2006), pp. 154–197. ISSN: 01689002.
- [91] J.H. Allison, W. W. M ; Cobb. “Relativistic Charged Particle Identification By Energy Loss”. In: *Ann. Rev. Nucl. Part. Sci.* **30**: (1980), pp. 253–298.
- [92] Zhong He. “Review of the Shockley-Ramo theorem and its application in semiconductor gamma-ray detectors”. In: *Nucl. Instruments Methods Phys. Res. Sect. A Accel. Spectrometers, Detect. Assoc. Equip.* **463**:1-2 (2001), pp. 250–267. ISSN: 01689002.
- [93] KT McDonald. “Notes on electrostatic wire grids”. In: *Notes Elec-trost. wire grids*. 2003. URL: <http://www.hep.princeton.edu/~mcdonald/examples/grids.pdf>.
- [94] V. E. Guiseppe, S. R. Elliott, A. Hime, K. Rielage, and S. Westerdale. “A Radon Progeny Deposition Model”. In: 2011, pp. 95–100. URL: <http://aip.scitation.org/doi/abs/10.1063/1.3579565>.
- [95] E. O. Knutson. “Radon and Its Decay Products in Indoor Air”. Wiley, 1988.

- [96] Yasuhiro Takemoto. “⁷Be solar neutrino observation with KamLAND”. In: *Nucl. Part. Phys. Proc.* **265-266**: (2015), pp. 139–142. ISSN: 24056014. URL: <http://linkinghub.elsevier.com/retrieve/pii/S2405601415003788>.
- [97] A. Gando et al. “Be 7 solar neutrino measurement with KamLAND”. In: *Phys. Rev. C* **92**:5 (2015), p. 055808. ISSN: 0556-2813. URL: <https://link.aps.org/doi/10.1103/PhysRevC.92.055808>.
- [98] G. Bellini et al. “Final results of Borexino Phase-I on low-energy solar neutrino spectroscopy”. In: *Phys. Rev. D* **89**:11 (2014), p. 112007. ISSN: 1550-7998. URL: <https://link.aps.org/doi/10.1103/PhysRevD.89.112007>.
- [99] Christer Samuelsson. “Plate-out and Implantation of ²²²Rn Decay Products in Dwellings”. In: *Environ. Int. Vol.* **22**:Suppl. 1 (1996), pp. 839–843.
- [100] Lawrence Stein. “The Chemistry of Radon”. In: *Radiochim. Acta* **32**: (1982), pp. 163–171. ISSN: 0036-8075.
- [101] Lawrence Stein. “Chapter 18 Chemical Properties of Radon”. In: *Radon Its Decay Prod.* 1987, pp. 240–251.
- [102] J.K. Hammer, B; Norskov. “Theory of adsorption and surface reactions”. In: (1997), pp. 285–351.
- [103] J . Bigu. “Plate-Out of Radon and Thoron Progeny on Large Surfaces”. In: *Radon Its Decay Prod.* 1987. Chap. 21, pp. 272–284.
- [104] E S Morrison, T Frels, E H Miller, R W Schnee, and J Street. “Radon daughter plate-out onto Teflon.” In: *arXiv.org, e-Print Arch. Phys.* **090002**: (2017), pp. 1–4. ISSN: 15517616. URL: <http://arxiv.org/pdf/1708.08534.pdf>.
- [105] M. Bruemmer, M. Nakib, R. Calkins, J. Cooley, and S. Sekula. “Studies on the reduction of radon plate-out”. In: *AIP Conf. Proc.* **1672**: (2015). ISSN: 15517616. arXiv: [1506.04050](https://arxiv.org/abs/1506.04050).
- [106] D. S. Akerib et al. “Projected WIMP sensitivity of the LUX-ZEPLIN (LZ) dark matter experiment”. In: (2018), pp. 1–16. arXiv: [1802.06039](https://arxiv.org/abs/1802.06039). URL: [http://arxiv.org/abs/1802.06039](https://arxiv.org/abs/1802.06039).
- [107] B. Edwards et al. “Measurement of single electron emission in two-phase xenon”. In: *Astropart. Phys.* **30**:2 (2008), pp. 54–57. ISSN: 09276505.
- [108] E. Santos et al. “Single electron emission in two-phase xenon with application to the detection of coherent neutrino-nucleus scattering”. In: *J. High Energy Phys.* **2011**:12 (2011). ISSN: 11266708. arXiv: [1110.3056 \[physics.ins-det\]](https://arxiv.org/abs/1110.3056).

- [109] E. Aprile et al. “Observation and applications of single-electron charge signals in the XENON100 experiment”. In: *J. Phys. G Nucl. Part. Phys.* **41**:3 (2014). ISSN: 09543899. arXiv: [1311.1088](https://arxiv.org/abs/1311.1088).
- [110] J. Xu and Et al. “An investigation of the background electron emissions in the LUX detector”. Tech. rep. Salt Lake City, UT: 16-19 April Meeting APS, 2016.
- [111] E. M. Gushchin, A. A. Kruglov, and I. M. Obodovskii. “Emission of “hot” electrons from liquid and solid argon and xenon”. In: *Sov. Phys. JETP* **55**:5 (1982).
- [112] B. N.V. Edwards et al. “Extraction efficiency of drifting electrons in a two-phase xenon time projection chamber”. In: *J. Instrum.* **13**:1 (2018). ISSN: 17480221. arXiv: [1710.11032](https://arxiv.org/abs/1710.11032).
- [113] Peter Sorensen. “Electron train backgrounds in liquid xenon dark matter search detectors are indeed due to thermalization and trapping”. In: (2017), pp. 1–5. arXiv: [1702 . 04805](https://arxiv.org/abs/1702.04805). URL: <http://arxiv.org/abs/1702.04805>.
- [114] W. Tauchert and Werner F. Schmidt. “Energy of the Quasi-free Electron State in Liquid Argon, Krypton, and Xenon”. In: *Zeitschrift für Naturforsch. A* **30a**: (1975), pp. 1085–1086.
- [115] Morrel Cohen and J. Lekner. “Theory of Hot Electrons in Gases, Liquids, and Solids”. In: *Phys. Rev.* **158**:1935 (1967), pp. 305–309. ISSN: 0031-899X.
- [116] A I Bolozdynya. “Two-phase emission detectors and their applications”. In: *Nucl. Instruments Methods Phys. Res. A* **422**: (1999), pp. 314–320.
- [117] P. Sorensen and K. Kamdin. “Two distinct components of the delayed single electron noise in liquid xenon emission detectors”. In: *J. Instrum.* **13**:2 (2018). ISSN: 17480221. arXiv: [1711.07025](https://arxiv.org/abs/1711.07025).
- [118] O. Bunemann, T.E. Cranshaw, and J.A. Harvey. “Design of Grid Ionization Chambers”. In: *Candian J. Res.* **27**:A (1949), pp. 191–206.
- [119] R. Bevilacqua, A. Göök, F. J. Hambsch, N. Jovančević, and M. Vidiši. “A procedure for the characterization of electron transmission through Frisch grids”. In: *Nucl. Instruments Methods Phys. Res. Sect. A Accel. Spectrometers, Detect. Assoc. Equip.* **770**: (2015), pp. 64–67. ISSN: 01689002.
- [120] T. Hashimoto, A. Habiro, M. Noguchi, and T. Kubota. “Spontaneous deposition behavior of polonium on several kinds of metallic wires and its utilization as a conventional alpha-source”. In: *Radioisotopes* **39**:7 (1990), pp. 291–297.

- [121] P.E. Figgins. "The Radiochemistry of Polonium". Tech. rep. 1961.
- [122] Luigi Blum, Walter; Riefler, Werner; Rolandi. "Particle Detection with Drift Chambers Particle Acceleration and Detection". 2008. ISBN: 9783540766834.
- [123] V. F. Gachkovskii, T. A. Kudryavtseva, and N. M. Chirkov. "Dependence of the fluorescence intensity of polytetrafluoroethylene on the conditions of synthesis and molecular weight". In: *Bull. Acad. Sci. USSR Div. Chem. Sci.* **18**:11 (1969), pp. 2297–2299. ISSN: 05685230.
- [124] S. A. Khatipov, R. N. Nurmukhametov, Yu E. Sakhno, V. G. Klimenko, D. I. Seliverstov, S. T. Sychkova, and T. V. Sakhno. "Color and fluorescence of polytetrafluoroethylene treated by γ -irradiation near the melting point". In: *Nucl. Instruments Methods Phys. Res. Sect. B Beam Interact. with Mater. Atoms* **269**:21 (2011), pp. 2600–2604. ISSN: 0168583X. URL: <http://dx.doi.org/10.1016/j.nimb.2011.07.017>.
- [125] Walter C. Ermler, Yoon S. Lee, and Kenneth S. Pitzer. "Ab initio effective core potentials including relativistic effects. IV. Potential energy curves for the ground and several excited states of Au₂". In: *J. Chem. Phys.* **70**:1 (1979), pp. 293–298. ISSN: 00219606.